

FINAL
INDEX
2017
45327
P. 121

**TRANSMISSION ELECTRON MICROSCOPE STUDIES
OF EXTRATERRESTRIAL MATERIALS**

Final Technical Report for NASA Contract:

NAS 9-18992

(NASA-CR-188363) TRANSMISSION
ELECTRON MICROSCOPE STUDIES OF
EXTRATERRESTRIAL MATERIALS Final
Technical Report (MVA) 121 p

N95-24222

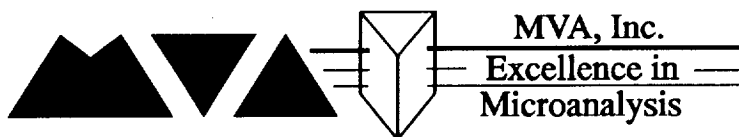
Unclas

G3/25 0045327

Prepared by:

Dr. Lindsay P. Keller
MVA, Inc.
5500 Oakbrook Parkway, Suite 200
Norcross, GA 30093

January 31, 1995



5500 Oakbrook Parkway #200
Norcross, Georgia 30093
404-662-8509

TABLE OF CONTENTS

TEM Studies of Extraterrestrial Materials

4.1 Analyze Carbon in Interplanetary Dust Particles	2
a. Embedding IDPs in sulfur	2
b. Preparing ultramicrotome thin sections	8
c. Elimination of sulfur embedding media	8
d. Carbon analysis using HRTEM	14
e. Electron diffraction analysis of carbon in IDPs	19
f. Carbon analysis by energy-dispersive x-ray spectrometry	23
g. Carbon analysis by electron energy-loss spectroscopy	25
h. Mineralogy and mineral chemistry of major phases	43
i. Reflectance spectroscopy of IDPs	46
4.1 Analyze Selected Lunar Samples Using TEM	49
a. Embedding and sectioning lunar samples	49
b. TEM studies of opaque assemblages in high-Ti basalts	49
c. Analyzing blue rutiles in lunar basalt 70035	56
d. Analysis of reaction rims on armalcolites	56
e. Reduction microstructures in lunar soil grains	60
f. Analyzing agglutinates in lunar soils	69
g. Analyzing amorphous rims and vapor deposits	83
h. Analyzing submicrometer glass spheres in soils	85
i. Analyzing selected regolith grains for carbon	85
j. Analyzing selected lunar grains for reflectance spectra	89
Appendix- Publications	90

SECTION 4.1. ANALYZE CARBON IN INTERPLANETARY DUST PARTICLES

4.1.a. Embedding IDPs in sulfur.

We have embedded 10 IDPs in sulfur (see Table 1 below). Figures 1-5 are optical micrographs showing the IDPs embedded in sulfur. These figures show the IDPs in cross-section after thin sections have been obtained.

TABLE 1. IDPs embedded in sulfur.

L2011 R11	L2008F16
L2006, Cluster 14, #10	L2008E5
L2011A4	L2009J4
L2008F13	L2008E3
L2008G9	L2008F4

Our procedure for sulfur embedding is to prepare a molten droplet (100-200 μm in diameter) of elemental sulfur on a glass slide. IDPs are dry-transferred using a fine tungsten needle and dropped onto the sulfur droplet. The IDP is manipulated with the tungsten needle until it is encased within the droplet. At this point, the droplet is heated until the sulfur undergoes a phase change to a highly viscous form, and is allowed to solidify. We have also modified the technique to embed the IDPs in crystalline sulfur. In this technique, the nucleation and growth of sulfur crystals is carefully controlled so that the IDP ends up as an inclusion in a large single crystal of sulfur. An advantage of this latter technique is that the sulfur bead is optically transparent.

We emphasize, that prior to this report, only two other IDPs have been successfully embedded in sulfur and subsequently thin-sectioned.

ORIGINAL PAGE IS
OF POOR QUALITY



FIGURE 1. Reflected light micrograph of L2011R11 (top) and L2006, Cluster 14, Particle #10 (bottom). Width of field is 200 μm .



ORIGINAL PAGE IS
OF POOR QUALITY

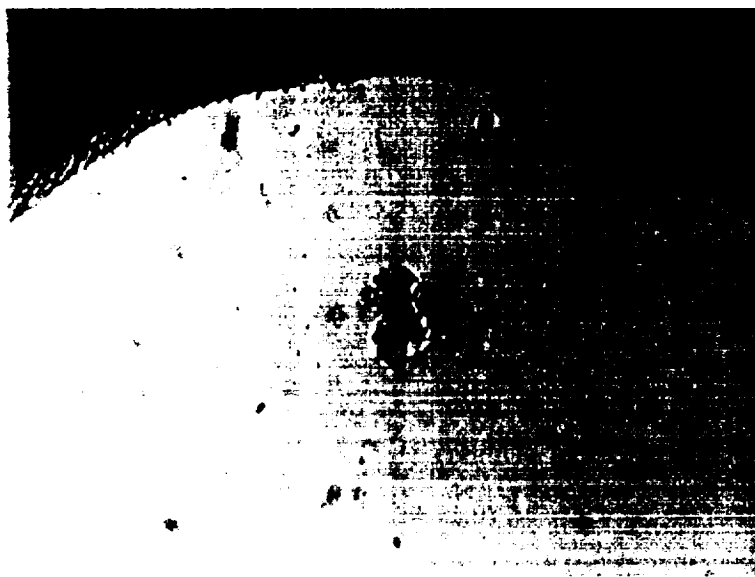
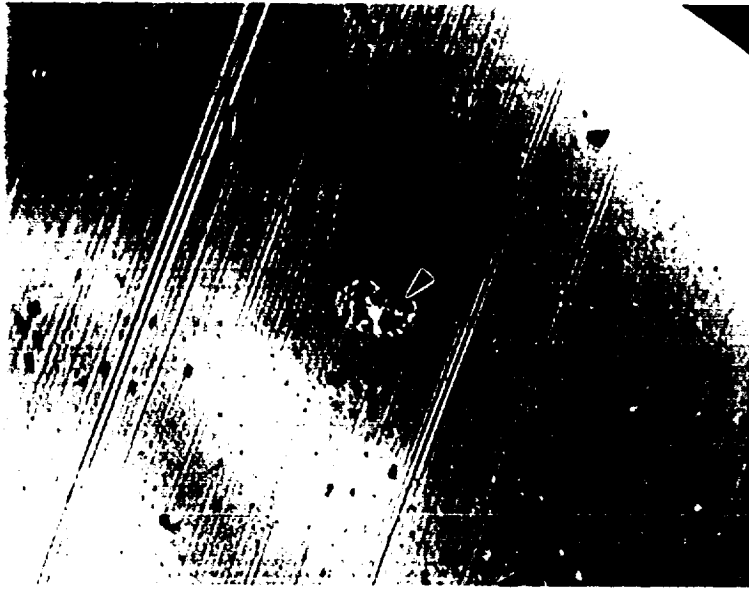


FIGURE 2. Reflected light micrograph of L2011A4 (top) and L2008F13 (bottom).
Width of field is 200 μm .



ORIGINAL PAGE IS
OF POOR QUALITY



FIGURE 3. Reflected light micrograph of L2008G9 (top) and L2008F16 (bottom). Width of field is 200 μm .



FIGURE 4. Reflected light micrograph of L2008E5 (top) and L2008J4 (bottom).
Width of field is 200 μm .

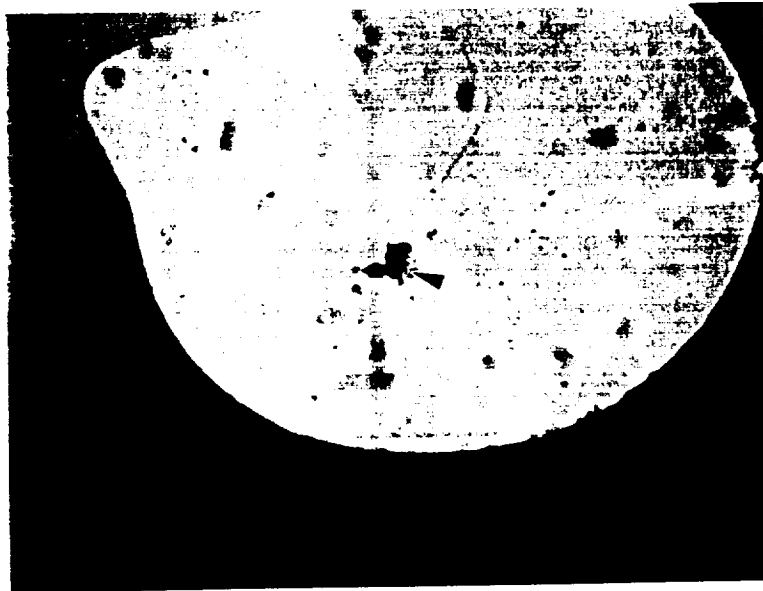
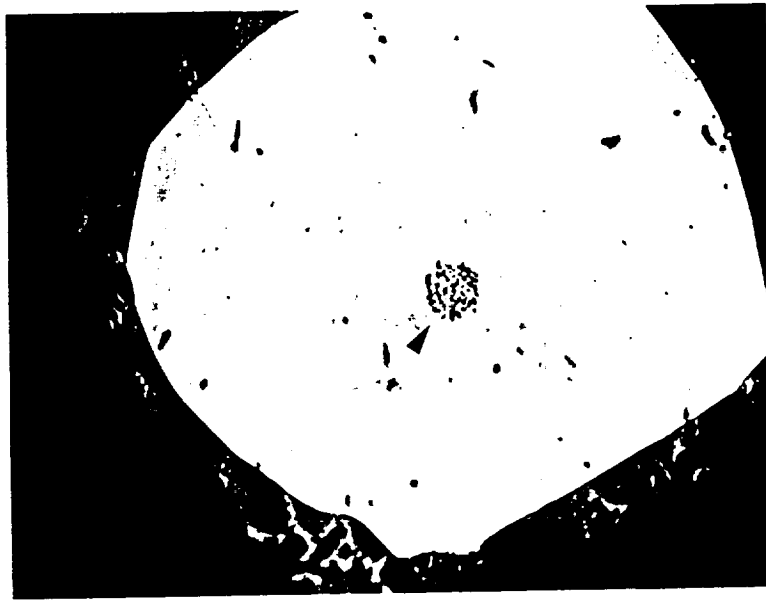


FIGURE 5. Reflected light micrograph of L2008E3 (top) and L2008F4 (bottom).
Width of field is 200 μm .

4.1.b and 4.1.c. Preparing ultramicrotome thin sections and elimination of the sulfur embedding media.

After embedding the IDPs in a bead of glassy or crystalline sulfur, the sulfur bead is attached to a block of epoxy with a cyanoacrylate adhesive, which is held in the microtome chuck. Thin sections were cut using a Reichert-Jung Ultramicrotome. The thin sections were all silver- to grey-colored in reflected light, which indicates a section thickness of 50 to 80 nm. Thin sections were placed on SiO thin films attached to copper TEM grids. The use of SiO thin films has several advantages and disadvantages. SiO thin films are carbon-free, relatively strong, and are amorphous. The major disadvantages are that SiO films tend to charge (because SiO is an insulator) making imaging difficult, and the films contain Si and O which are also present in the IDP thin sections. This latter point makes it difficult to extract chemical compositions of silicates in the IDPs.

We successfully prepared ultramicrotome thin sections of the IDPs listed in Table 1. After the thin sections were collected on the SiO thin film TEM grids, the grids were placed in a JEOL 1200 TEM, and the sulfur was allowed to sublime. Complete sublimation occurred over a few minutes. Figures 6-10 are low-magnification TEM images showing typical thin sections of each of the particles. Although using sulfur as an embedding medium is much more difficult than using epoxy, it can be seen from the figures that the quality of the thin sections is comparable to that obtained by using epoxy.

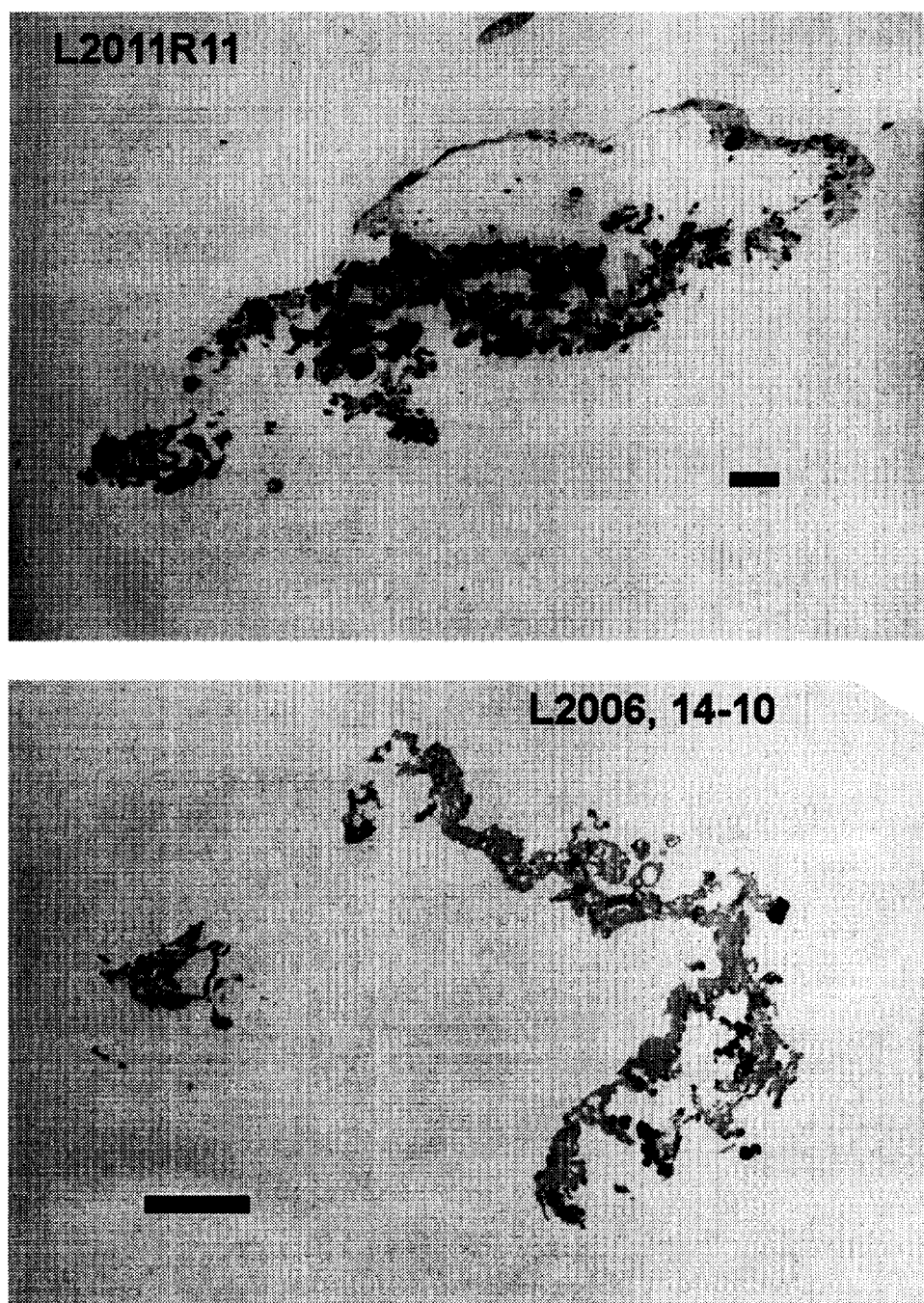


FIGURE 6. Bright-field TEM image of microtome thin sections of L2011R11 (top) and L2006, Cluster 14, Particle #10 (bottom). Scale bar is 1 μm .

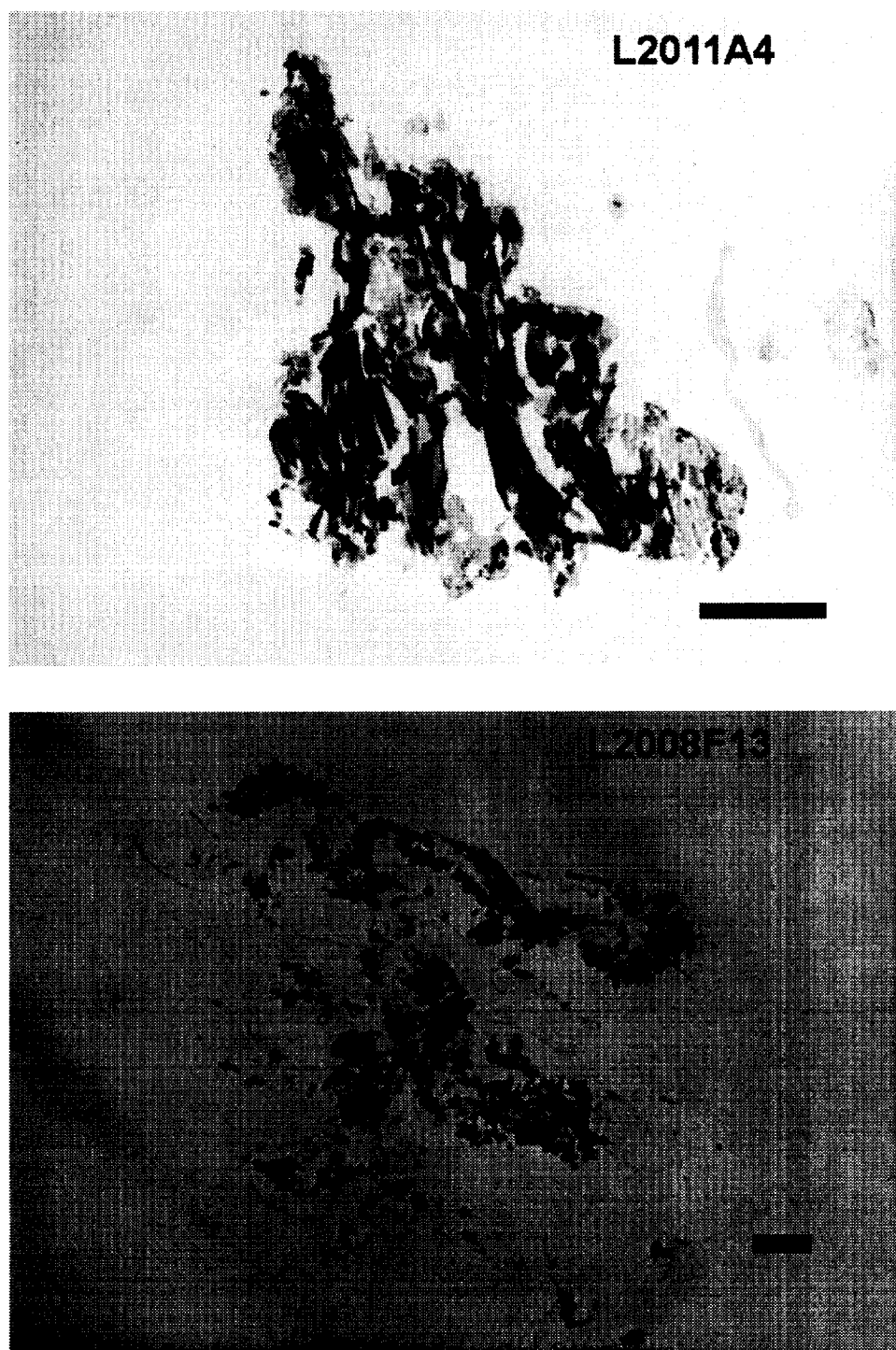
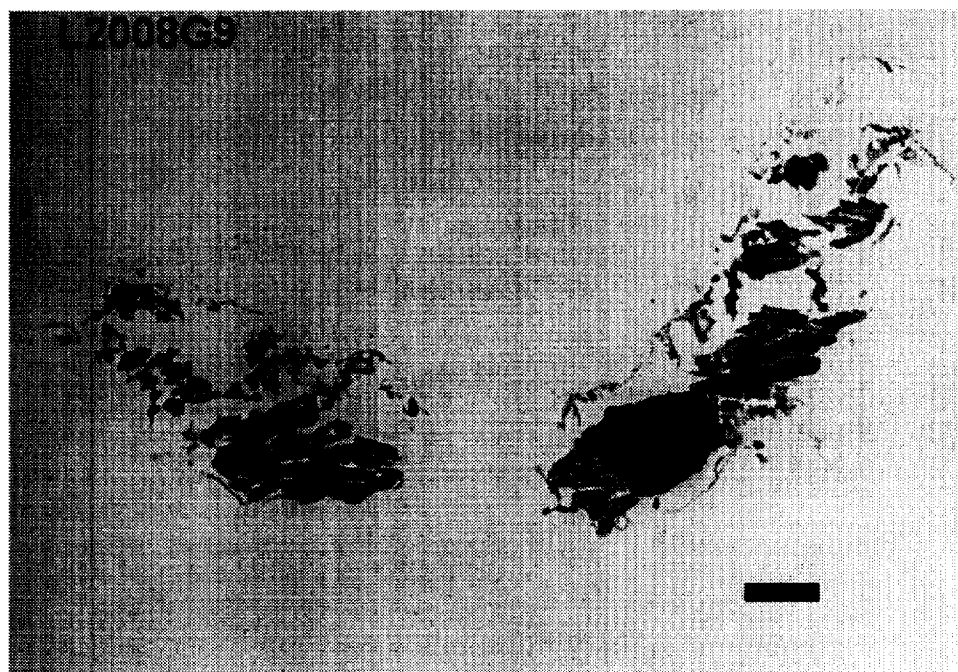


FIGURE 7. Bright-field TEM image of microtome thin sections of L2011A4 (top) and L2008F13 (bottom). Scale bar is 1 μm .



L2008F16

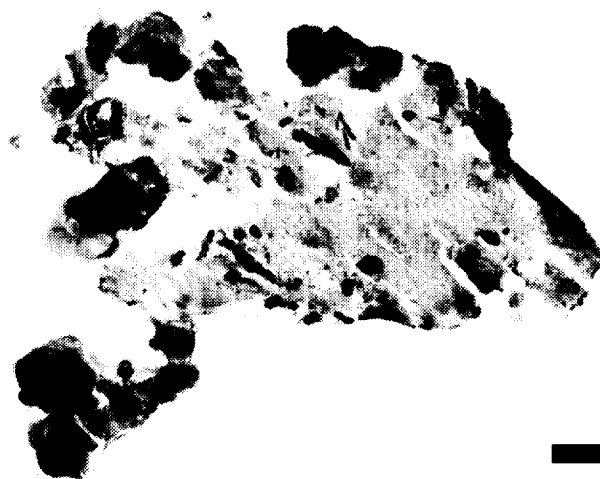


FIGURE 8. Bright-field TEM image of microtome thin sections of L2008G9 (top) and L2008F16 (bottom). Scale bar is 1 μm .

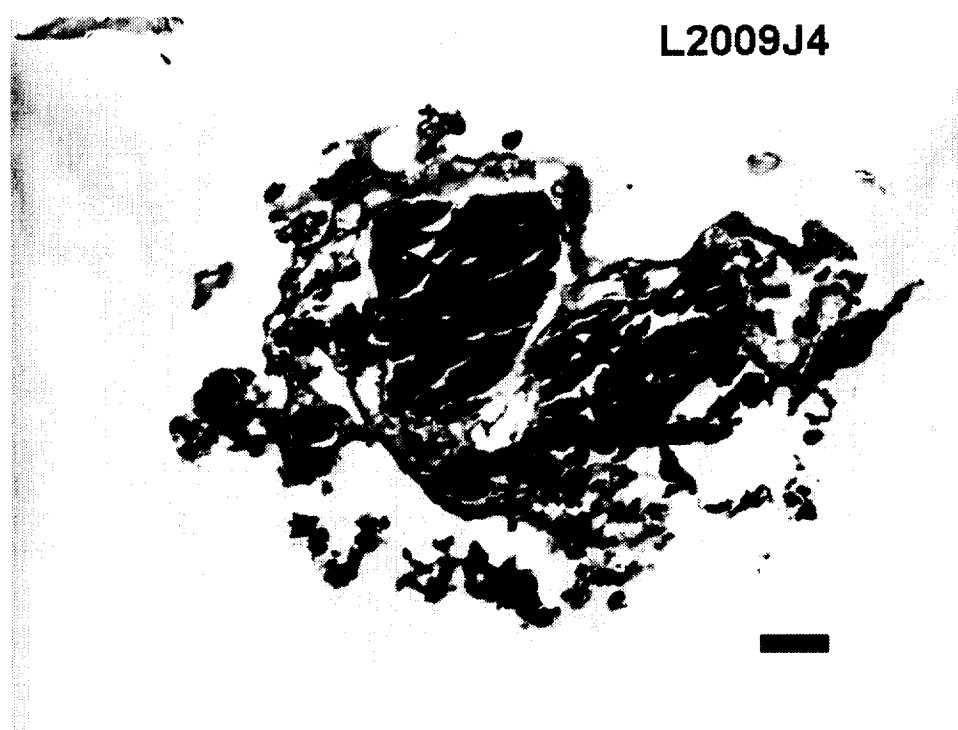
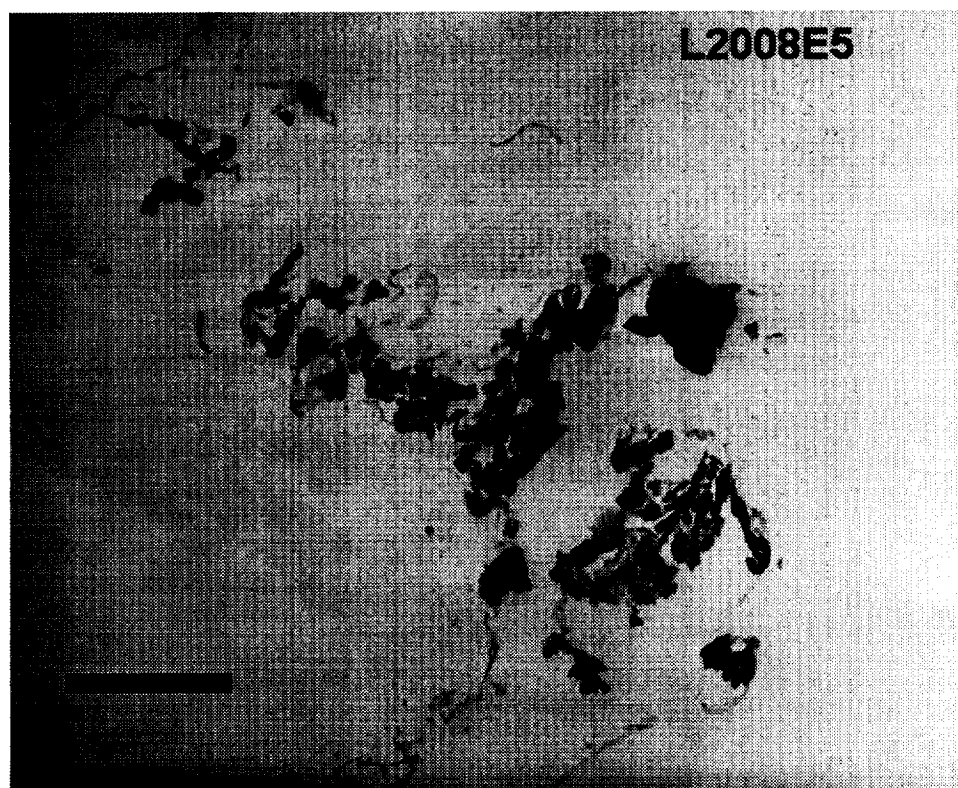


FIGURE 9. Bright-field TEM image of microtome thin sections of L2008E5 (top) and L2008J4 (bottom). Scale bar is 1 μm .

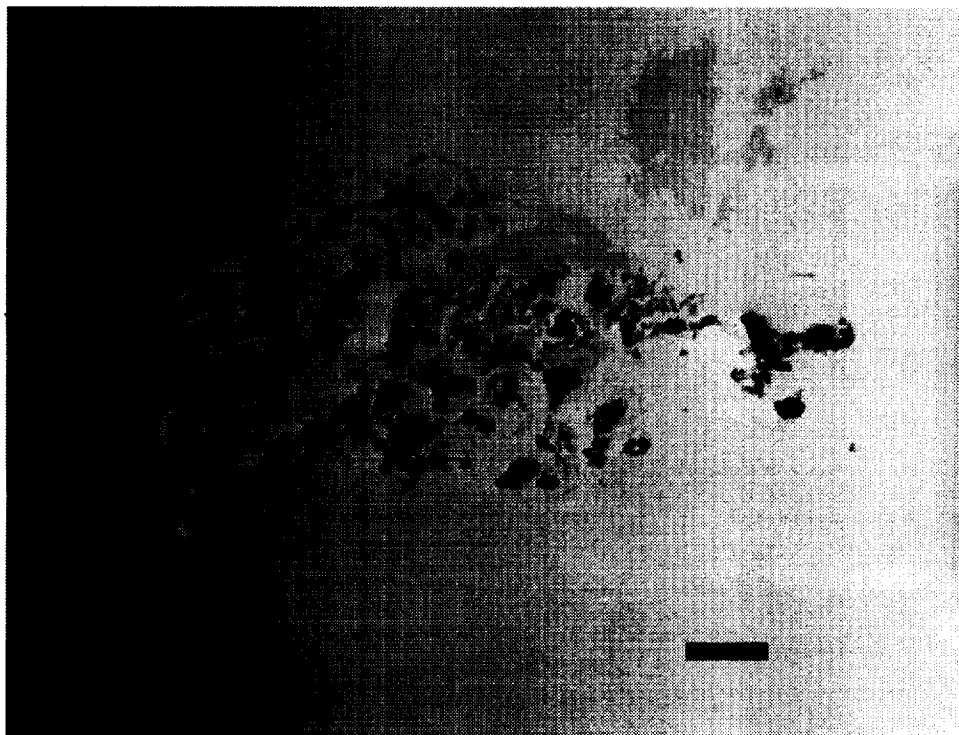
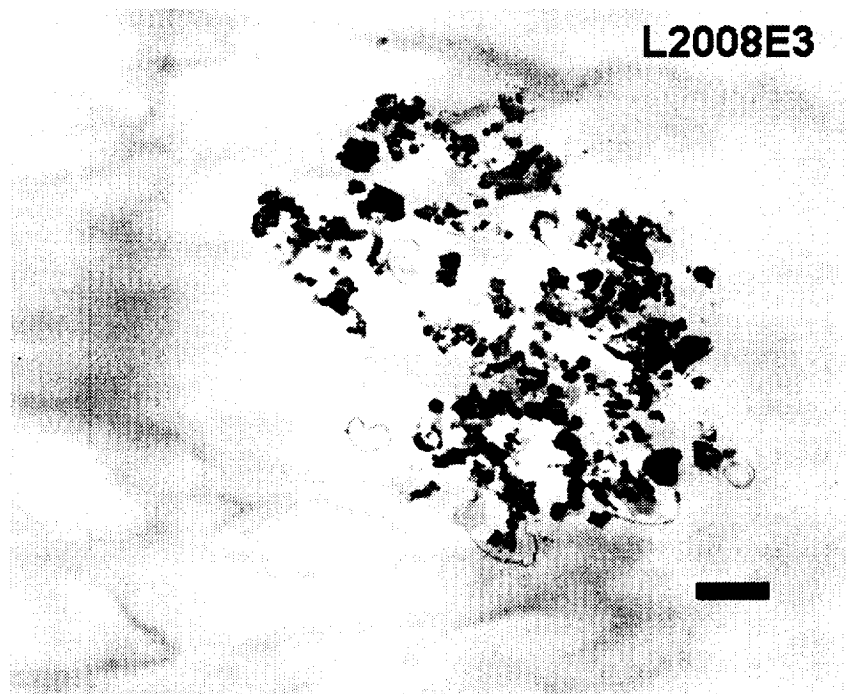


FIGURE 10. Bright-field TEM image of microtome thin sections of L2008E3 (top) and L2008F4 (bottom). Scale bar is 1 μm .

4.2.d. Carbon analysis using high-resolution TEM imaging.

High-resolution transmission electron microscope (HRTEM) images were obtained from the carbonaceous materials in only four of the analyzed IDPs. As described above, the ultramicrotome thin sections of IDPs were placed on SiO thin films, which have a tendency to charge (i.e. electrostatic build-up). Charging results in sample movement during the time that the images are recorded, and this movement blurs the detail in the HRTEM images. For some of the IDPs (e.g. L2008F16) the carbonaceous material is intimately intergrown with poorly-crystalline phyllosilicates making it impossible to distinguish. HRTEM images for L2011R11, L2008F13, L2008F4, and L2008 are shown in Figures 11-14. The carbonaceous material in these images is generally featureless and lacks any indication of graphite-like lattice spacings (e.g. the 0.34 nm basal spacing). Mineral grains that occur as inclusions within the carbonaceous material are indicated in the figures.

ORIGINAL PAGE IS
OF POOR QUALITY

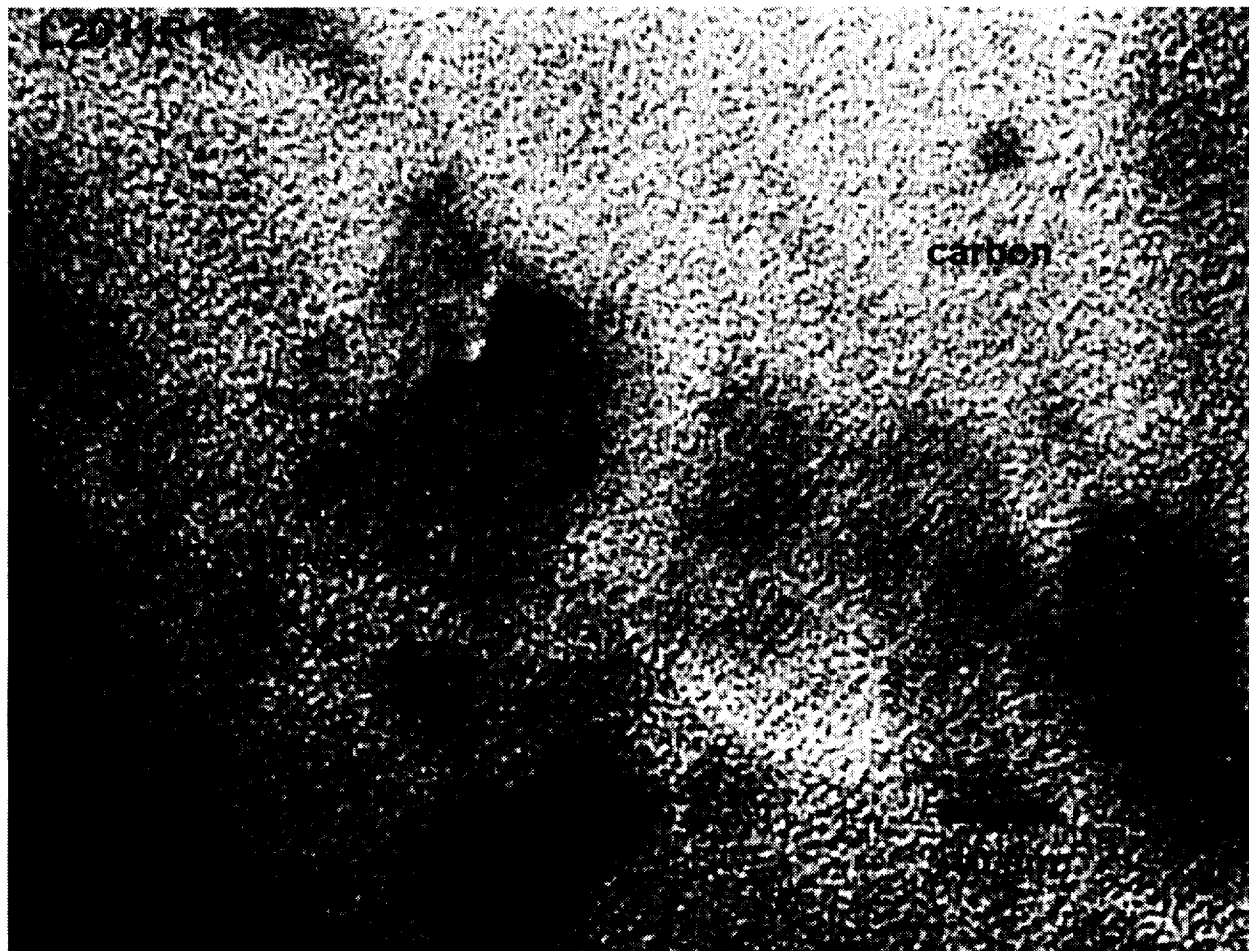


FIGURE 11. High-resolution TEM image of carbonaceous material in L2011R11, showing no evidence for the presence of graphitic layers.

ORIGINAL PAGE IS
OF POOR QUALITY

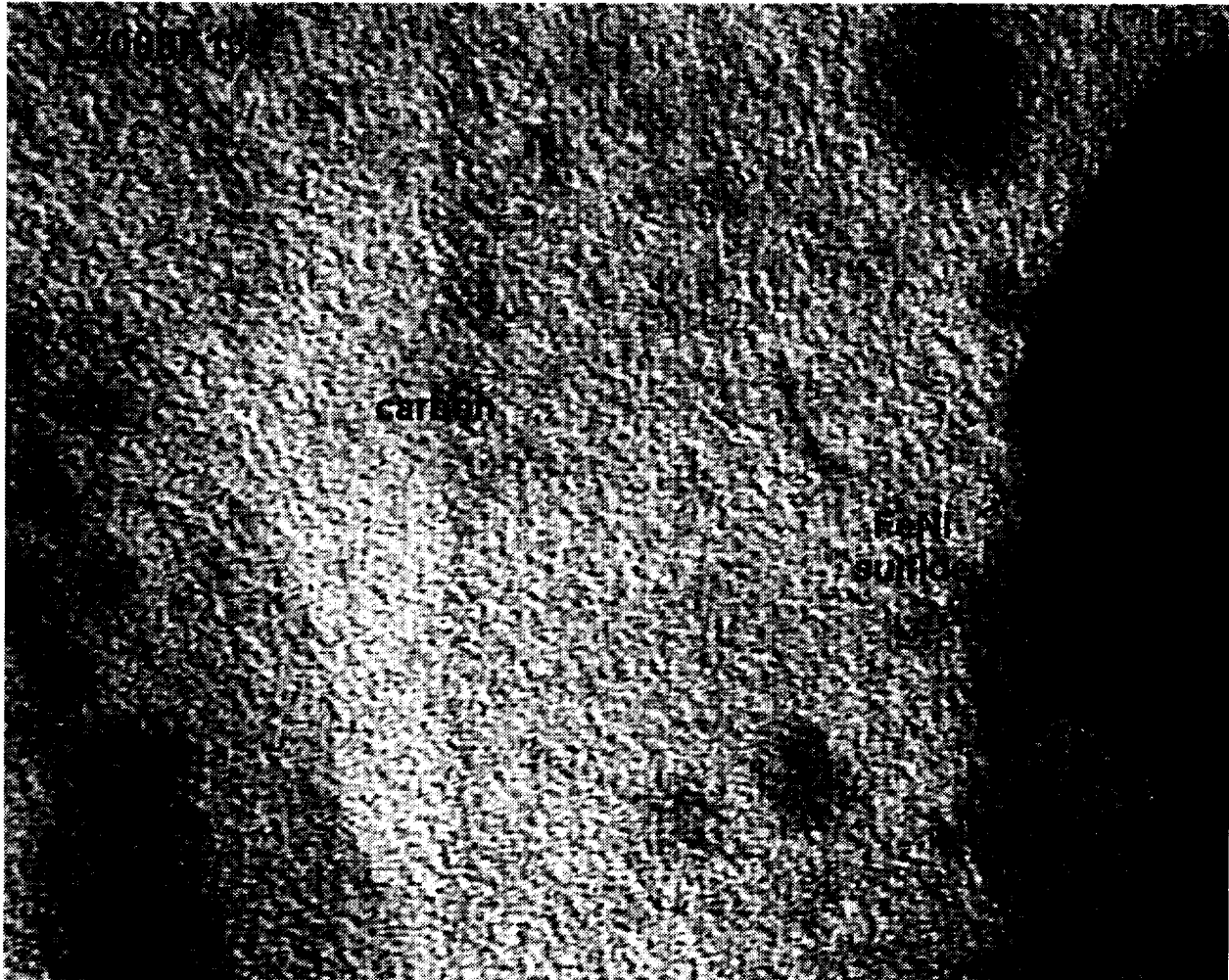


FIGURE 12. High-resolution TEM image of carbonaceous material in L2008F13, showing no evidence for the presence of graphitic layers.

ORIGINAL PAGE IS
OF POOR QUALITY

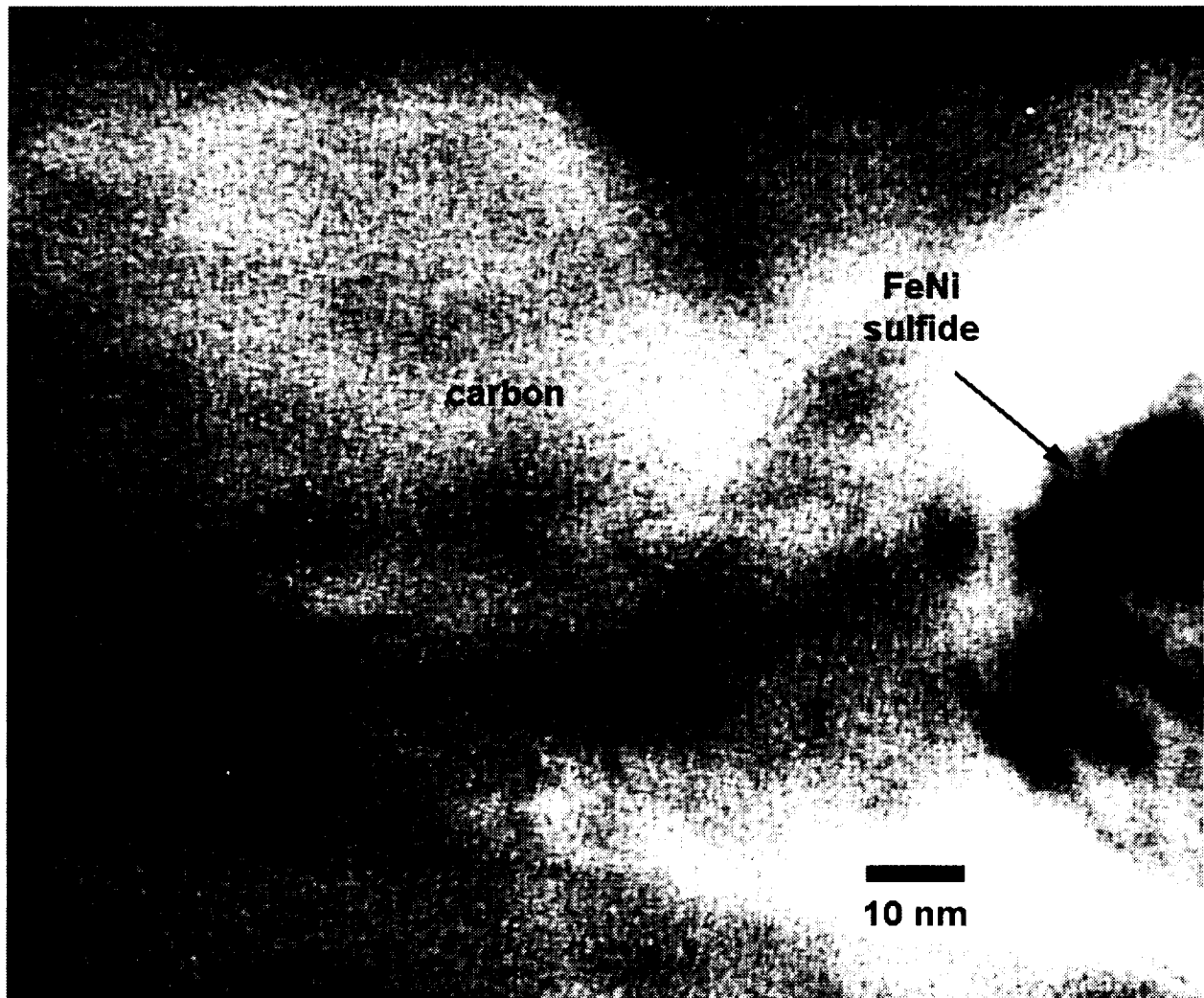


FIGURE 13. High-resolution TEM image of carbonaceous material in L2008E3, showing no evidence for the presence of graphitic layers.

ORIGINAL PAGE IS
OF POOR QUALITY

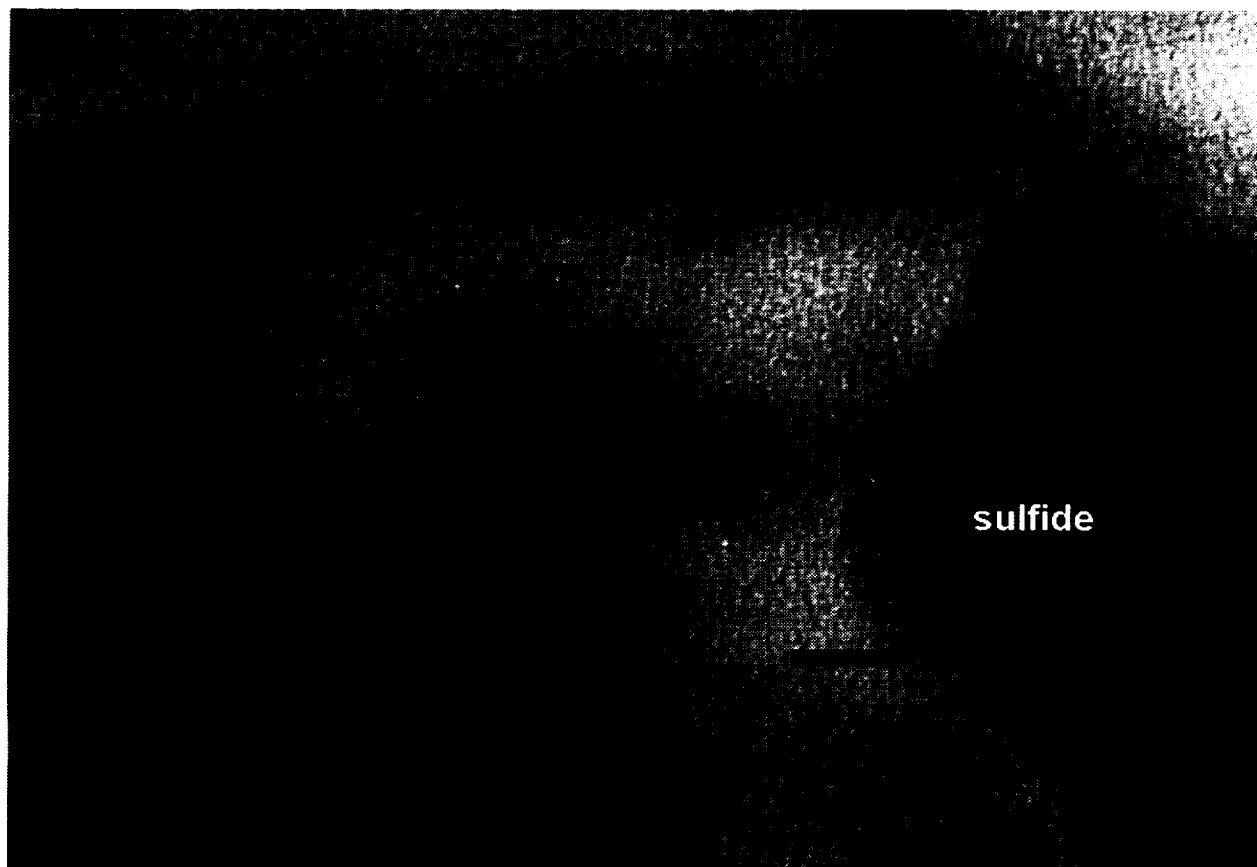


FIGURE 14. High-resolution TEM image of carbonaceous material in L2008F4, showing no evidence for the presence of graphitic layers.

4.2.e. Electron diffraction analysis of carbon in IDPs.

Selected-area electron diffraction (SAED) patterns were obtained from 6 of the analyzed IDPs listed in Table 1. We report diffraction data only for those particles where the carbonaceous material was present in regions approximately as large as the area covered by our smallest selected area aperture (e.g. a circular region ~150 nm in diameter). Even with these precautions, some of the SAED patterns in Figures 15-17 show diffraction spots from other mineral phases (typically Fe-Ni sulfides) that are intergrown with the carbon. The SAED patterns in Figures 15-17 all show only two broad diffuse diffraction rings for the carbonaceous material, with spacings of ~0.205 nm and 0.12 nm. These diffraction data are consistent with the HRTEM data presented in Section 4.2.d and the electron energy-loss spectra given in Section 4.2.g. in that the carbonaceous material is poorly-ordered, with little long range order. The electron diffraction data indicate that the carbonaceous material in these IDPs is largely amorphous.

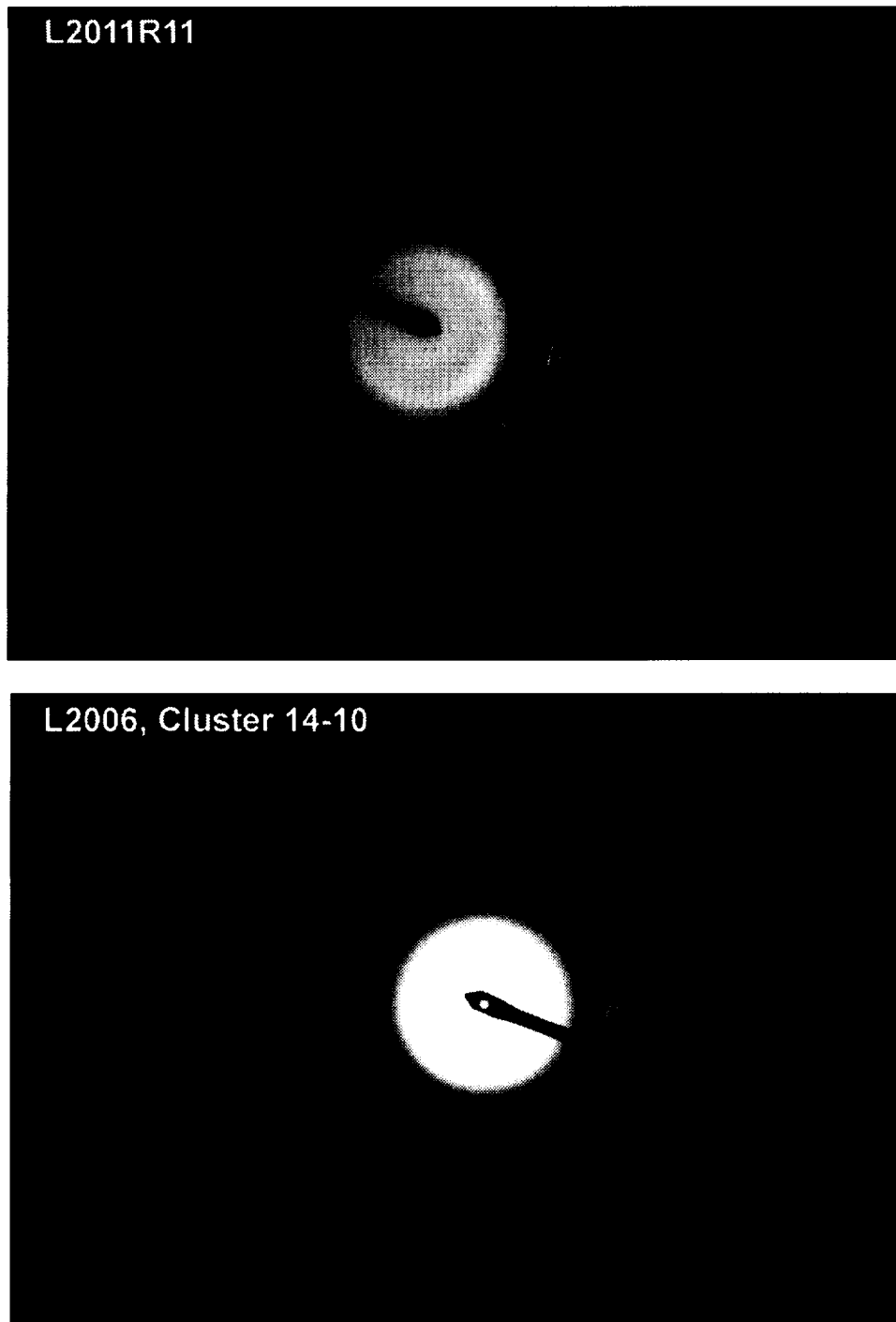


FIGURE 15. Selected-area electron diffraction patterns for carbonaceous material in L2011R11 (top) and L2006, cluster 14-10 (bottom). Small arrow points towards the 0.20 nm spacing of amorphous carbon.

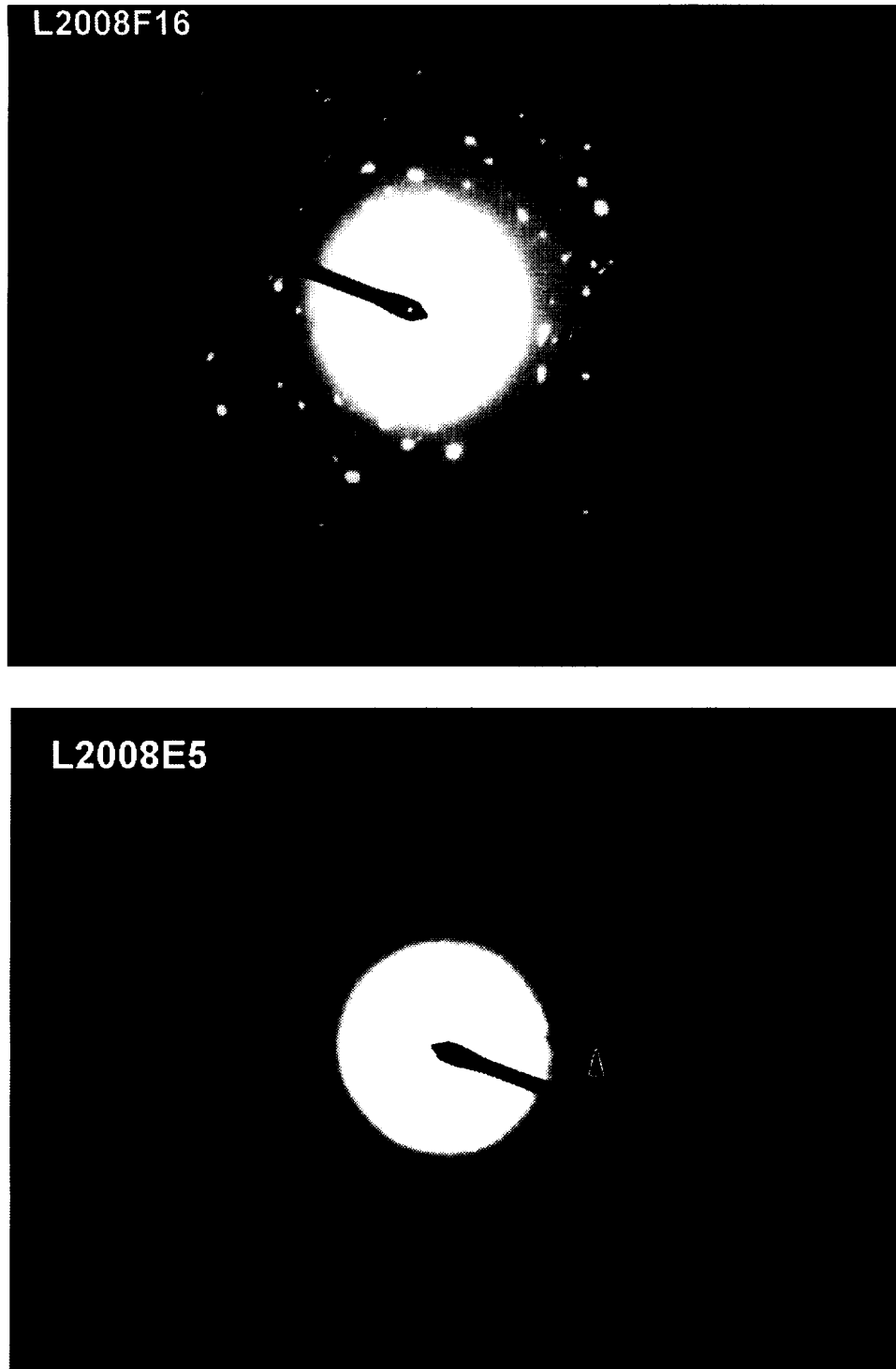


FIGURE 16. Selected-area electron diffraction patterns for carbonaceous material in L2008F16 (top) and L2008E5 (bottom). Small arrow points towards the 0.20 nm spacing of amorphous carbon.

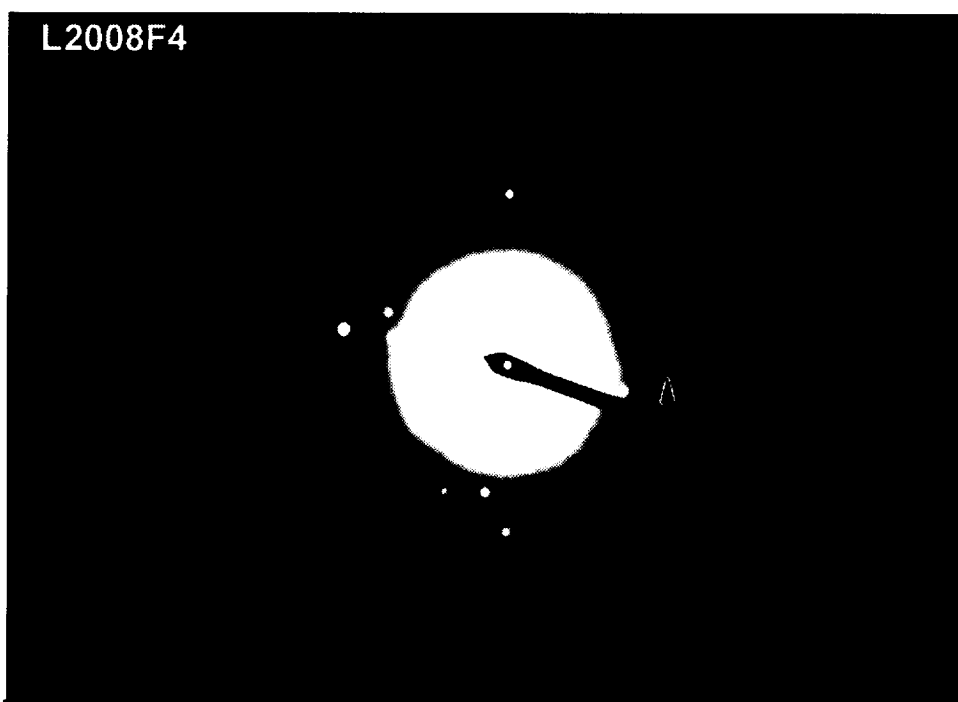
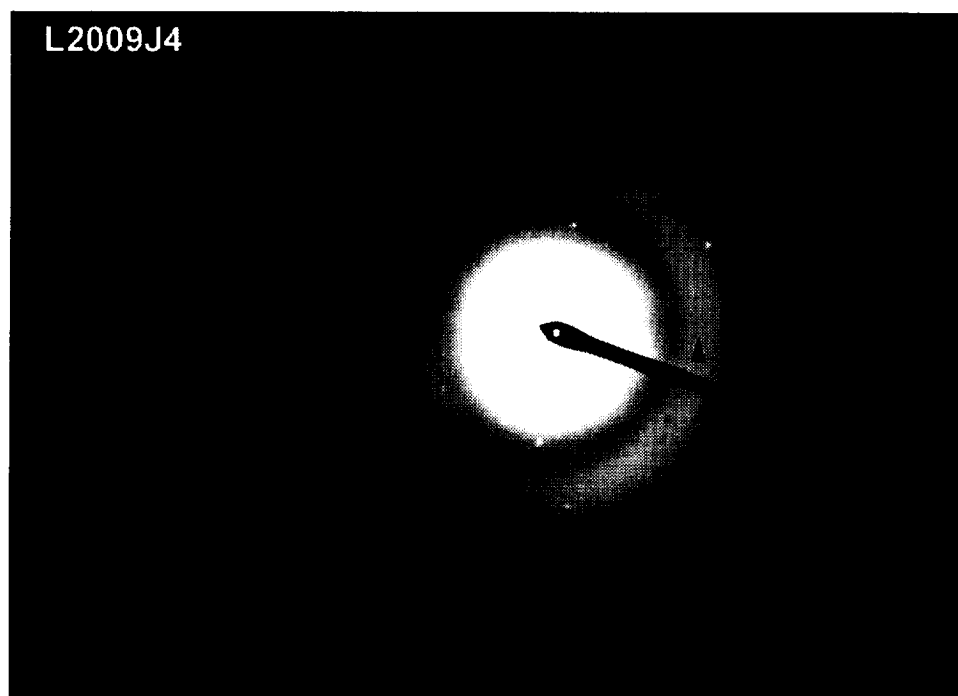


FIGURE 17. Selected-area electron diffraction patterns for carbonaceous material in L2009J4 (top) and L2008F4 (bottom). Small arrow points towards the 0.20 nm spacing of amorphous carbon

4.2.f. Carbon analysis using energy-dispersive x-ray spectrometry.

We obtained quantitative energy-dispersive x-ray (EDX) data from all 10 of the particles listed in Table 1. Our EDX data are tabulated in Table 2 along with data for the Orgueil CI chondrite (for comparison). The data are reported as element-weight % ratios relative to Fe because of the interference from the Si and O peaks that are derived from the SiO thin film support. The C/Fe ratios reported in Table 2 correlate well with the abundance of carbonaceous material observed by TEM imaging in the thin sections (e.g. L2006,14-10 has the highest C/Fe ratio of the analyzed IDPs and also contains the highest modal carbonaceous material in thin section; the converse is true for L2008G9).

Table 2 is a comparison of our thin-film analyses of two of the particles (L2011R11 and L2011A4) with data obtained from the same particles by SEM-EDX bulk particle techniques. There is excellent agreement between the data sets for both techniques except for the C/Fe ratios determined by TEM-EDX which are ~ a factor of 2 greater than the ratio determined in the SEM. The disparity between the C/Fe ratios may be a result of obtaining the thin-film analyses from the sections on the SiO films. The oxygen peak (much of the oxygen is from the SiO substrate) in the TEM-EDX spectra is large relative to the carbon peak, and we may be recording too many counts in the carbon peak that are actually derived from the tail of the oxygen peak. This result suggests that SiO is a less than ideal substrate for carbon analysis.

TABLE 2. Quantitative EDX analyses of IDP thin sections. Data are presented in weight % of the element relative to Fe.

IDP	C/Fe	Mg/Fe	Al/Fe	S/Fe	Ca/Fe	Ni/Fe
L2011R11	1.27	0.56	0.09	0.34	0.05	0.05
L2006,14,10	3.70	0.11	0.08	0.18	n.d.	0.04
L2011A4	1.10	0.97	0.14	0.34	0.09	0.04
L2008F13	2.50	0.25	0.06	0.25	0.01	0.03
L2008G9	0.77	0.74	0.09	0.10	0.03	0.01
L2008F16	1.36	0.62	0.15	0.34	0.01	0.10
L2008E5	1.70	0.72	0.15	0.22	0.03	0.02
L2009J4	0.83	0.55	0.13	0.30	0.05	0.05
L2008E3	0.87	0.46	0.07	0.33	0.04	0.06
L2008F4	1.60	1.00	0.13	0.45	0.06	0.10
Orgueil	0.19	0.51	0.05	0.28	0.05	0.03

TABLE 3. Comparison of quantitative TEM-EDX data compared to data from same particle by SEM-EDX techniques.

IDP	C/Fe	Mg/Fe	Al/Fe	S/Fe	Ca/Fe	Ni/Fe
L2011R11	1.27	0.56	0.09	0.34	0.05	0.05
R11 (SEM)	0.47	0.52	0.06	0.42	0.05	0.05
L2011A4	1.10	0.97	0.14	0.34	0.09	0.04
A4 (SEM)	0.47	0.90	0.09	0.31	0.07	0.03

4.2.g. Carbon analysis by Electron Energy-Loss Spectroscopy.

We have completed electron energy-loss spectroscopy (EELS) measurements of the chemical state of carbon in a total of 15 IDPs. EELS spectra were obtained from thin sections of the 10 particles listed in Table 1, and typical spectra from each particle are illustrated in Figures 18-27. The spectra from all 10 particles are very similar in terms of the near-edge structure exhibited in the carbon k-edge. The carbonaceous material in these IDPs shows the same structure as amorphous carbons. There is no evidence in any of the spectra for poorly-graphitized carbon or graphite. The carbon-bearing materials in these IDPs lack significant long-range order. Several of the analyzed IDPs have been strongly heated during atmospheric entry (see section 4.2.h. Mineralogy section), but there has been no apparent change in the carbonaceous materials in these IDPs with strong heating (i.e. no graphite formation). We have also observed nitrogen associated with the carbonaceous materials in three particles (L2011R11, L2008F13, and L2006, #10). The possibility exists that in L2011R11, the particle may have been contaminated with cyanoacrylate, however, for the other two particles, we can exclude the possibility of contamination during the embedding and sectioning procedures.

We also obtained spectra from 5 additional IDPs (all hydrated IDPs) that had been embedded in epoxy. Most of the hydrated IDPs contain two main forms of carbon, oxidized carbon (carbonates) and "amorphous" carbon, although one IDP (L2006E10) contains no carbonates (Figures 28-32). The distinction between these two forms of carbon is straightforward because of the dramatic differences in the near-edge structure and the large chemical shift of nearly 5 eV in the onset of the edges between carbonate and amorphous carbon (Figure 33). An important result of this study is that all five hydrated IDPs analyzed contain significant amorphous carbon, the amorphous carbon is typically very fine-grained, poorly-crystalline, and is intimately associated with the layer silicates in these particles. L2006J14 is the only one of the 16 IDPs analyzed that contains carbonaceous material that could be termed "poorly-graphitized" carbon because of the development of fine structure in the edge (development of a sharp spike on the σ^* peak and the increased width of the σ^* peak (Figure 32, compare to Figure 34).

Our analyses indicate that there is little structural difference between the carbonaceous material in anhydrous IDPs compared to that in hydrated particles. We have observed however, that the distribution of the carbonaceous material in the two main types of IDPs is different. In anhydrous IDPs, it is common to see extensive regions of carbonaceous material, whereas in hydrated IDPs, the carbonaceous material is intimately mixed with the phyllosilicate matrix. The EELS analysis is particularly useful in cases where the carbon-bearing phases are fine-grained and widely dispersed. For example, in our initial TEM analysis of IDP L2005R7, we did not identify carbonates using the traditional techniques of EDX analyses and electron diffraction, whereas our subsequent analysis using EELS revealed that minor carbonates are present in this particle. Most of these results were summarized in a LPSC XXV abstract, and in an abstract published

in *Meteoritics* in July of 1994 (copies of these abstracts are attached in the Appendix-Publications).

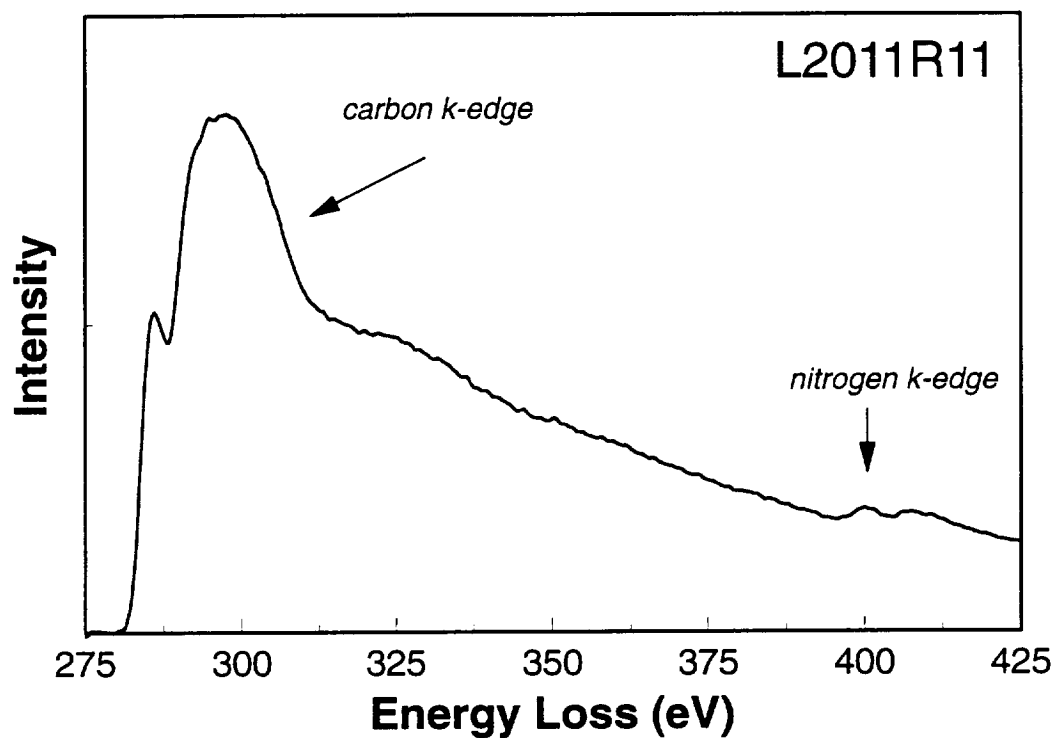


FIGURE 18. EELS spectrum for carbonaceous material in L2011R11. Note the small peak at ~400 eV which corresponds to the nitrogen k-edge.

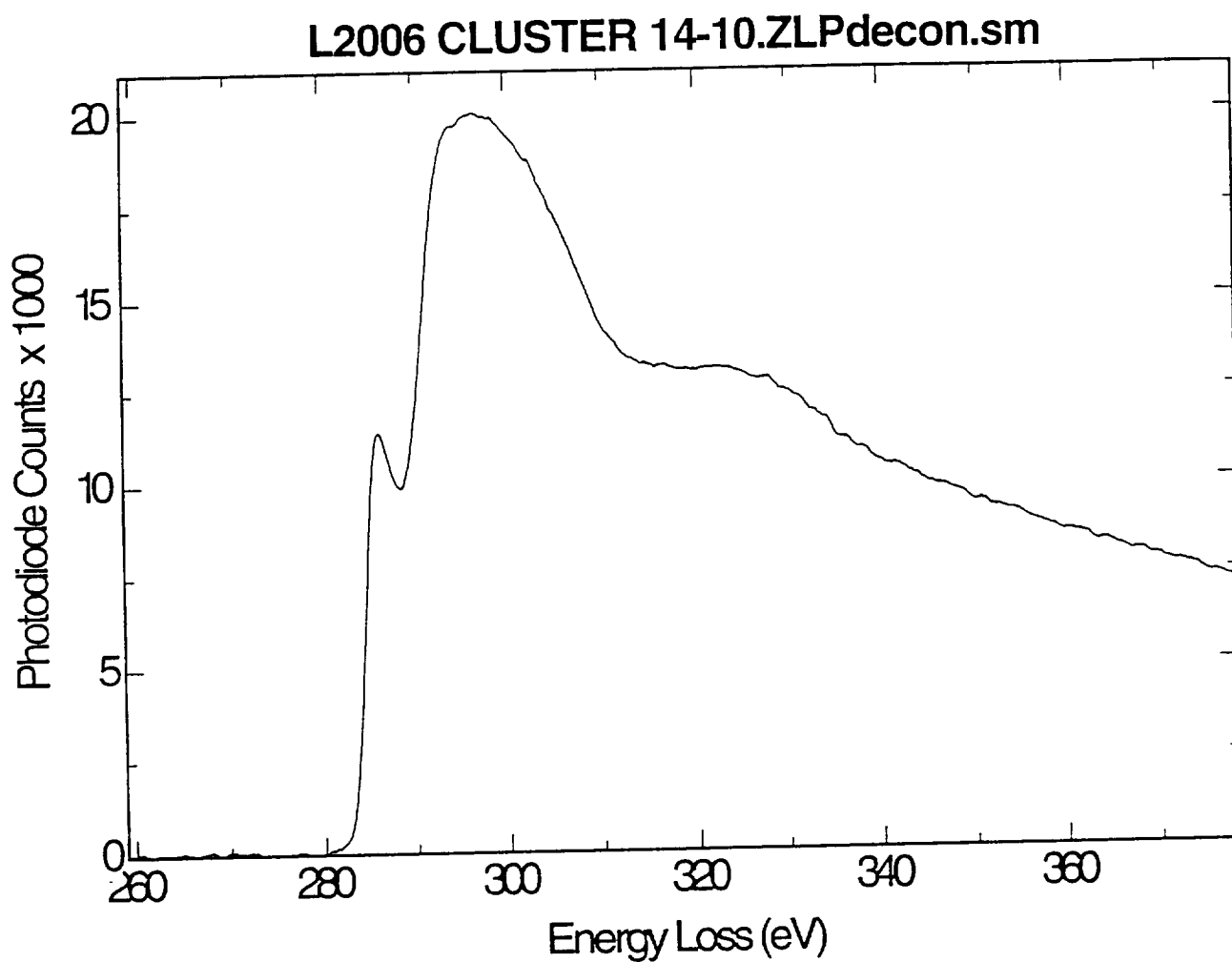


FIGURE 19. EELS spectrum for carbonaceous material in L2006, Cluster 14, Particle 10. Both the vesicular and featureless carbon show the same spectrum.

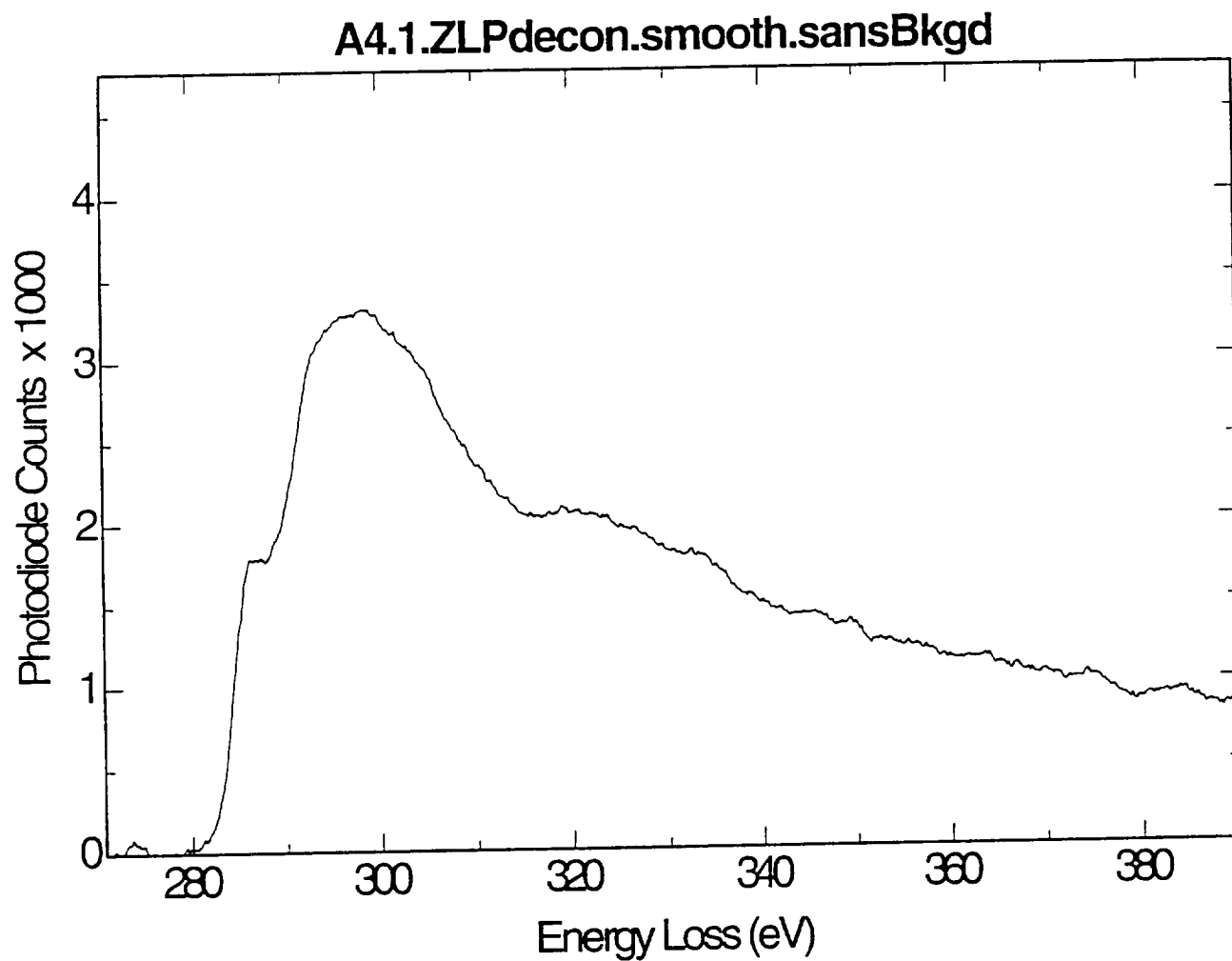


FIGURE 20. EELS spectrum for carbonaceous material in L2011A4. Although this particle was strongly heated, there is no evidence for the development of graphite.

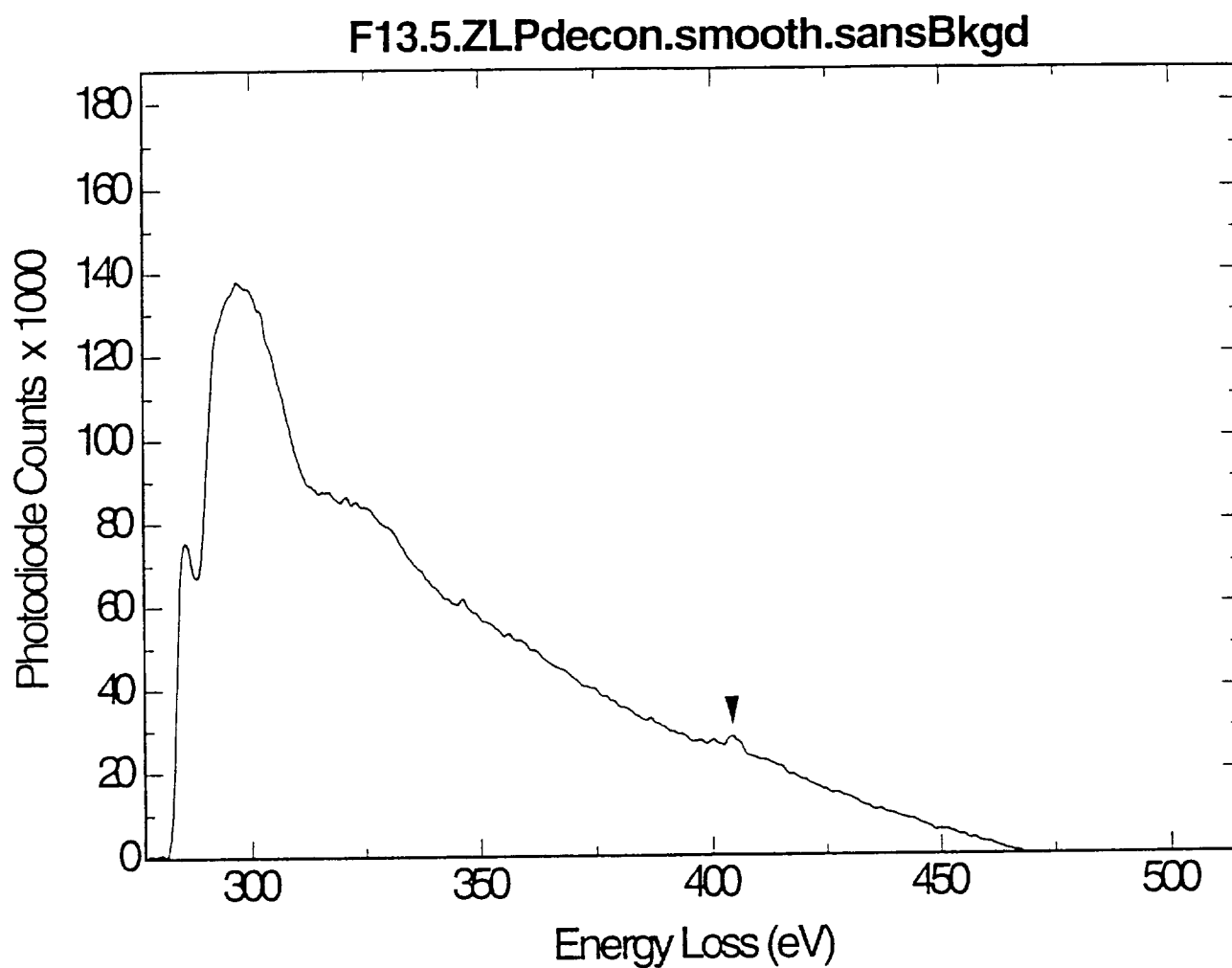


FIGURE 21. EELS spectrum for carbonaceous material in L2008F13. Note the small peak at ~400 eV which corresponds to the nitrogen k-edge.

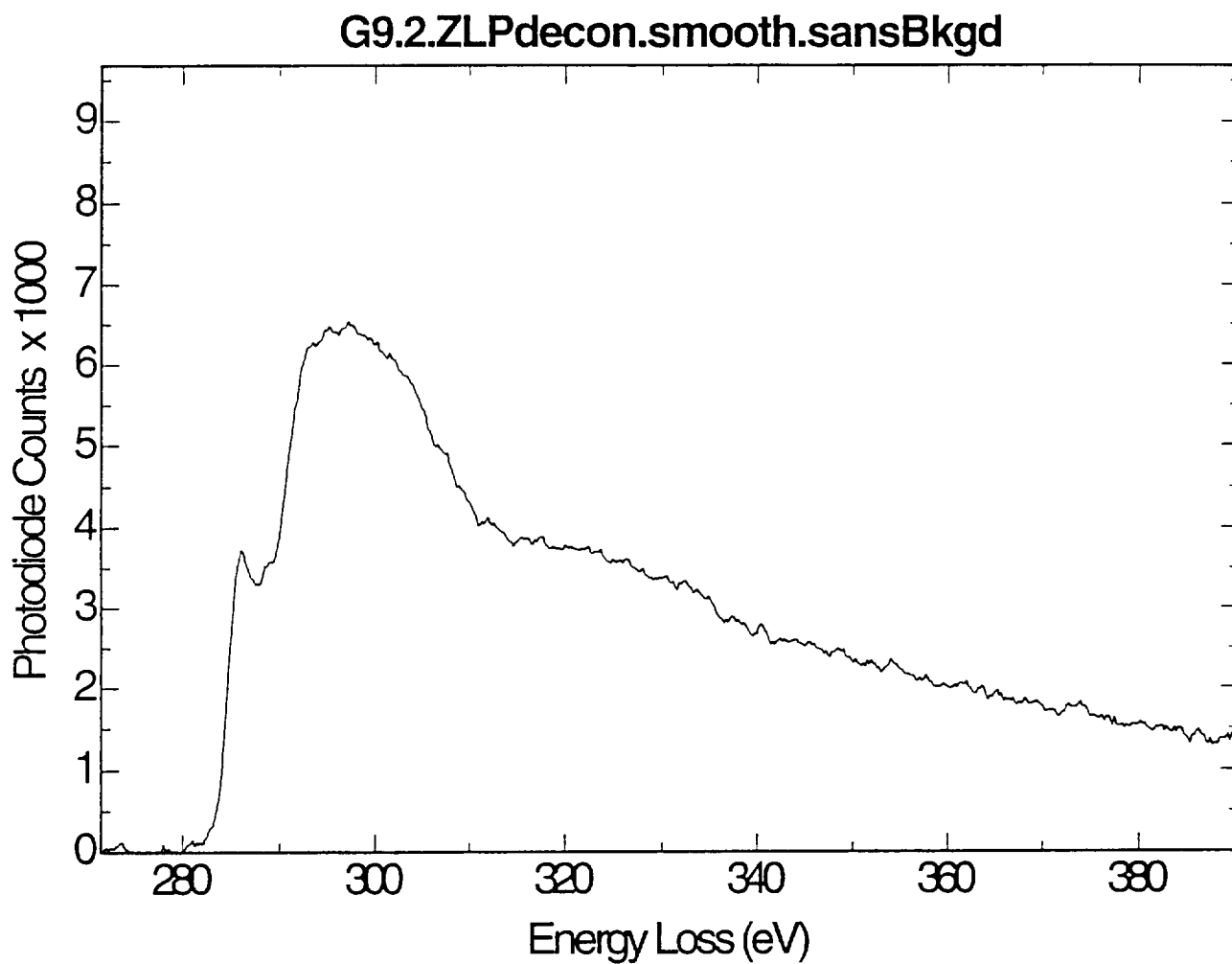


FIGURE 22. EELS spectrum for carbonaceous material in L2008G9.

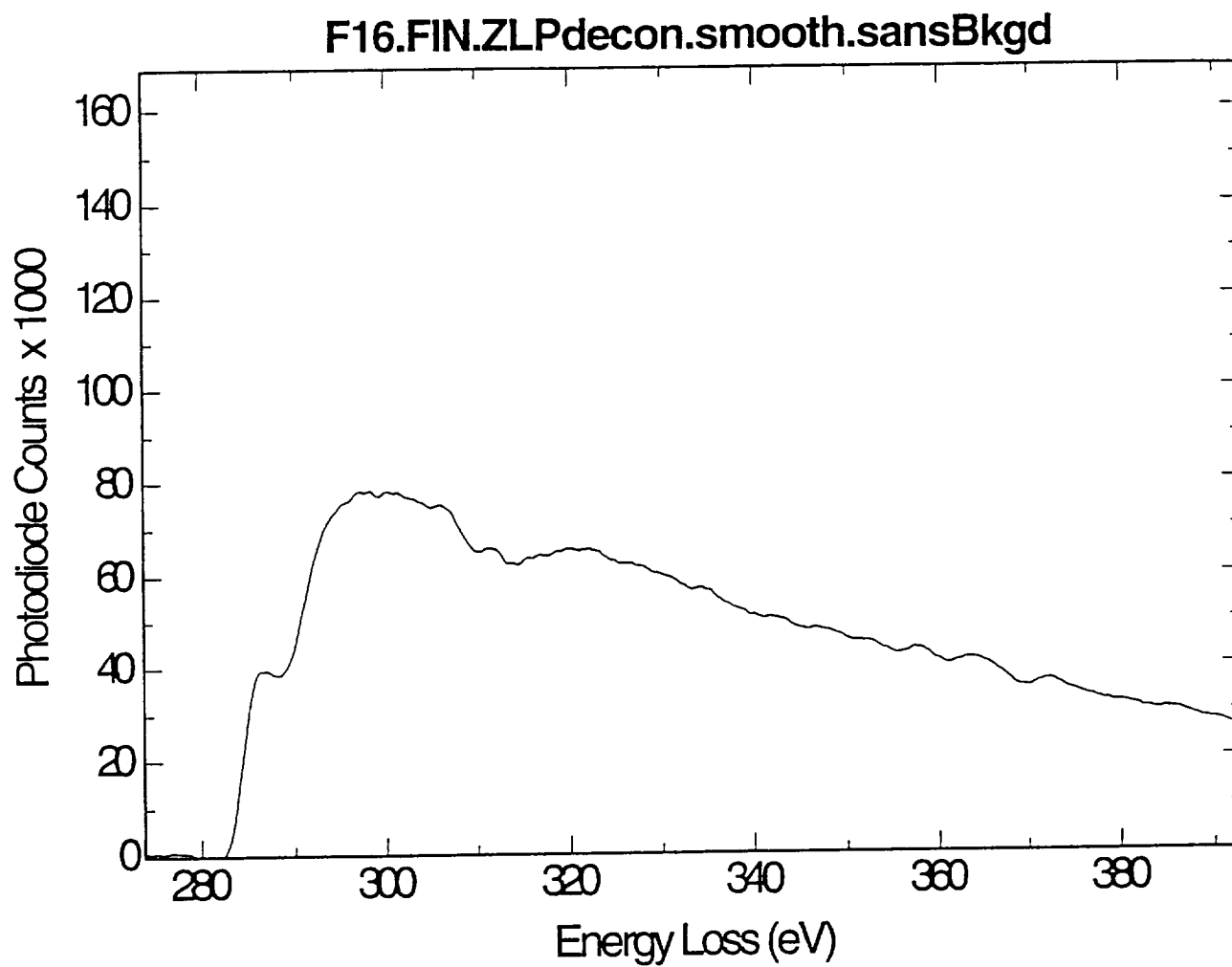


FIGURE 23. EELS spectrum for carbonaceous material in L2008F16. This hydrated IDP contains only amorphous carbonaceous material; no carbonates are observed.

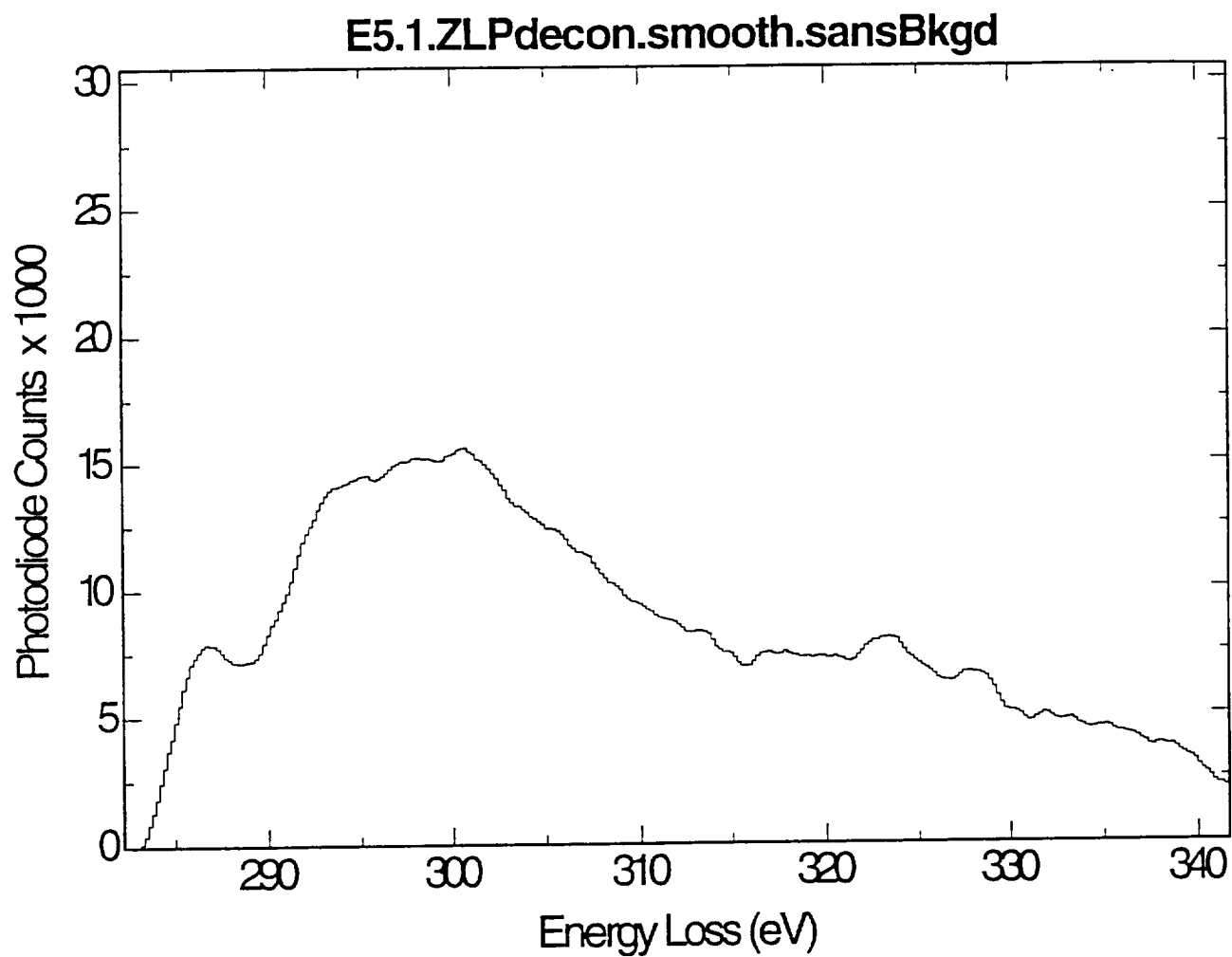


FIGURE 24. EELS spectrum for carbonaceous material in L2008E5.

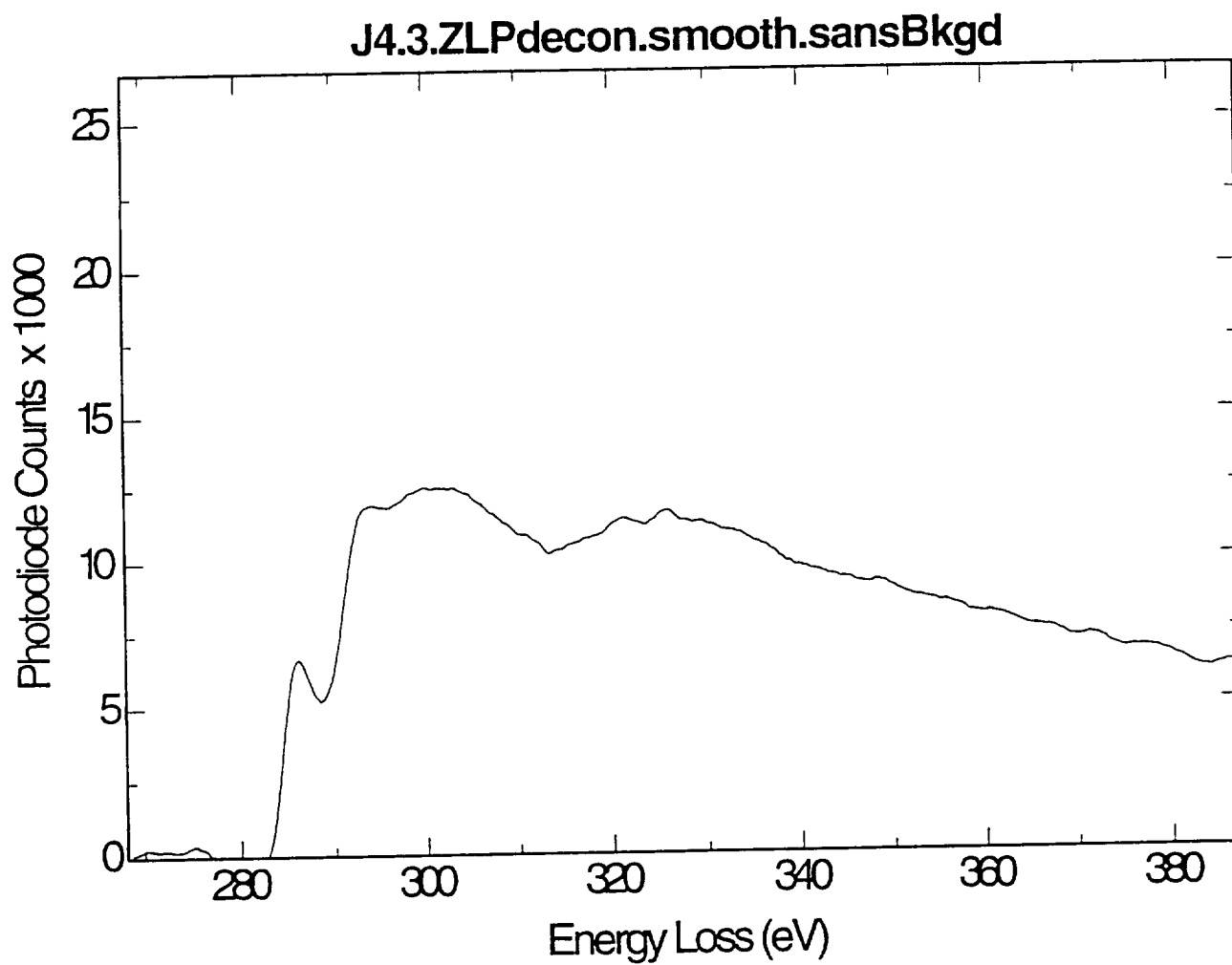


FIGURE 25. EELS spectrum for carbonaceous material in L2009J4.

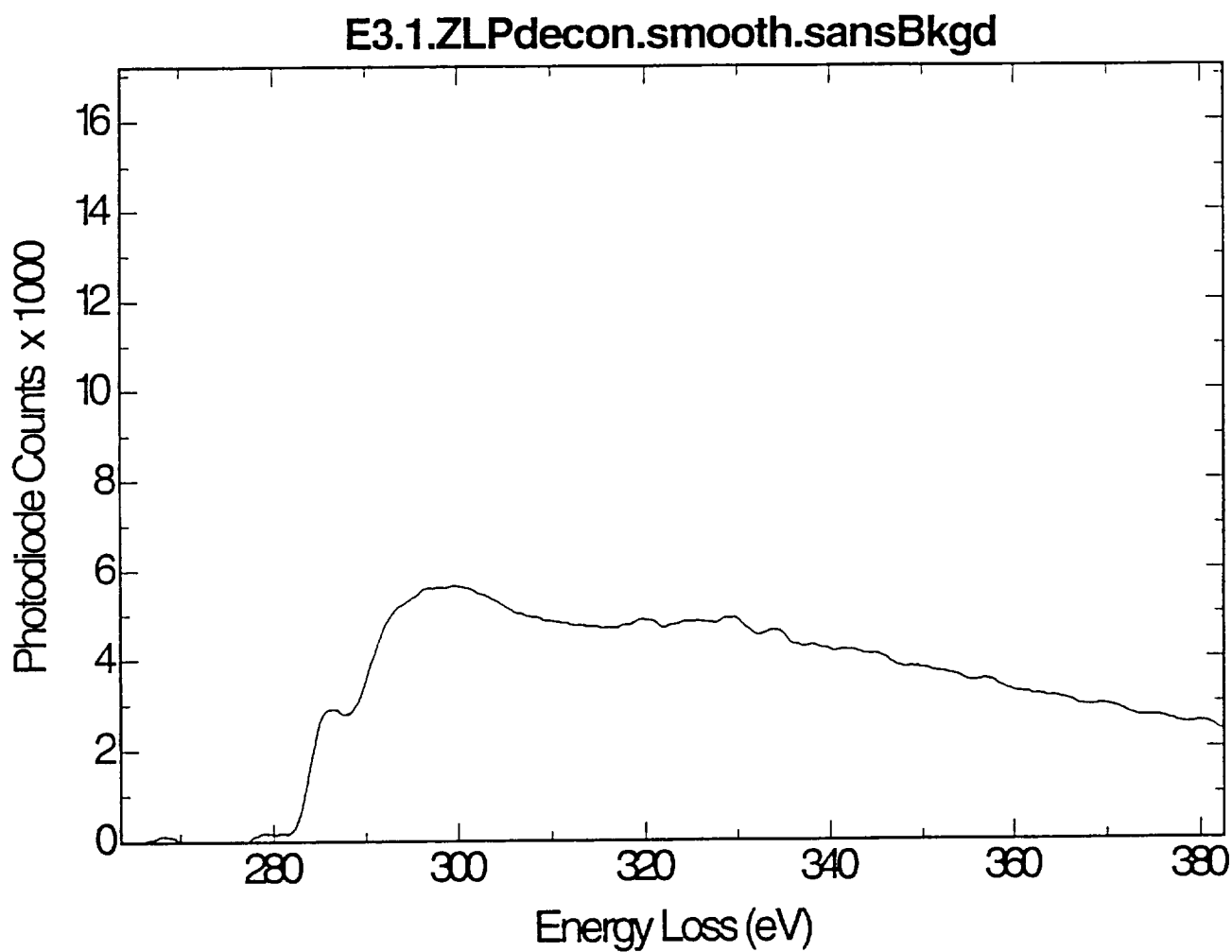


FIGURE 26. EELS spectrum for carbonaceous material in L2008E3.

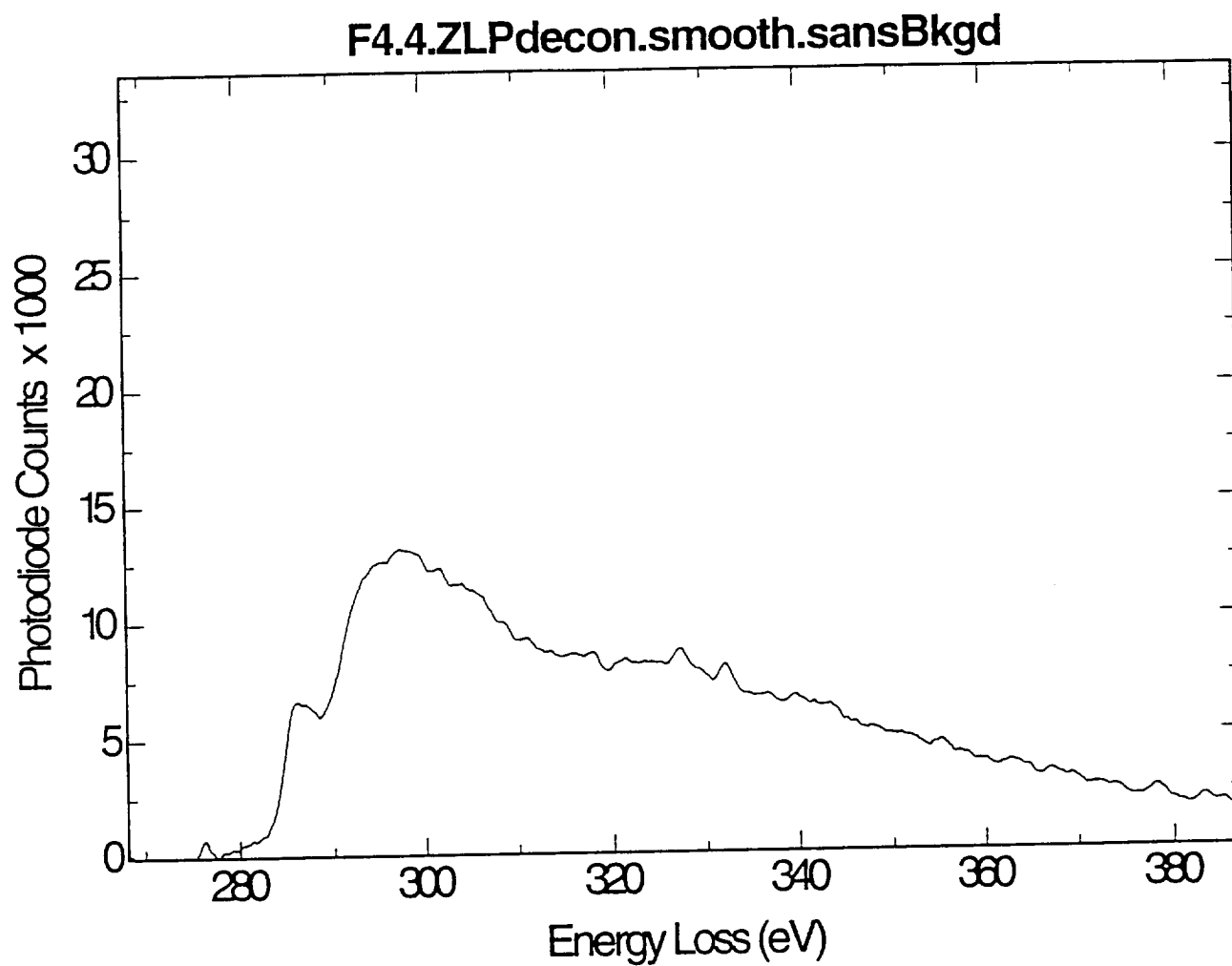


FIGURE 27. EELS spectrum for carbonaceous material in L2008F4.

L2006G1

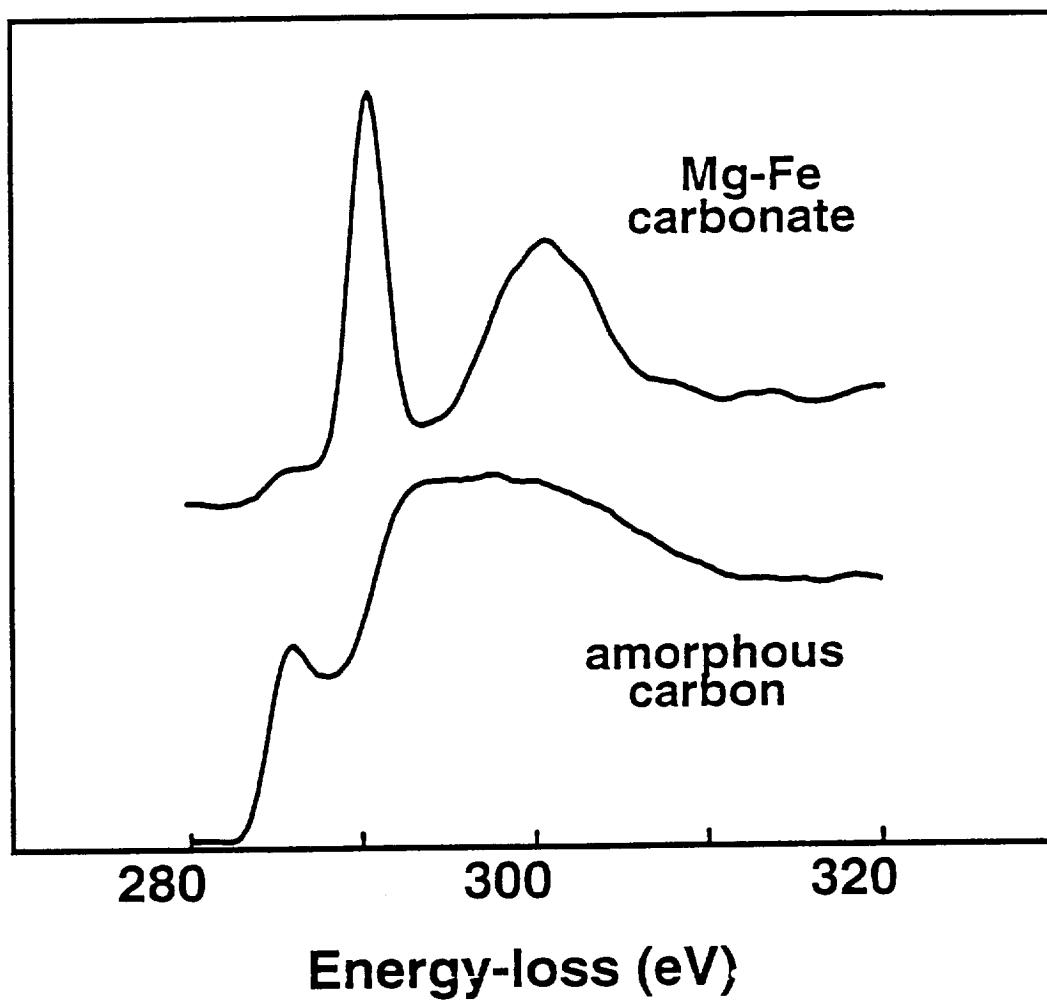


FIGURE 28. EELS spectrum for carbon-bearing materials in L2006G1, a hydrated IDP containing two types of carbon, elemental and carbonate.

L2006F10

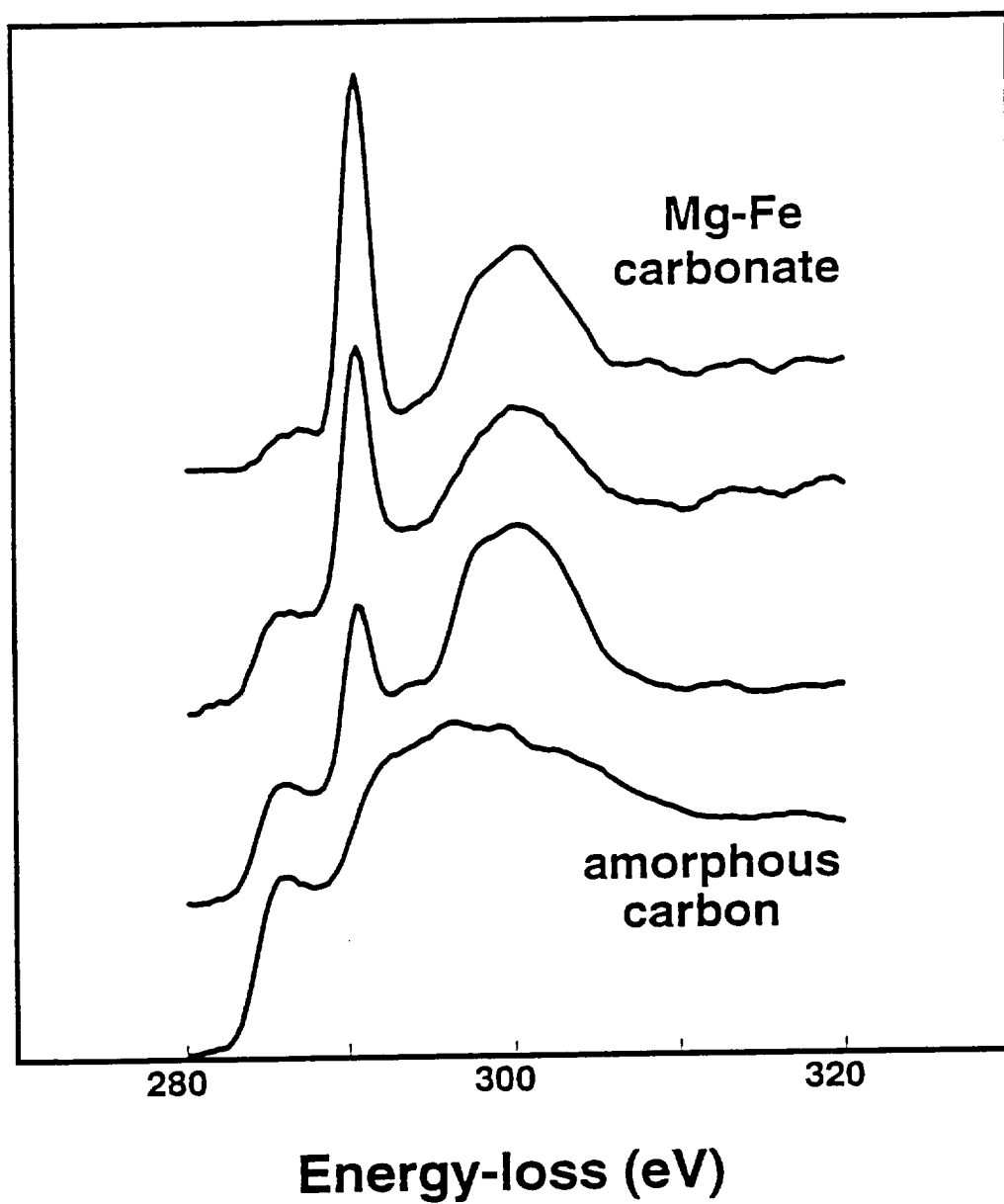


FIGURE 29. EELS spectrum for carbon-bearing materials in L2006F10, a hydrated IDP containing two types of carbon, elemental and carbonate.

L2005R7

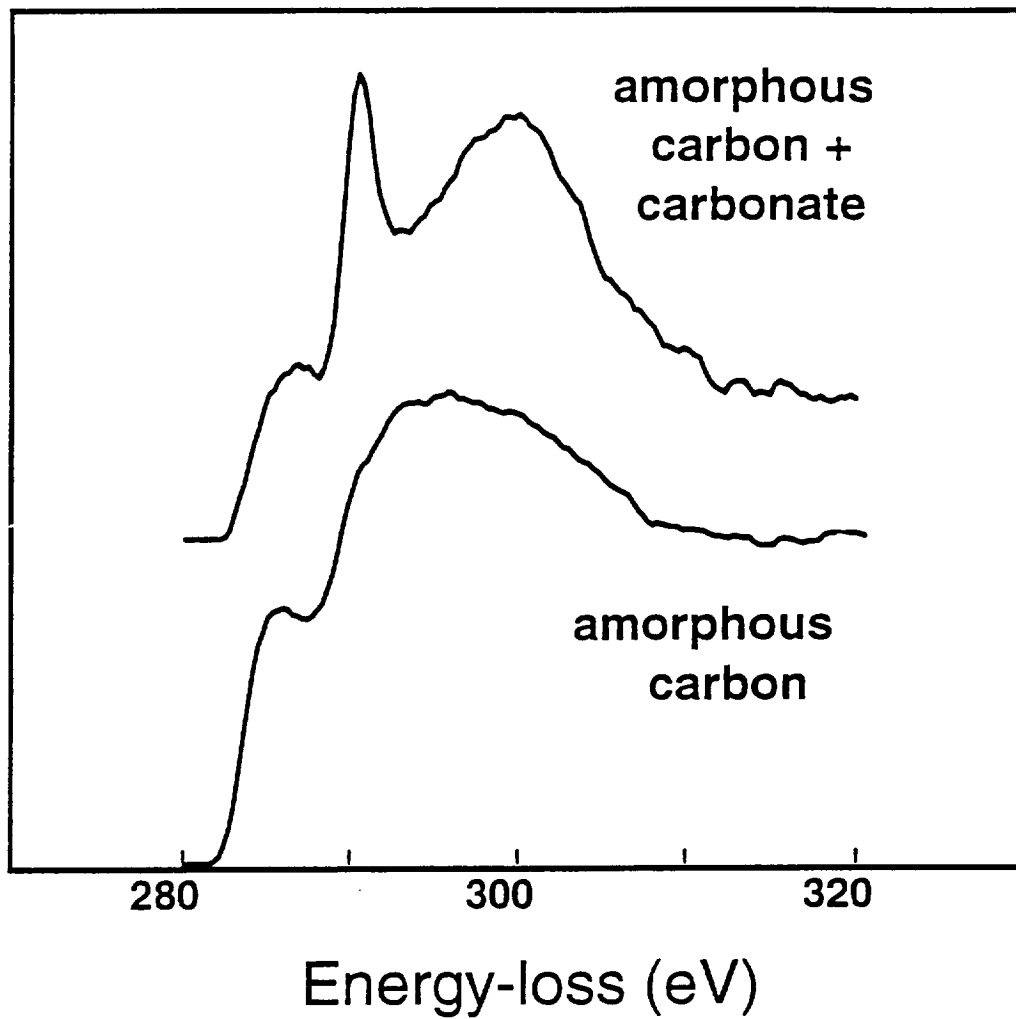


FIGURE 30. EELS spectrum for carbon-bearing materials in L2005R7, a hydrated IDP containing two types of carbon, elemental and carbonate. Carbonates are rare and fine-grained.

L2006E10

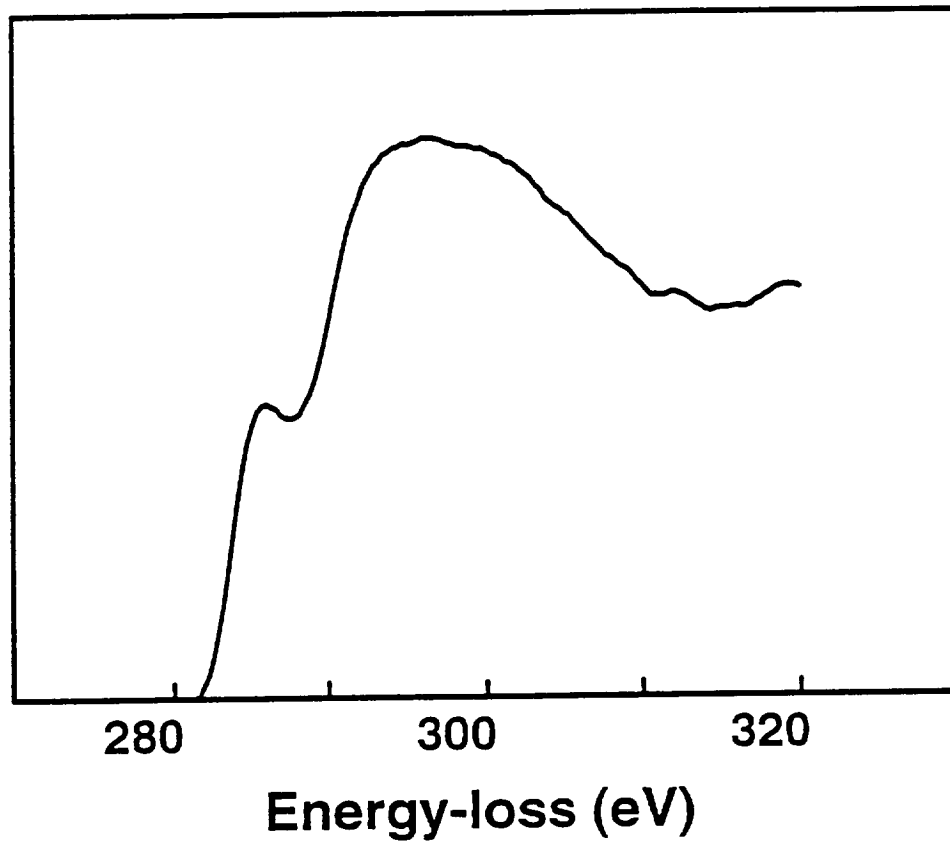


FIGURE 31. EELS spectrum for carbon-bearing materials in L2006E10, a hydrated IDP containing only elemental carbon.

L2006J14

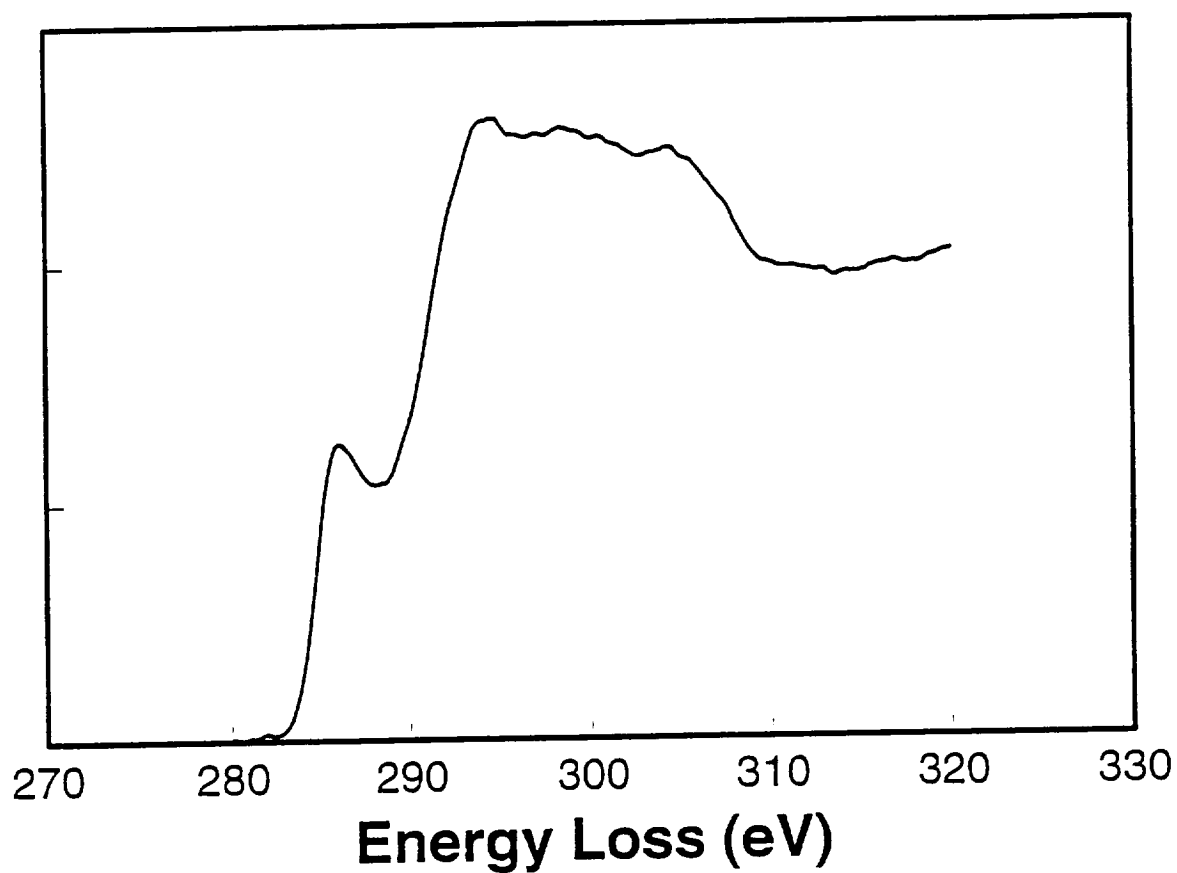


FIGURE 32. EELS spectrum for carbon-bearing materials in L2006J14, a hydrated IDP containing poorly-graphitized carbon. Compare to Figure 34.

"Finger-print" for carbonate

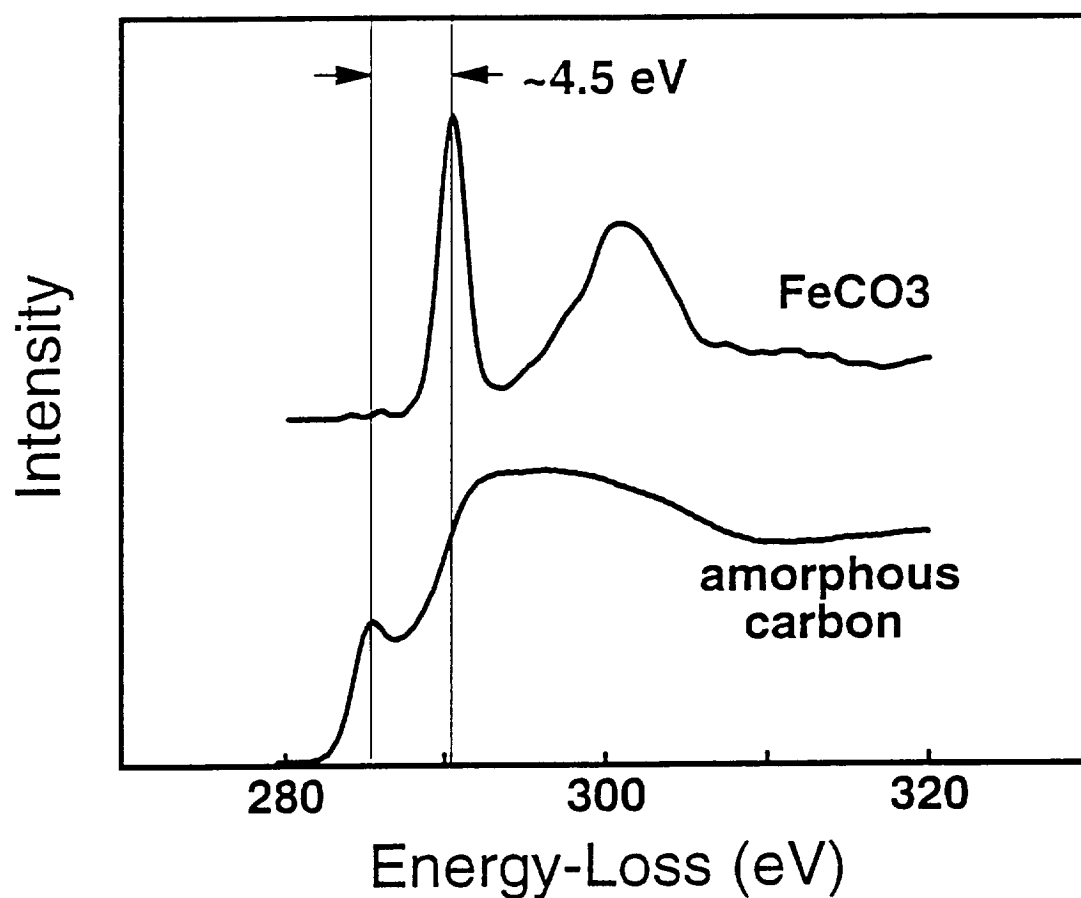


FIGURE 33. EELS spectrum for the carbon k-edge in siderite (FeCO_3) and in amorphous carbon (thin film standard) showing the chemical shift of ~ 4.5 eV and the dramatically different edge-structure for oxidized versus elemental carbon.

k-edges in elemental C

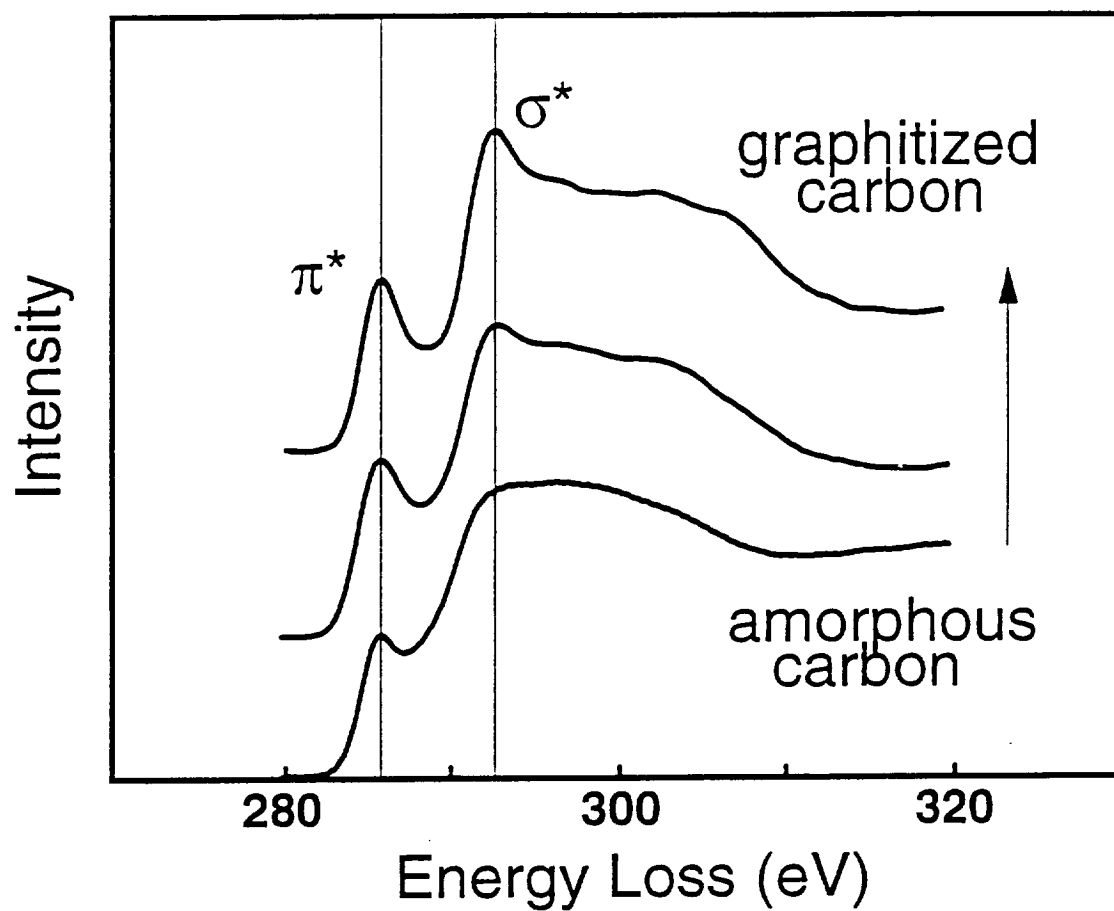


FIGURE 34. EELS spectrum for elemental carbons showing the changes in the near-edge structure with increasing structural order.

4.2.h. Mineralogy and mineral chemistry of major phases in analyzed IDPs.

The following are descriptions of the mineralogy, petrography, and mineral chemistry of the 10 IDPs listed in Table 1.

L2011R11 is a chondritic-porous anhydrous IDP ~20 μm in size whose mineralogy is dominated by low-Ca pyroxene, low-Ni Fe-sulfides, GEMS (glass with embedded metal and sulfides), and carbonaceous material. Mineral grain sizes are variable with pyroxene and sulfide grains ranging up to 1 μm in size; whereas GEMS are typically 0.1 to 0.3 μm in size. A thin, discontinuous magnetite rim occurs on parts of the external surface of the particle. Pyroxenes in R11 contain solar flare tracks with a track density of $\sim 4 \times 10^{10}$ tracks/ cm^2 . A sputtered rim was observed on one pyroxene grain exposed at the particle surface. Carbonaceous material occurs throughout the particle and serves as a matrix bonding the silicates and sulfides together. The carbonaceous material shows two distinct textures, 1) uniform, featureless regions up to ~ 0.1 μm in size, and 2) regions of vesiculated carbon that occur near the particle surface as well as in the interior. High-resolution imaging and electron energy-loss spectroscopy (EELS) data show that the carbon-rich material is amorphous and lacks significant long-range order. EELS data for the carbon k-edge from the two textural varieties of carbon in R11 are identical. A major finding of this study was the observation of significant nitrogen concentrations within the carbonaceous material. Nitrogen was identified by its k-edge at ~ 400 eV in the EELS spectra. We believe that the nitrogen is indigenous to the IDP, but we are also completing exhaustive tests in order to exclude the possibility of contamination.

L2006, Cluster 14, particle #10 is a fragment from a larger particle that fragmented on the collector surface. Previous work on fragments associated with this cluster have shown them to be unusually carbon-rich (Thomas *et al.* 1993, *Geochimica et Cosmochimica Acta*, vol. 57, 1551). L2006,14,10 is an irregularly shaped particle that is volumetrically dominated by carbonaceous material with minor interspersed GEMS (glass with embedded metal and sulfides). The carbonaceous material shows no evidence for long range-order either by EELS or by electron diffraction.

L2011A4 is a compact, anhydrous IDP whose mineralogy is dominated by pyroxene and olivine grains with equilibrated Mg/Fe ratios, aluminosilicate glass, minor Fe-Ni sulfides, and a thin discontinuous magnetite rim. The mineralogical features of this particle are consistent with strong heating during atmospheric entry.

L2008F13 is a large (~ 20 μm) carbon-rich, porous, anhydrous IDP. F13 contains abundant pigeonite, FeNi sulfides (low Ni), and GEMS (glass with embedded metal and sulfides) all of which are held together by a carbonaceous matrix.

Lobes of the silicate and sulfide-rich areas are covered with thin magnetite rims. EELS data from the carbonaceous material indicate that nitrogen is associated with the carbon, and there are indications that it is localized in "nitrogen hotspots".

L2008G9 is a strongly heated hydrated IDP that contains coarse-grained Fe-sulfides ($\sim 0.5 \mu\text{m}$) that are mantled by magnetite rims on their exposed surfaces. The phyllosilicates are Fe-rich ($\text{Fe}/(\text{Fe}+\text{Mg}) \text{ atomic} \approx 0.8$), very-poorly-crystalline, and are intergrown with fine-grained Fe sulfides and magnetite. We did not observe any basal spacings in the fibrous phyllosilicates and we presume they were destroyed during atmospheric entry.

L2008F16 is only the second hydrated IDP of the 10 particles that were analyzed. L2008F16 is a low porosity IDP whose mineralogy is dominated by coarse- and fine-grained phyllosilicates. High-resolution TEM images show basal spacings of 1 nm which indicates that the phyllosilicates in F16 are saponite. The saponite has a $\text{Mg}/(\text{Mg}+\text{Fe})$ ratio of ~ 0.70 which is typical for saponite-rich IDPs. FeNi sulfides ($\text{Ni}/(\text{Ni}+\text{Fe}) \approx 0.1$) are fine-grained and dispersed throughout the particle, although towards the rim of the particle they have decomposed to magnetite during atmospheric entry. No carbonates were observed in F16.

L2008E5 is an anhydrous IDP containing major coarse-grained pyroxene ($\text{Mg}/(\text{Mg}+\text{Fe}) = \sim 0.75$) which shows little compositional variation throughout the particle and fine-grained (typically $< 0.2 \mu\text{m}$) low Ni sulfides. The particle is surrounded with a discontinuous magnetite rim which is evidence for atmospheric entry heating. Carbonaceous material is featureless and is not abundant. It occurs in small regions up to a few tenths of a micrometer in size and contains embedded sulfides and silicate grains.

L2009J4 is another large ($\sim 20 \mu\text{m}$) anhydrous IDP that is dominated by coarse-grained sulfides and silicates. The sulfides are up to $5 \mu\text{m}$ in size and are very Ni-poor. Silicates include both pyroxene and olivines up to $1 \mu\text{m}$ in size with equilibrated $\text{Mg}/(\text{Mg}+\text{Fe})$ ratios (atom ratio of ~ 0.7). GEMS (glass with embedded metal and sulfides) occur in the thin sections and comprise ~ 10 volume % of the thin sections. No obvious magnetite rim was observed. The olivines contain significant Mn, but the Mn content is less than the Fe content. L2009J4 has a low porosity; much of the space between mineral grains is filled with featureless carbonaceous material which mantles the mineral grains.

L2008E3 is a highly-porous, anhydrous, spheroidal particle. The apparent porosity in thin section approaches 50%. E3 contains abundant, fine-grained ($\sim 300 \text{ nm}$ in diameter), somewhat equant pyroxene and sulfide grains. Pyroxenes have $\text{Mg}/(\text{Mg}+\text{Fe})$ atom ratios of ~ 0.8 . The sulfides contain 5-10 mol% Ni. Small regions of carbonaceous material occur between the mineral grains.

components of E3 have thin, discontinuous magnetite rims on exposed, outermost surfaces.

L2008F4 is a classic porous anhydrous IDP. Its mineralogy is dominated by nearly end-member enstatite, which occurs as platelets and as equant grains. The enstatite platelets show a mixture of the clino- and ortho- polytypes. The fine-grained sulfides have a uniform Ni content of ~10 mol%. GEMS (glass with embedded metal and sulfides) are the major components in F4. Carbonaceous material is evenly distributed throughout the particle and occurs between mineral grains and as extensive regions up to 0.5 μm in size.

4.1.i. Reflectance spectroscopy of IDPs.

We have obtained reflectance spectra for 38 chondritic interplanetary dust particles (Figures 35 and 36). These spectra were acquired in dark-field mode over the visible wavelength range (370-800 nm) using a Zeiss MPM400 light microscope equipped with a halogen light source, high-power objectives, and a spectrophotometer with a photomultiplier tube detector. Reflectance spectra are collected from IDPs mounted on glass slides with a measuring aperture that is of the same size as the analyzed particle. All data are reported relative to a pressed barium sulfate pellet which has essentially 100% reflectance over the visible range.

The mineralogy and petrography of only a few of these particles have been determined in detail, but several interesting trends are observed including: 1) IDPs, in general, have albedos and spectral shapes that are comparable to the carbonaceous chondrite meteorites; 2) IDPs dominated by large mineral grains tend to have high reflectance values (typically 30% or more); and 3) the most carbon-rich IDPs tend to have the lowest albedos, although there are low albedo particles that are not carbon-rich.

The reflectance spectra in Figure 35 from L2005, Cluster 8, are included in a manuscript by K. L. Thomas *et al.* that is in revision for *Geochimica et Cosmochimica Acta*. The spectra from L2005, Cluster 31 are included in an abstract submitted by K. L. Thomas *et al.* to the XXVI Lunar and Planetary Science Conference (see Appendix-Publications)

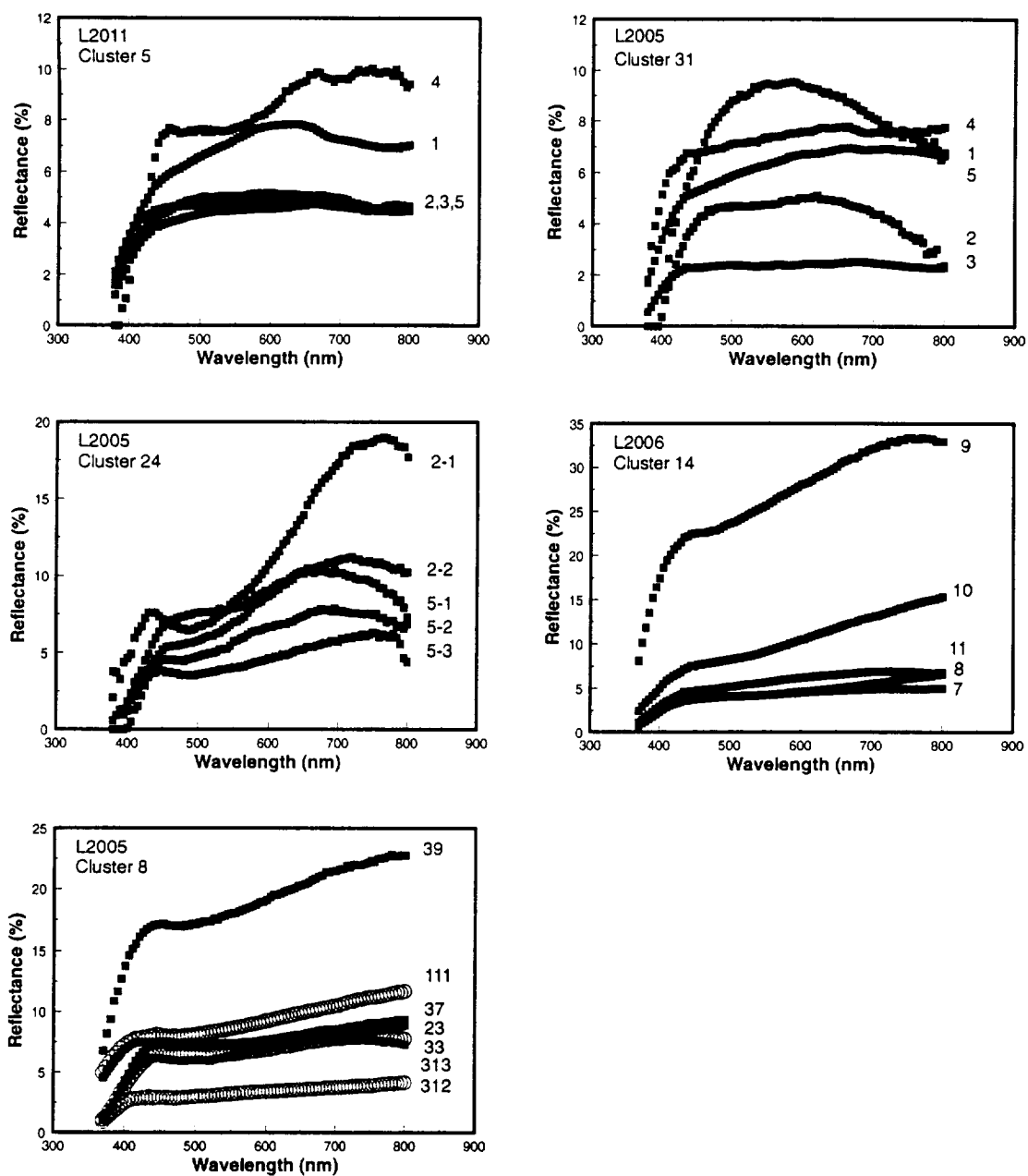


FIGURE 35. Reflectance spectra for multiple IDPs from various clusters from the large-area collectors L2005, L2006, and L2011.

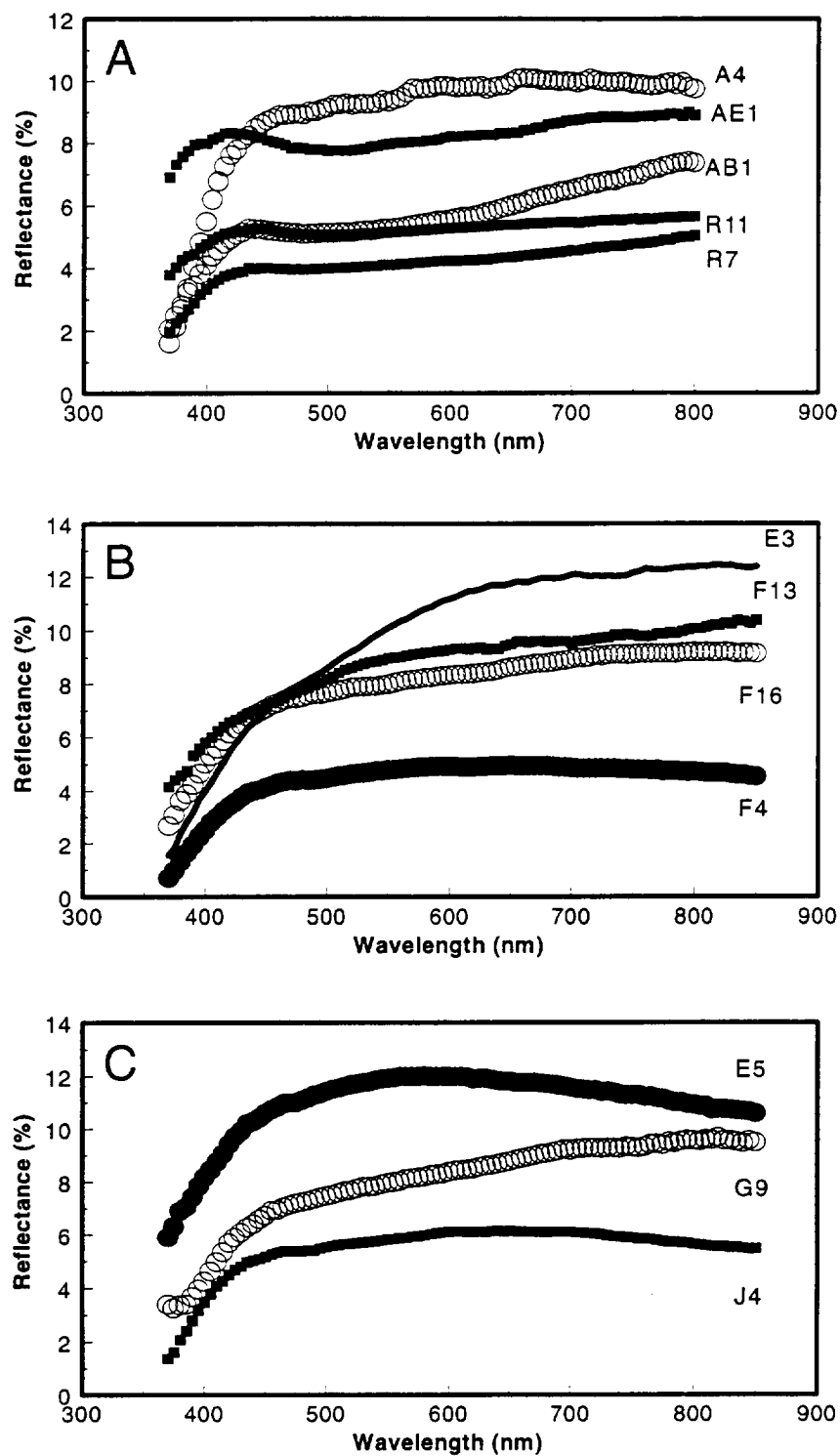


FIGURE 36. Reflectance spectra for individual IDPs. Legend: A) L2011A4, L2011R11, L2011R7, L2005AB1, and L2005AE1. B) L2008E3, L2008F13, L2008F16, and L2008F4. and C) L2008E5, L2008G9, and L2009J4.

SECTION 4.2 ANALYZE SELECTED LUNAR SAMPLES USING (TEM).

4.2.a. Embedding and sectioning selected lunar samples.

Transmission electron microscope specimens were prepared using two main methods, ion-milling and ultramicrotomy. For the studies of opaque assemblages in high-Ti lunar basalts (Subtasks 4.2b-d) we extracted 5 individual regions (3 mm in diameter) from a petrographic thin section of Apollo 17 basalt 70035, attached them to copper support grids, and ion-milled the specimens with 4 kV argon ions until they were electron transparent. For the analyses of lunar soils (subtasks 4.2e-i), multiple aliquots (more than 3 preparations for each soil) of the <20 μm sieve fractions of several lunar soils were embedded in low viscosity epoxy, and TEM specimens were prepared by ultramicrotomy. We embedded samples of the following lunar soils: 10084, 61221, 61181, 67701, 72501, and 78221. The thin sections (typically 50-80 nm thick) were analyzed using a JEOL 2010 (200kV) transmission electron microscope equipped with a LaB_6 filament, a thin-window energy-dispersive x-ray detector, and a GATAN 666 parallel EELS spectrometer.

4.2.b. TEM studies of opaque assemblages in high-Ti basalts.

We have completed our transmission electron microscope studies of opaque assemblages in the Apollo 17 basalt 70035. We used a combination of high-resolution TEM imaging and electron diffraction to characterize the opaque assemblages in this basalt, with particular emphasis on the reported subsolidus reduction features. The opaque assemblages analyzed in this study were dominated by ilmenite with lesser rutile and spinel exsolutions, and traces of Fe metal. We did not observe any rimmed armalcolite grains in the thin sections provided by NASA. We obtained detailed analyses of 12 opaque assemblages in 70035. The general trends are described below.

Rutile forms epitactic intergrowths (coherency in 2 dimensions) with the host ilmenite. This reaction texture is structurally controlled such that the (100) planes of rutile are parallel to the basal plane of ilmenite (0001), and the [001] axis of rutile is coincident with the [110] axis of ilmenite (these orientation relationships are illustrated in Figures 37a and 37b). Three main types of rutile exsolution lamellae were observed: Type I, which consist of homogeneous rutile lamellae up to a few micrometers wide that contain only sparse defects (Figure 38); Type 2 lamellae contain a high density of stacking faults and further exsolution of oxygen-deficient titanium oxides (magneli phases) as thin lamellae from 1 to 50 nm in width (see Figure 39), and Type III, which resemble the type II lamellae with the exception that they also contain a generation of exsolved ilmenite (Figure 40). The electron diffraction patterns from the magneli phases in the Type II rutile exsolutions are complicated by the multiple orientations of the

lamellae (mostly along the {121} planes of the host rutile). The electron diffraction patterns from the Type II and III lamellae contain reflections with larger periodicities than are allowed for the unit cell of rutile. The most common periodicity observed is a spacing of 0.73 nm parallel to (011) of rutile which is consistent with the presence of either Ti_7O_{13} or Ti_9O_{17} , both of which have an ~ 0.73 nm spacing along their c-axes (Figure 41). The electron diffraction patterns are not consistent with any of the more reduced magneli phases (such as Ti_4O_7 , Ti_5O_9 , and Ti_6O_{11}).

This study confirms the results of previous workers on these materials in that reduction products of ilmenite (particularly rutile) are common. However, our data indicate that these assemblages are not nearly as reduced as previously thought. Fewer than 1/2 of the analyzed rutiles contain magneli phases, and in those cases where the magneli phases occur, they constitute only a small volume fraction of the host rutile (typically <20%). Although these reaction textures have been described previously as the products of "subsolidus" reduction, we believe that the textures represent successive exsolution from a high-T ilmenite solid-solution containing excess Ti (including some Ti^{3+}), Fe, and Cr. On cooling, the ilmenite solid-solution exsolved lamellae of chromite and rutile solid-solution (with some Fe and Ti^{3+}). With further cooling, the Ti^{3+} was concentrated into the magneli phase exsolutions in rutile, while the Fe was incorporated in the second-generation ilmenite lamellae in rutile. The point we are trying to make is that the basaltic magma already contained some Ti^{3+} prior to crystallization (i.e. that the parent liquids were reduced, thus there is no need to invoke reduction at subsolidus temperatures). The main objection to the subsolidus reduction hypothesis is chemical; how can you reduce Ti^{4+} to Ti^{3+} in the rutile lamellae, but not reduce the Fe in coexisting ilmenite lamellae in the same rutile grain? Secondly, because it is easier to reduce Cr^{3+} to Cr^{2+} than it is to reduce Ti^{4+} to Ti^{3+} , it is difficult to understand how chromite and magneli phase exsolutions can coexist in the same ilmenite grain.

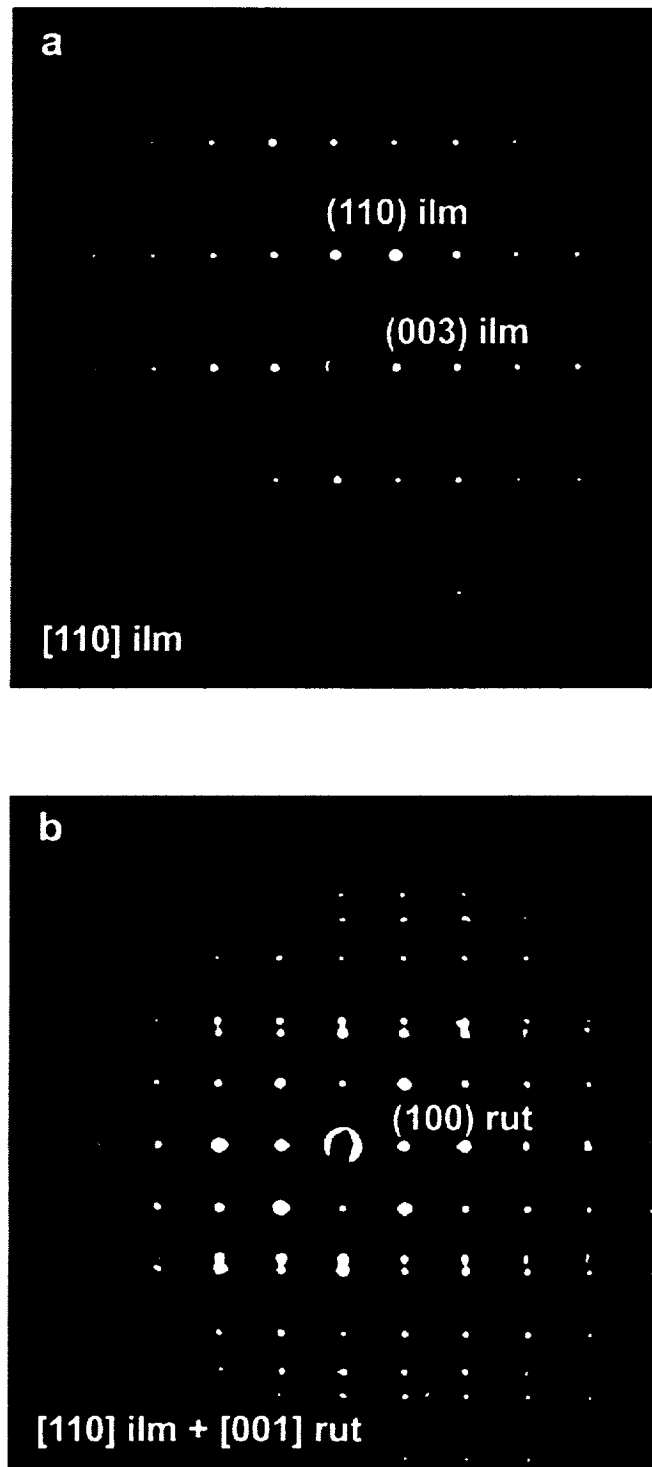


FIGURE 37. a) Selected-area electron-diffraction (SAED) pattern from the $[110]$ zone axis of ilmenite. b) SAED pattern from the $[001]$ zone axis of rutile superimposed on the $[110]$ zone axis of ilmenite (compare to a above). This is the typical orientational relationship between rutile lamellae and their ilmenite hosts in opaque assemblages in Apollo 17 basalt 70035.

ORIGINAL PAGE IS
OF POOR QUALITY

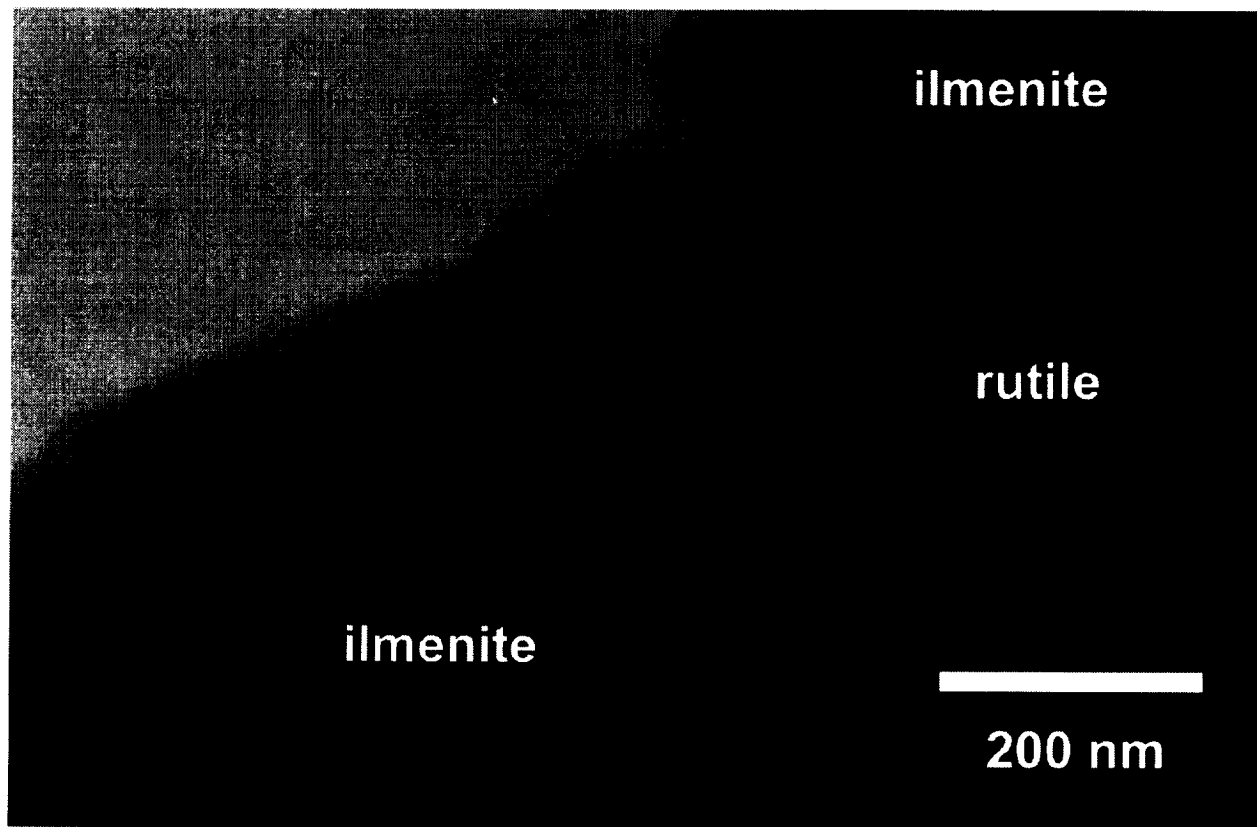


FIGURE 38. A low-magnification bright-field TEM image of a Type I rutile exsolution in ilmenite from 70035. The orientation relationship is the same as illustrated in Figure 37b.

ORIGINAL PAGE IS
OF POOR QUALITY

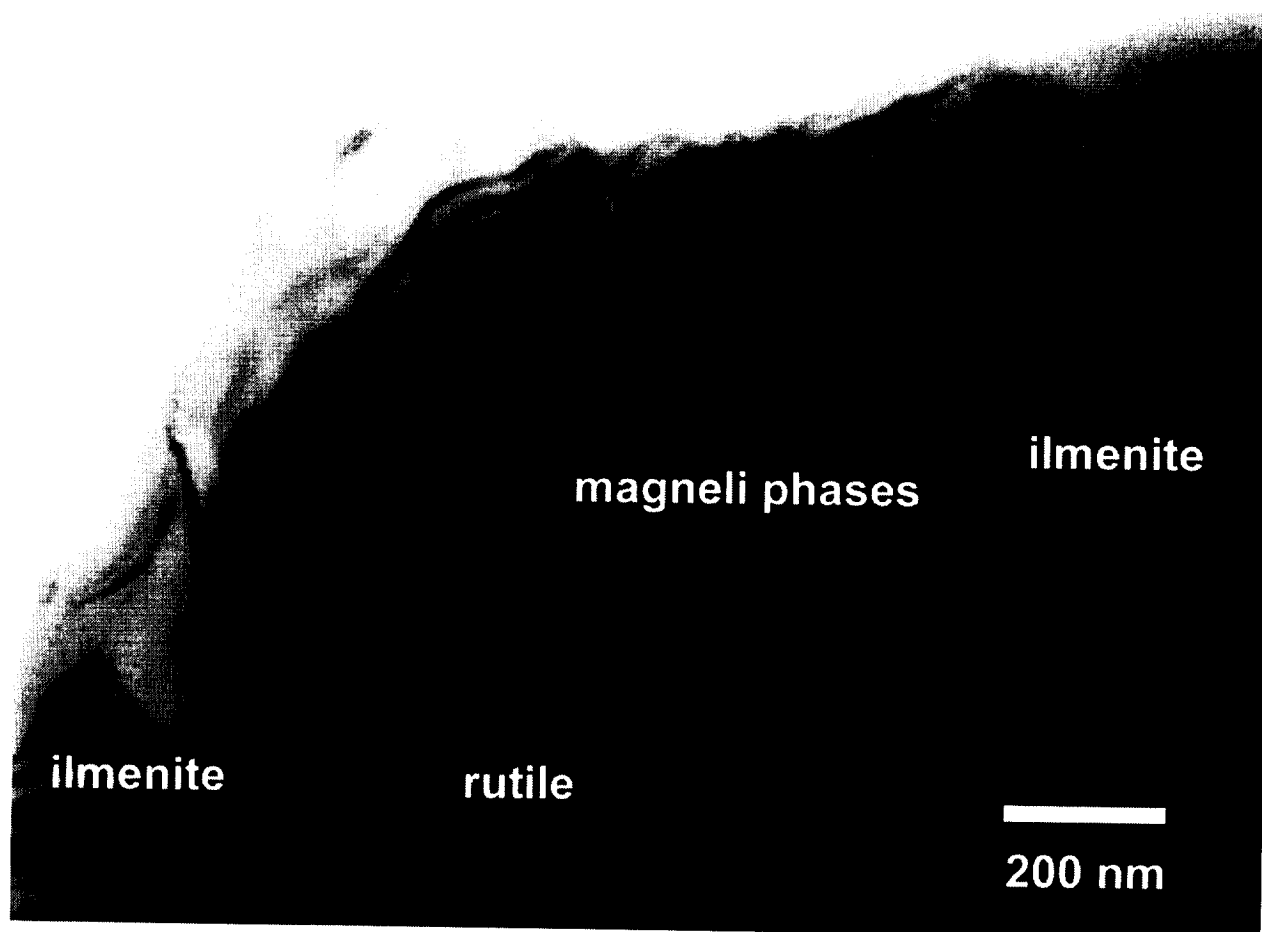


FIGURE 39. A low magnification bright-field TEM image of a Type II rutile exsolution in ilmenite from 70035. Two sets of magneli phase exsolutions within the rutile are indicated. The reticular pattern in within the rutile lamella results from stacking faults.

ORIGINAL PAGE IS
OF POOR QUALITY

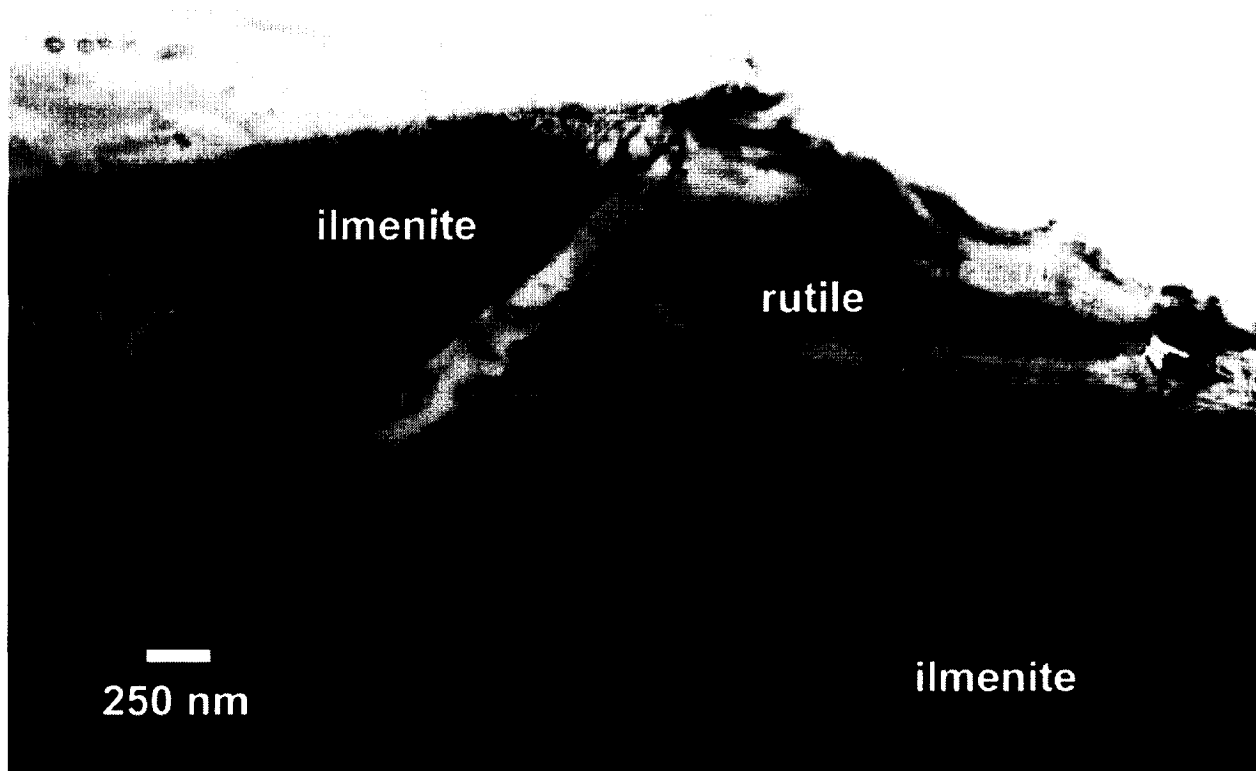


FIGURE 40. A low magnification bright-field TEM image of a Type III rutile exsolution in ilmenite from 70035. Two lamellae of second-generation ilmenite are indicated within the rutile. The rutile is highly strained and contains thin exsolutions of magneli phases.

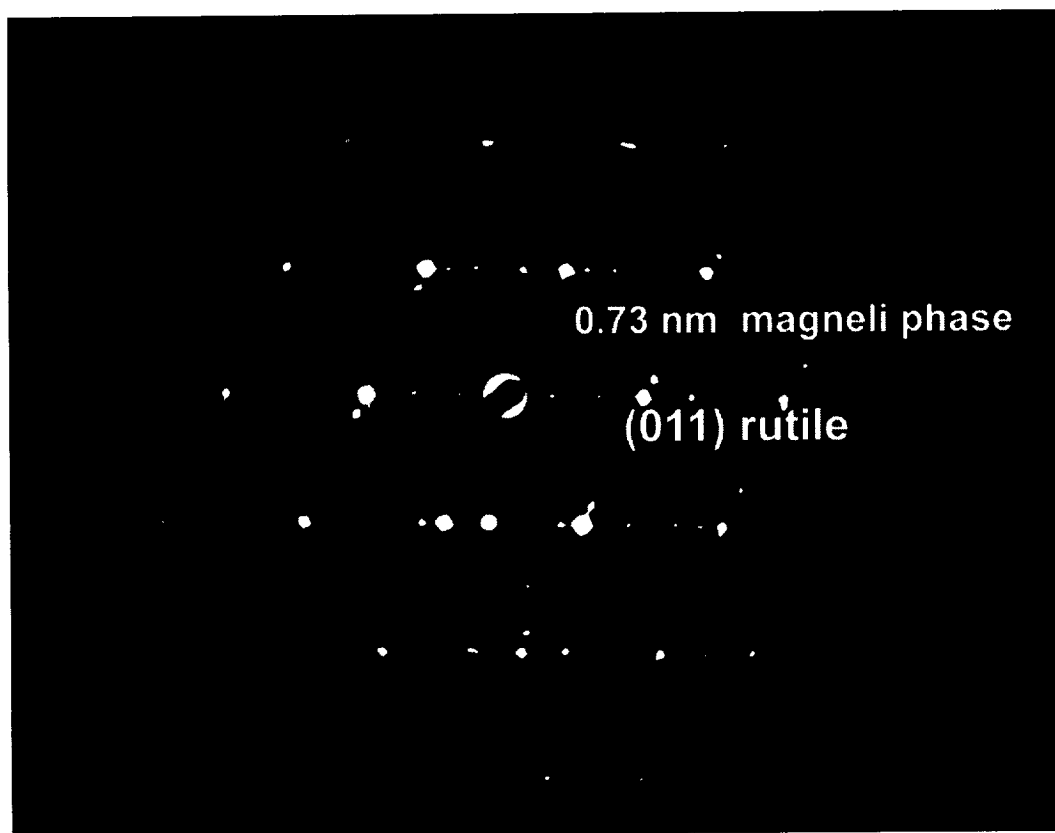


FIGURE 41. Selected-area electron diffraction pattern from the Type II rutile lamella in Figure 39 showing the strong diffraction spots for the rutile host (the (011) reflection for rutile is labelled), and additional spots with a 0.73 nm periodicity that are generated by the exsolved magneli phase. The orientation relationship is such that the (011) of rutile is parallel to the c -axis of the magneli phase.

4.2.c. Analyzing blue rutiles in lunar basalt 70035.

We used the technique of electron energy-loss spectroscopy (EELS) to characterize the nature of "blue rutiles" in high-Ti lunar basalts (70035). We have obtained high resolution EELS spectra from 10 rutile grains from the 70035 sample, along with reference spectra from the TiO_2 polymorphs, and some reduced Ti-oxides. These spectra are collected in Figures 42-44. We conclude that none of the EELS spectra show evidence for appreciable reduced titanium ($>20\% \text{ Ti}^{+3}$). The near edge structure in the titanium L_{2,3} edge and in the oxygen K-edge from all the lamellae are in excellent agreement with the reference spectrum for rutile.

4.2.d. Analysis of reaction rims on armalcolites in 70017 and 70035.

We do not report any analyses of reaction rims on armalcolites in the high-Ti basalts 70017 and 70035, because no rimmed armalcolite grains were present in the petrographic thin sections provided by NASA, that were available for this study.

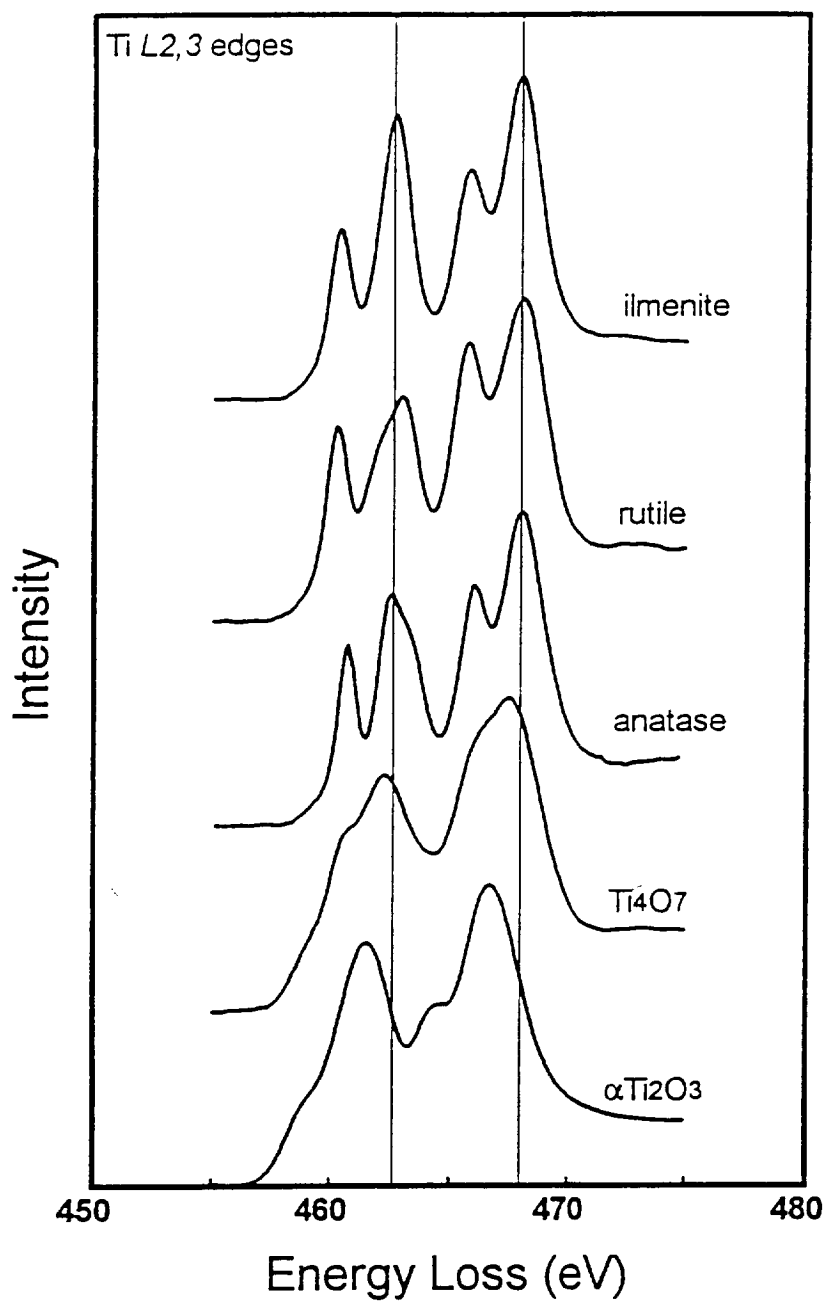


FIGURE 42. EELS spectra from titanium oxide standards showing the near-edge structure in the Ti L_{2,3} edge. The near-edge structure changes and there is a chemical shift of the edge towards lower energy with increasing Ti³⁺ content.

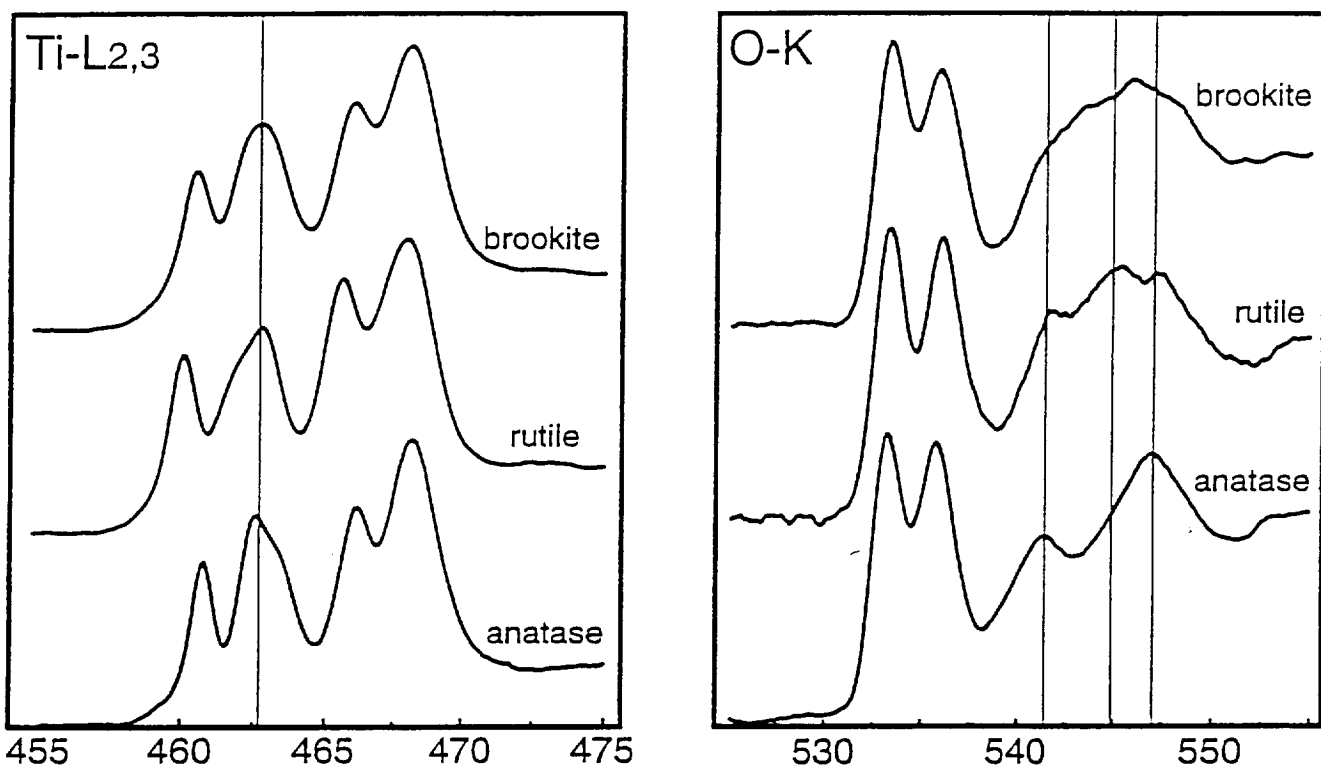
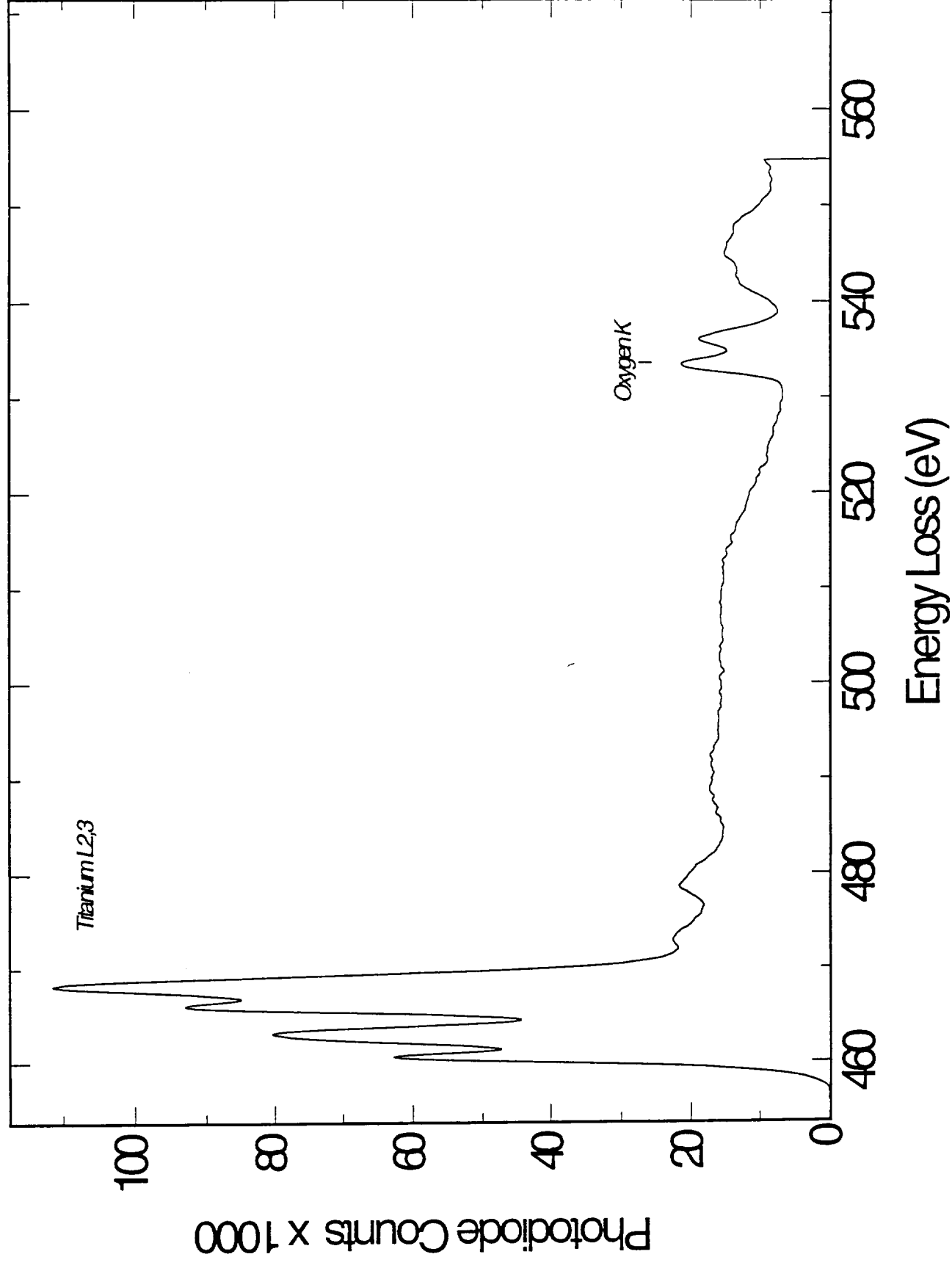


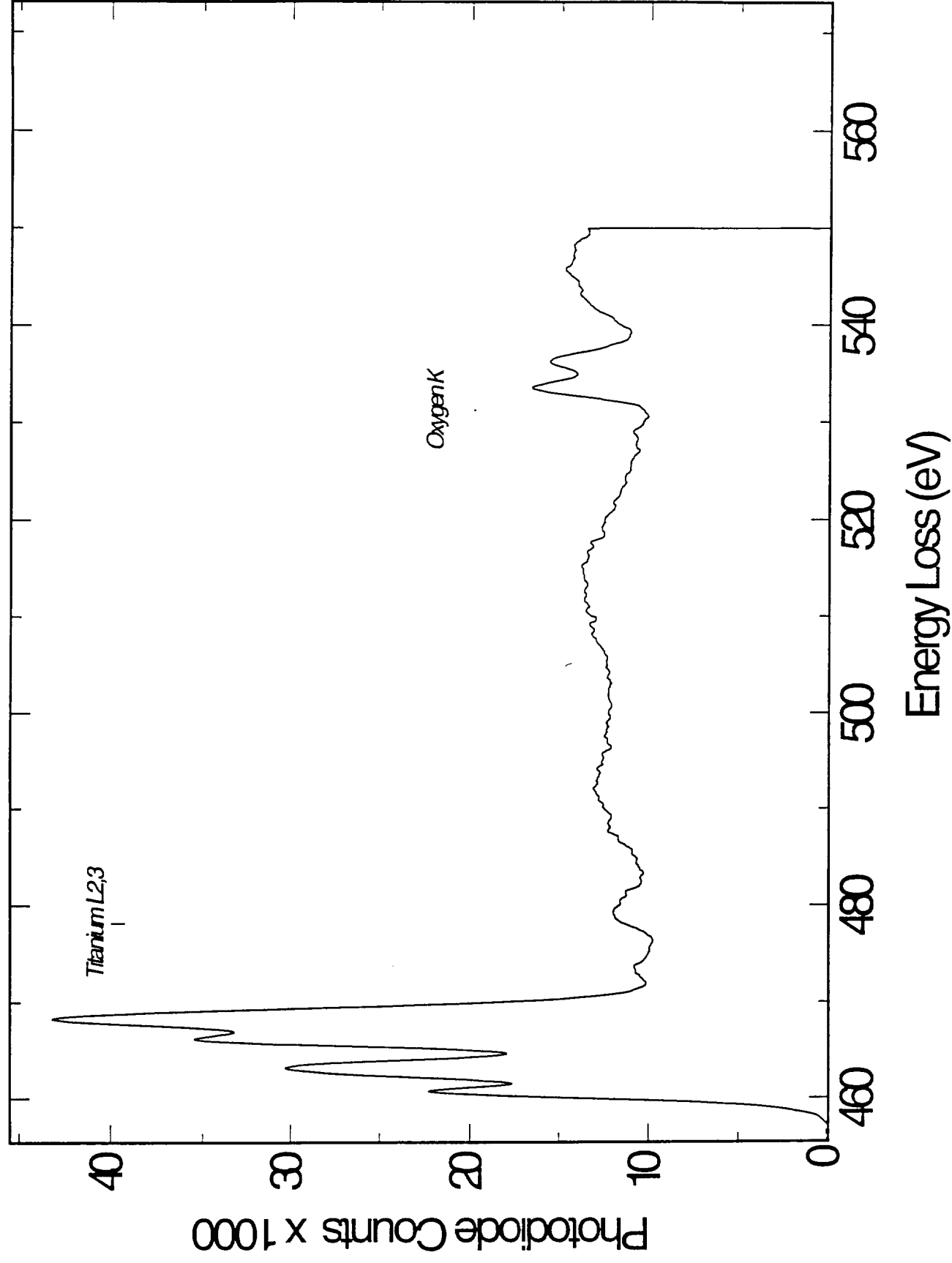
FIGURE 43. EELS spectra from the titanium dioxide polymorphs showing the near-edge structure in the Ti L2,3 edge and in the oxygen k-edge. EELS spectra from the “blue”rutiles in 70035 most strongly resemble the spectra for rutile.

FIGURE 44a-j. EELS spectra from 10 "blue" rutiles in ilmenite from 70035 showing the Ti L_{2,3} edge (beginning at ~455 eV) and the oxygen k-edge (at ~532 eV).

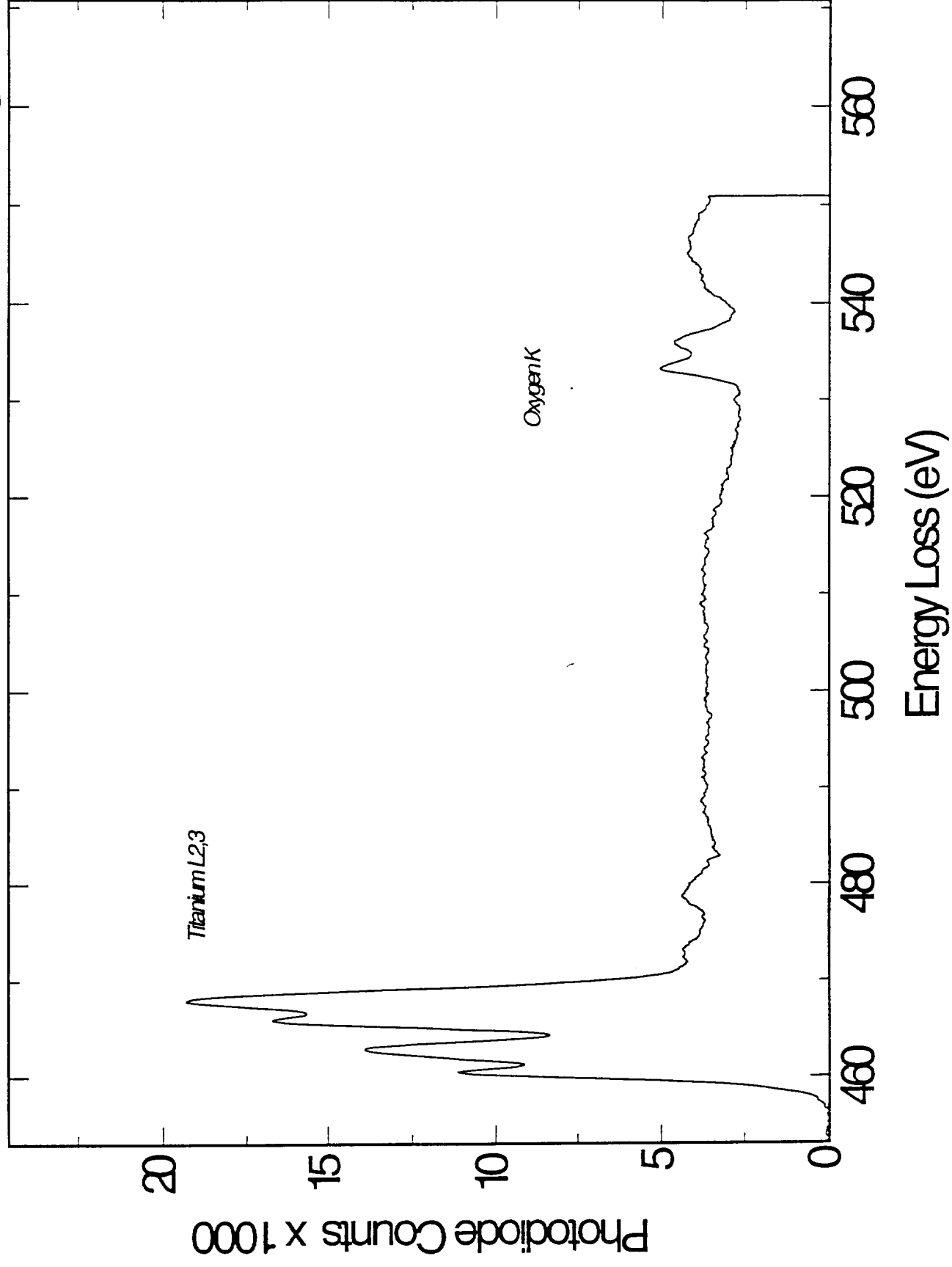
RUTILE-LAM.77035.1.ZLPdecon.smo



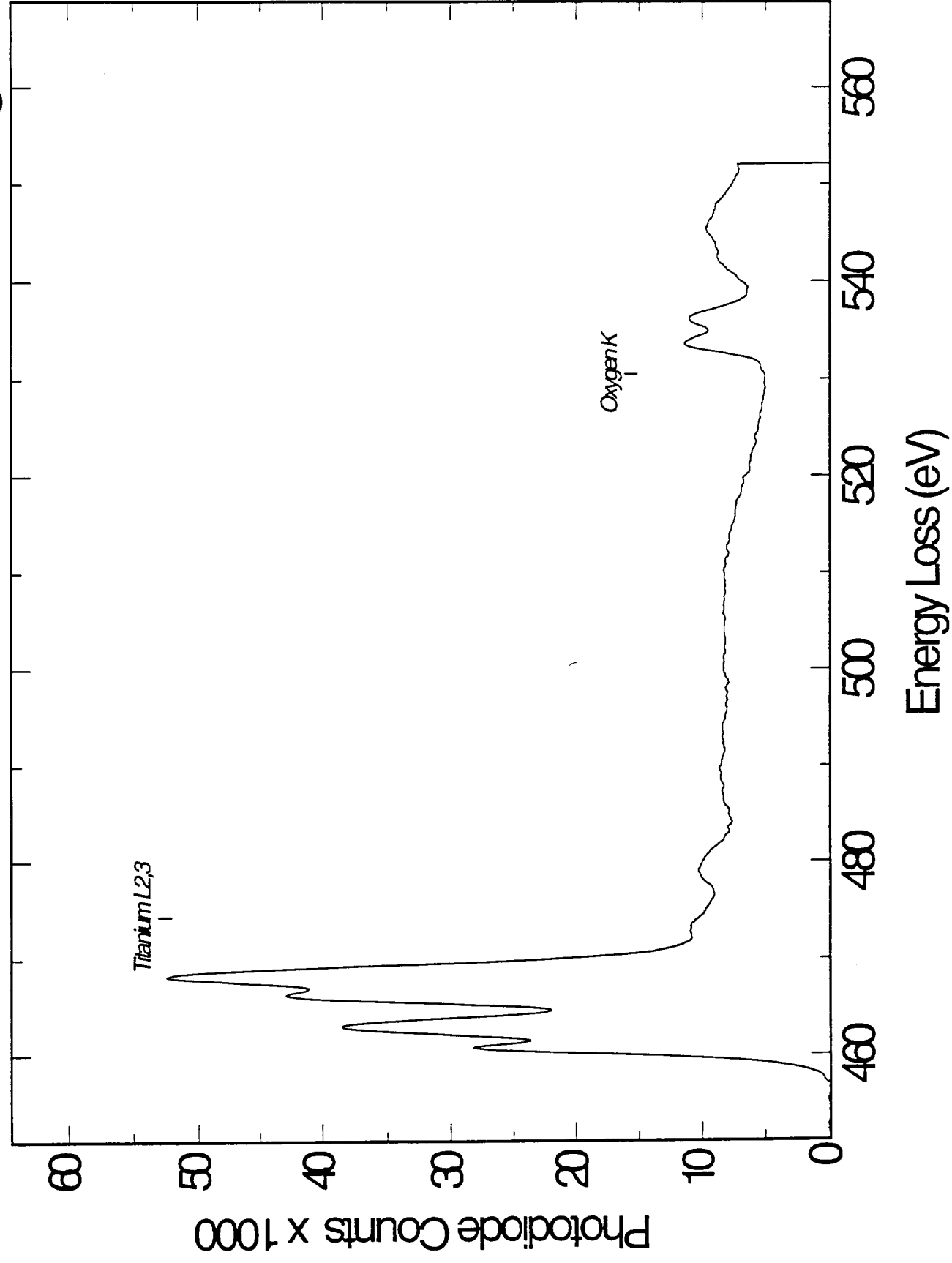
RUTILE-LAM.77035.2.ZLPdecon.smo



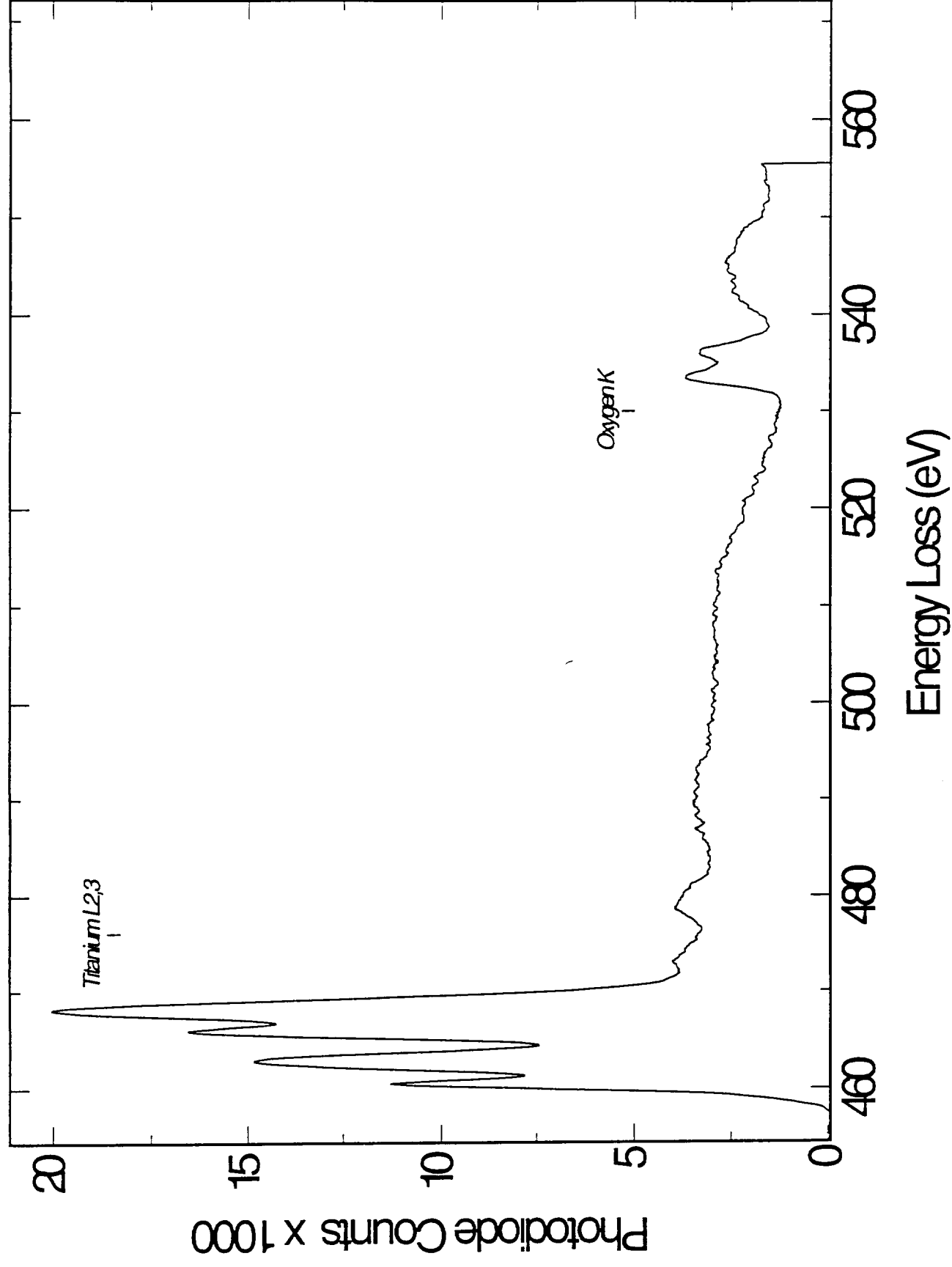
RUTILE-LAM.77035.3.ZLPdecon.smooth.sansBkgd



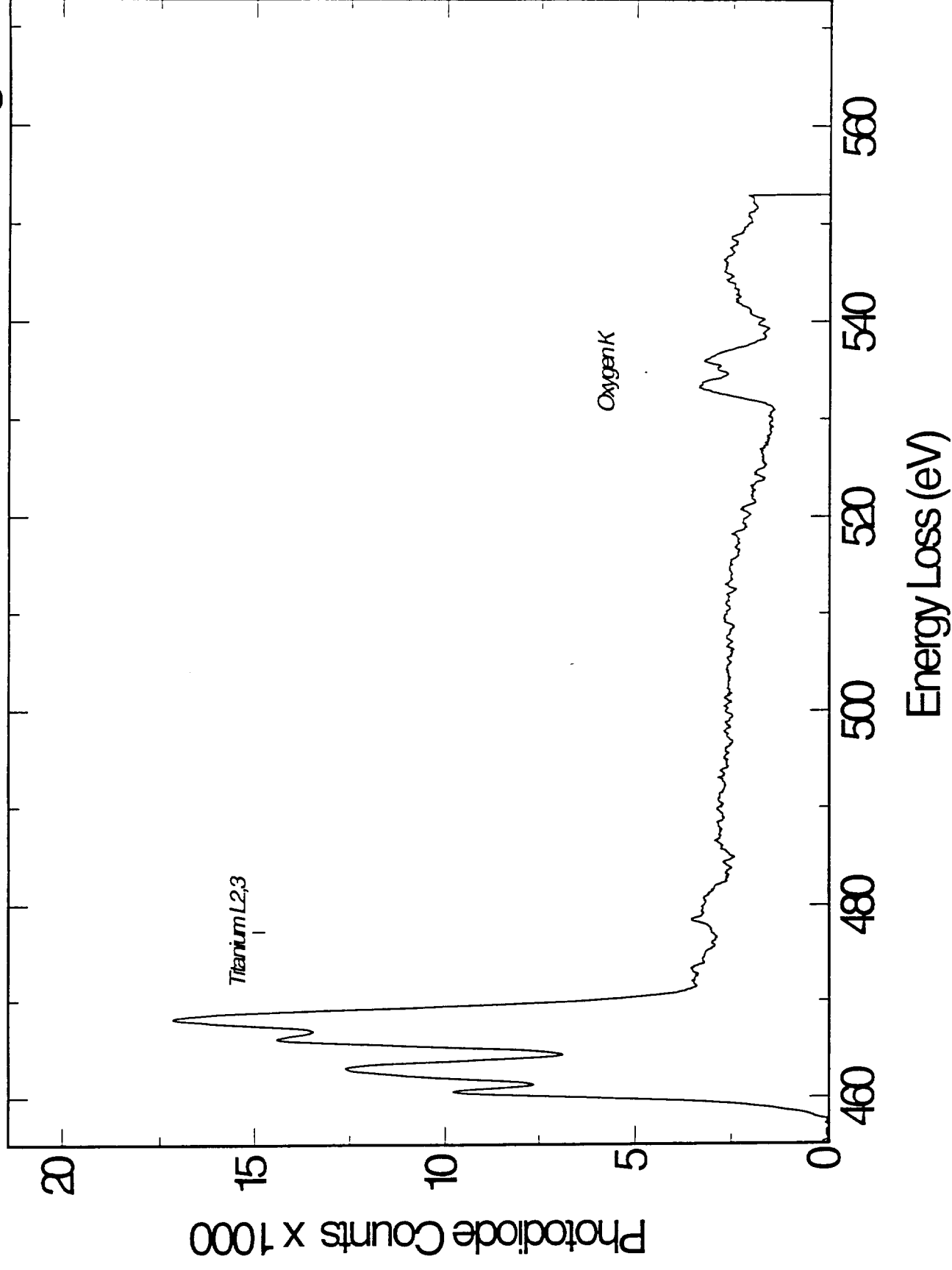
RUTILE-LAM.77035.4.ZLPdecon.smooth.sansBkgd



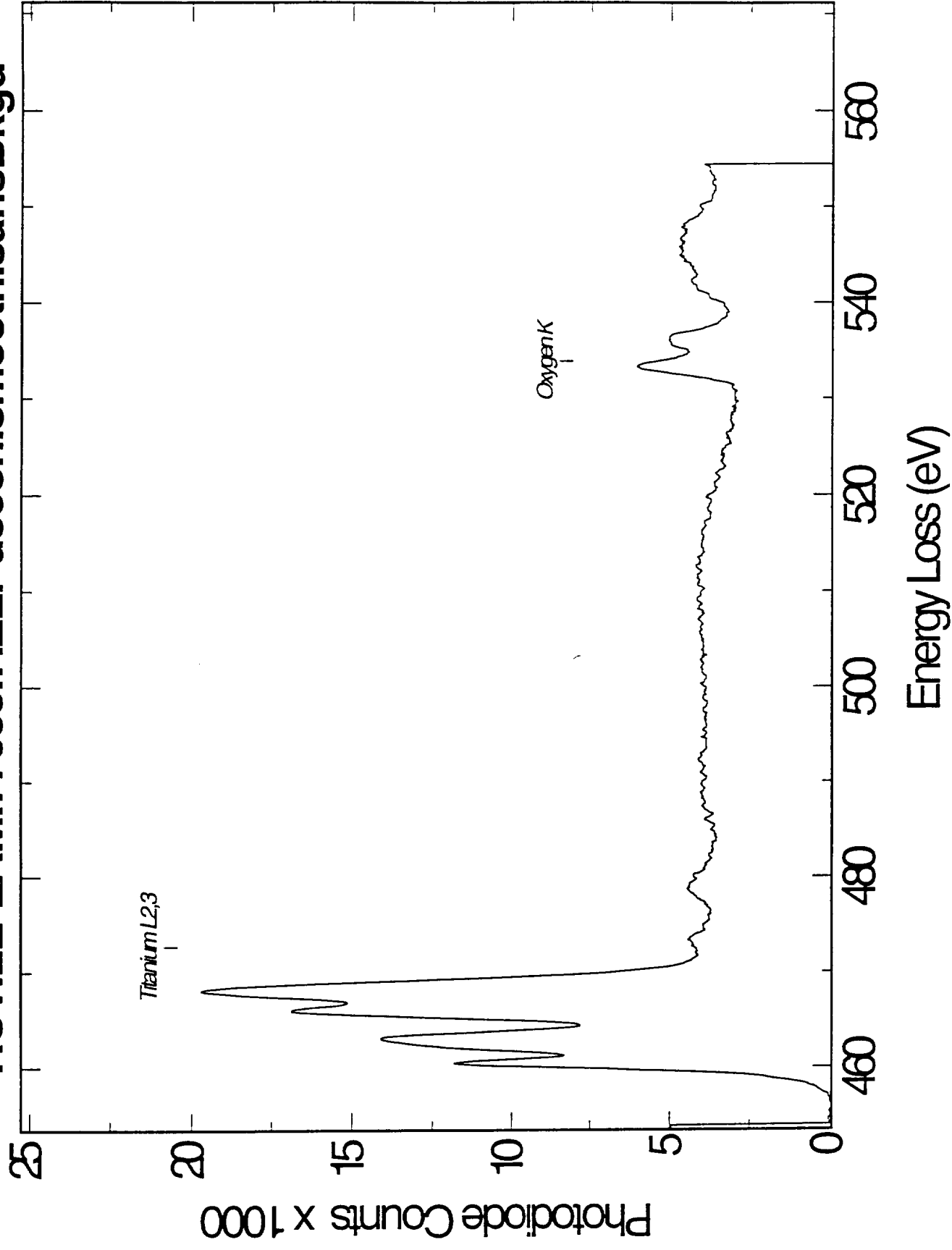
RUTILE-LAM.77035.5.ZLPdecon.smo



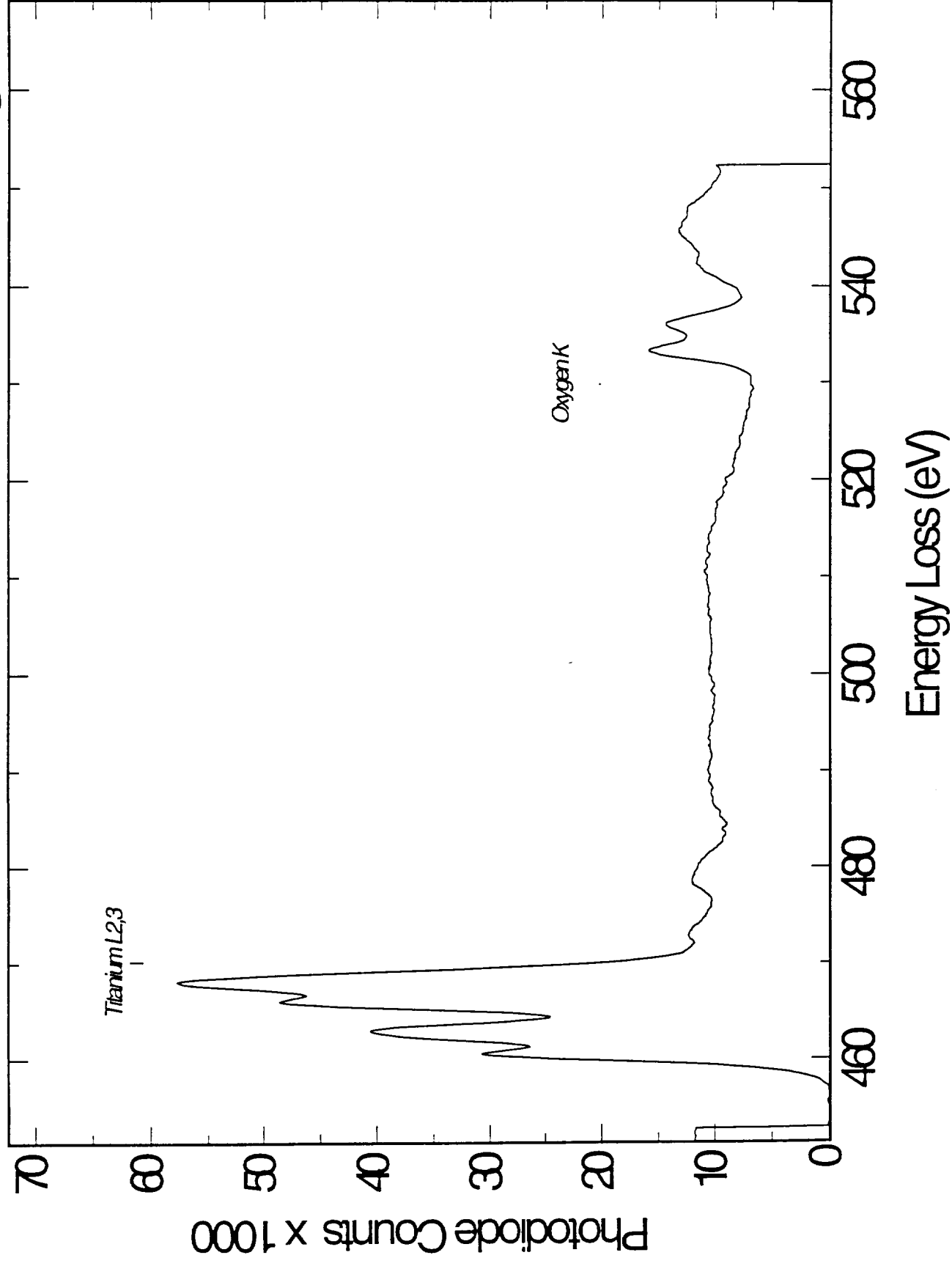
RUTILE-LAM.77035.6.ZLPdecon.smooth.sansBkgd



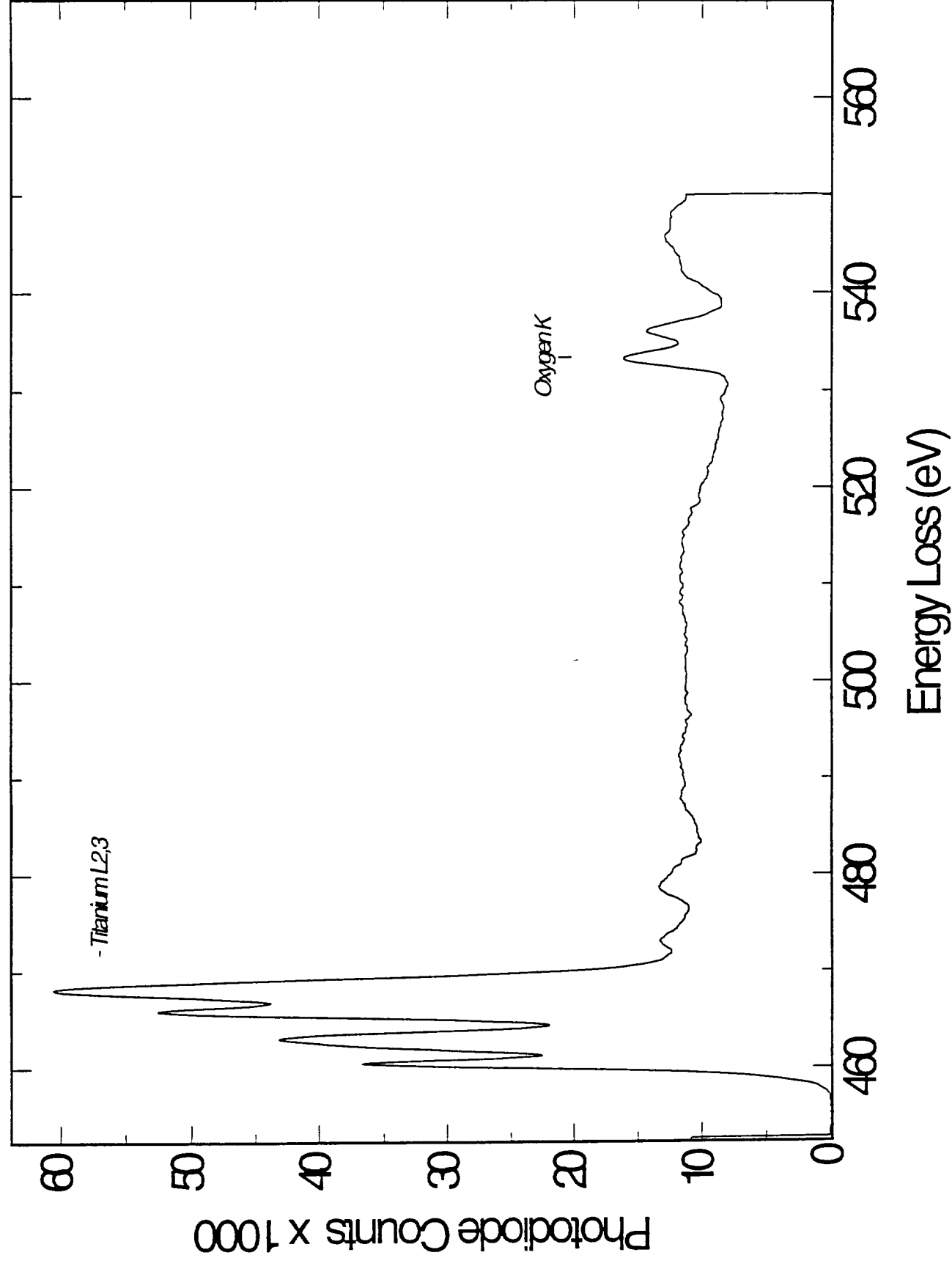
RUTILE-LAM.77035.7.ZLPdecon.smooth.sansBkgd



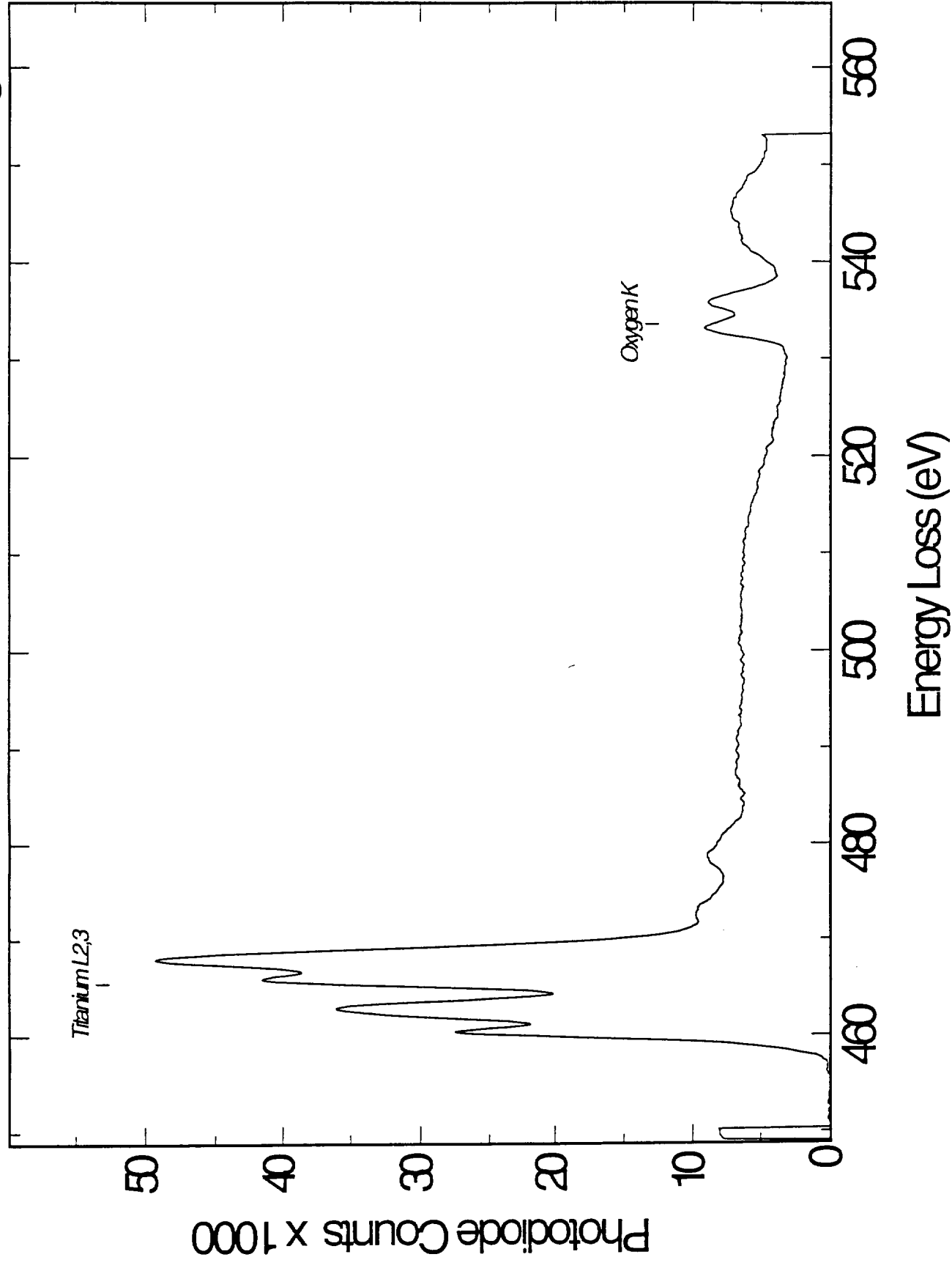
RUTILE-LAM.77035.8.ZLPdecon.smooth.sansBkgd



RUTILE-LAM.77035.9.ZLPdecon.smo



RUTILR-LAM.77035.10.ZLPdecon.smooth.sansBkgd



4.2.e. Reduction microstructures in lunar soil grains.

Here we report on our studies of reduction microstructures in lunar soil grains with emphasis on soil ilmenite grains from 10084, and “vesicular rims” on silicates in the immature soil 61221.

Ilmenite. Ilmenite grains in lunar soils are commonly surrounded by complex rim sequences that result from their exposure to the lunar “weathering” environment [e.g. Christoffersen *et al.*, (1994) LPSC XXV, 259]. These rims consist of an outer, thin amorphous rind of vapor-deposited silicate material, and a relatively thick, inner layer that is depleted in Fe relative to stoichiometric ilmenite. TEM studies have shown that the inner rim is not amorphous, but consists of a microcrystalline assemblage of ilmenite containing platy precipitates of rutile and probable Fe metal grains. In this study, electron energy-loss spectroscopy (EELS) was used to demonstrate that the altered rims on soil ilmenites contain significant trivalent titanium. Our data indicate that the disordered rims are chemically “reduced” and that oxygen has been lost from the rims. These results have implications regarding the processes responsible for the formation of disordered rims on ilmenite as well as their potential effects on the optical properties of lunar soils and are summarized in an abstract submitted to the XXVI Lunar and Planetary Science Conference (attached in Appendix-Publications).

Aliquots of a <20 μm sieve fractions of 10084 and individual ilmenite grains from the same soil were embedded in low viscosity epoxy, and TEM specimens were prepared by ultramicrotomy. The thin sections were analyzed using a JEOL 2010 (200kV) transmission electron microscope equipped with a LaB₆ filament, a thin-window energy-dispersive x-ray detector, and a GATAN 666 parallel EEL spectrometer. EELS spectra were collected in TEM image-mode at 15KX magnification with a collection semi-angle of ~ 100 milliradians at a dispersion of 0.1 eV/channel. The FWHM of the raw (unprocessed) zero-loss peak was ~ 0.7 eV. The relative energy of features in the spectra for the Ti L_{2,3} edges were calibrated relative to the C π^* peak maximum, which was set to 286 eV. For the Ti L_{2,3} spectra, the characteristic edge structure results from the promotion of inner shell (2p) electrons to valence and conduction bands (3d states). The EELS data provide information on the local solid state environment, including oxidation states. Differences in oxidation state are manifested by “chemical” shifts in energy of the edge onset and by changes in the near-edge structure.

EELS spectra of the Ti L_{2,3} edge have been obtained from 5 (<20 μm in dia.) individual ilmenite grains from the Apollo 11 soil 10084, and all spectra show significant differences between the altered rims and the core ilmenite. EELS data from the core of a lunar ilmenite grain, the disordered rim on the ilmenite, and synthetic Ti-oxides with well-constrained Ti³⁺/Ti⁴⁺ ratios are shown in Figure 45. Figure 46 shows Ti-EELS spectra for 4 additional ilmenite grains from 10084. The spectra from the altered rims exhibit a chemical shift of

~0.5 eV towards lower energy relative to the position of the Ti L_{2,3} edge in the core of the ilmenite grains. In addition, the splitting of the L₃ and L₂ peaks is reduced in spectra from the disordered rims as compared to the core ilmenite. Both the chemical shift and the change in the near-edge structure are consistent with a Ti³⁺/Ti⁴⁺ ratio of ~0.25 in the disordered rims.

The EELS results indicate that much of the Ti in the disordered rims is trivalent. We also obtained TEM-EDX analyses of rim sequences on two ilmenite grains from 10084 (Table 4) which show significant accumulations of silicate material in the rims (vapor deposits) and that the rims are, in fact, reduced (especially for ilmenite 2, Table 4). Figure 47 illustrates the disordered rim on ilmenite 1.

Vesicular rims on silicate grains in 61221. Many of the soil grains (both glass and mineral fragments) in 61221 are surrounded by what we term "vesicular rims" that are typically ~100 nm wide (Figures 48 and 49). These rims are amorphous and do not contain visible inclusions (e.g. Fe metal grains). Although our current number of analyses (Table 5 contains data from 5 grain-rim pairs) are limited, some chemical systematics are apparent. On average, the rim compositions are little different from the core of the grains. However, the data from the one orthopyroxene grain that was surrounded by a vesicular rim (Table 5) shows that the rim is depleted in certain cations (notably Mg, Ca and Fe) relative to the core and is probably enriched slightly in oxygen; similar chemical trends have been linked to irradiation effects from the solar wind (see Bradley, *Science*, vol. 265, p. 925). Our current hypothesis is that these vesicular rims are related to the implantation of solar wind gases, either forming during the implantation, or by subsequent heating of the soil grains (heating from a nearby impact?). It is intriguing that we have only observed these vesicular rims in an immature soil.

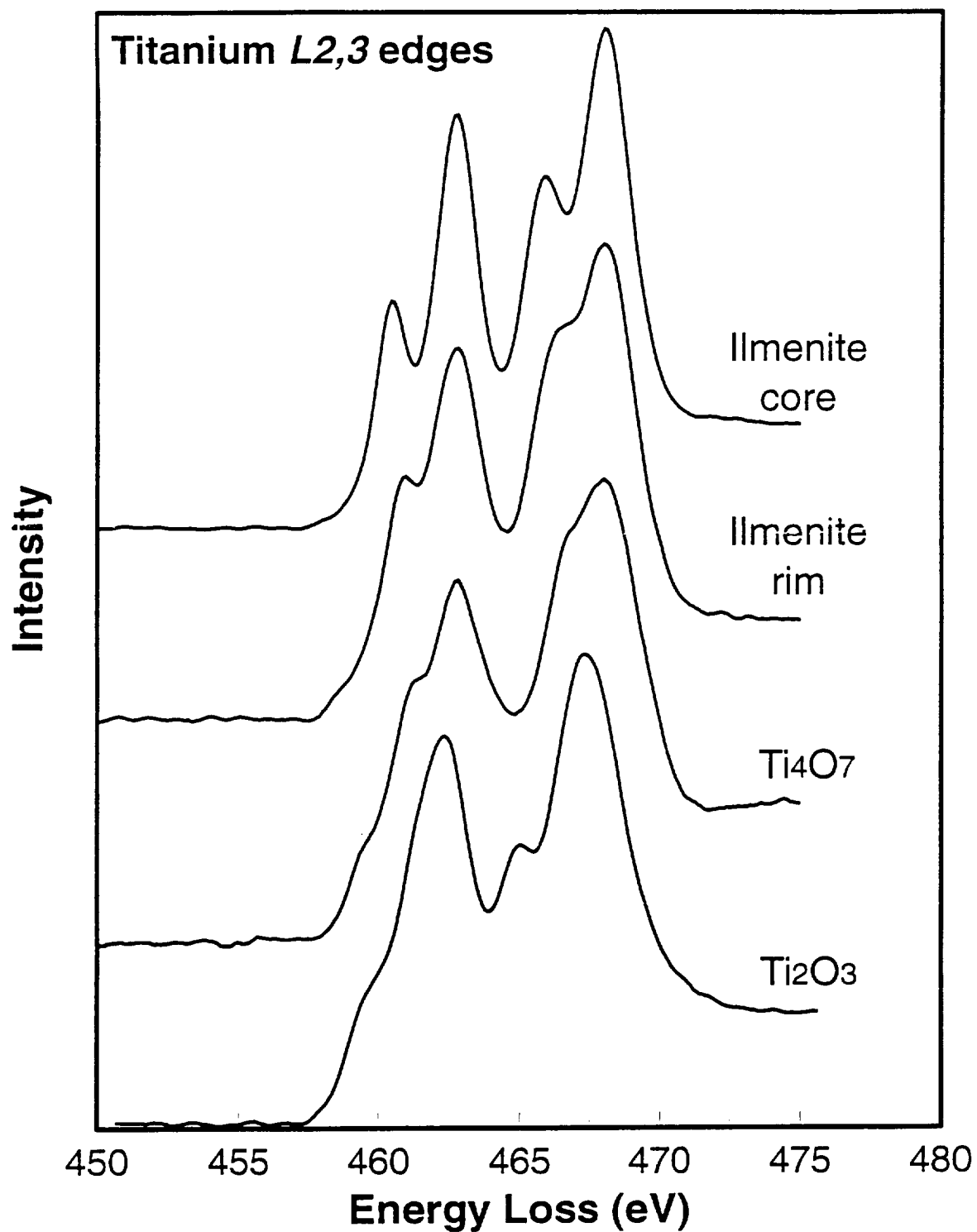


FIGURE 45. Electron energy-loss spectra for the Ti L_{2,3} edge for a typical ilmenite core/rim pair, along with data for Ti³⁺ bearing oxides. The spectra are shifted vertically for clarity.

Titanium L_{2,3} edges for individual ilmenite grains from 10084.

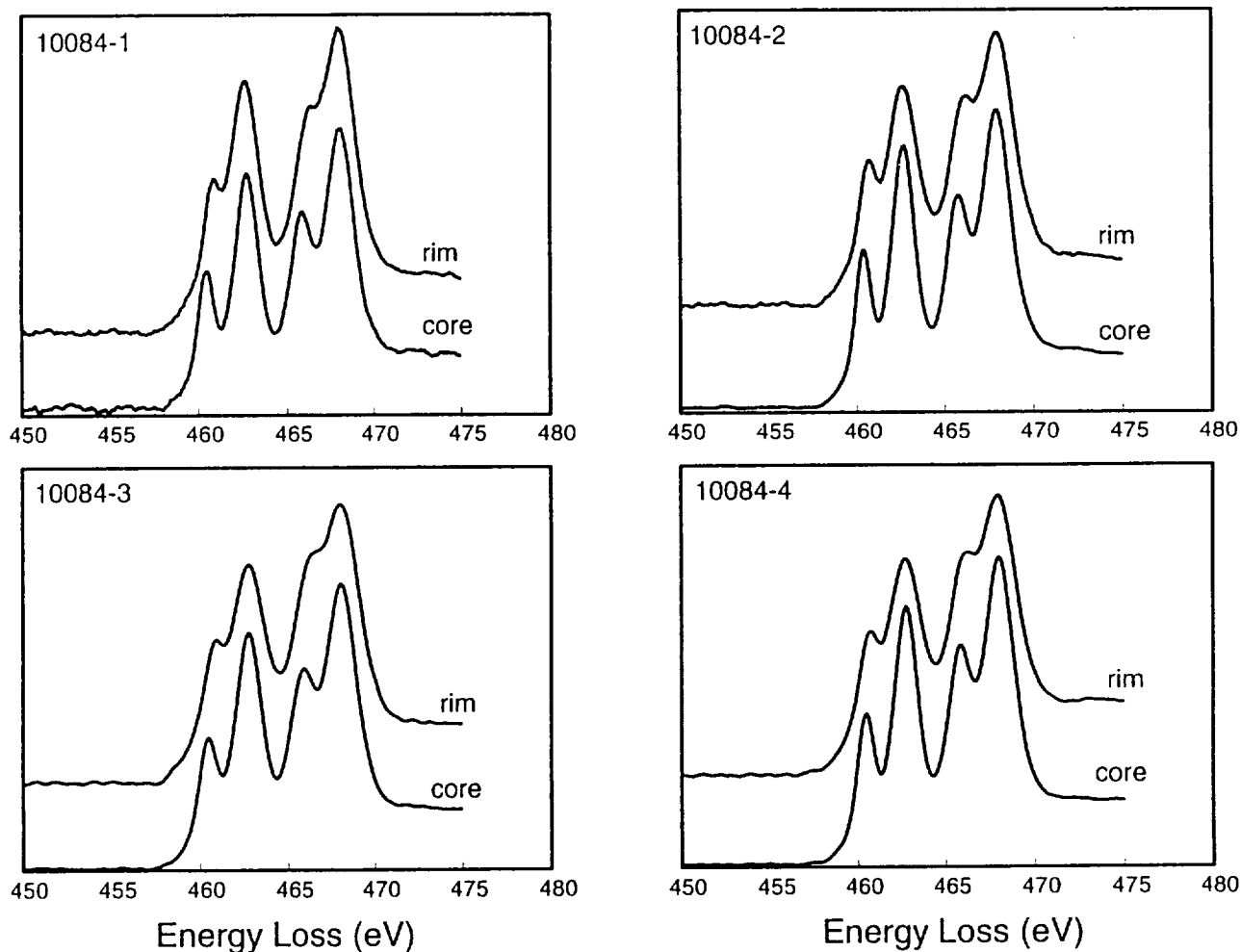


FIGURE 46. Electron energy-loss spectra for the Ti L_{2,3} edge for 4 additional ilmenite core/rim pairs.

TABLE 4. TEM-EDX analyses of two ilmenite grains (1 and 2) with disordered rims. Analyses 74-76 are for grain 1 while analyses 57-61 are for grain 2. These analyses were obtained with a 20 nm beam and represent a traverse from the outer edge of the grain into the interior. Analyses are in atom %.

	Ilmenite 1			Ilmenite 2				
	74 outer rim	75 inner rim	76 core	57 outer rim	58	59	60 inner rim	61 core
Atom %								
O	59.30	60.28	61.14	56.20	61.83	61.26	62.86	65.06
Mg	0.79	0.81	1.23	1.46	1.59	0.39	0.76	0.79
Al	0.34	0.00	0.00	1.72	0.34	0.00	0.00	0.01
Si	4.51	1.31	0.04	14.26	2.03	0.37	0.35	0.56
S	0.36	0.06	0.00	0.33	0.21	0.00	0.18	0.04
Ca	0.32	0.00	0.00	0.92	0.14	0.00	0.00	0.00
Ti	25.96	25.57	19.56	17.30	30.33	22.47	18.89	16.91
Cr	0.43	0.38	0.32	0.05	0.12	0.10	0.11	0.08
Fe	7.99	11.59	17.70	7.76	3.42	15.40	16.85	16.55

ORIGINAL COPY
OF POOR QUALITY

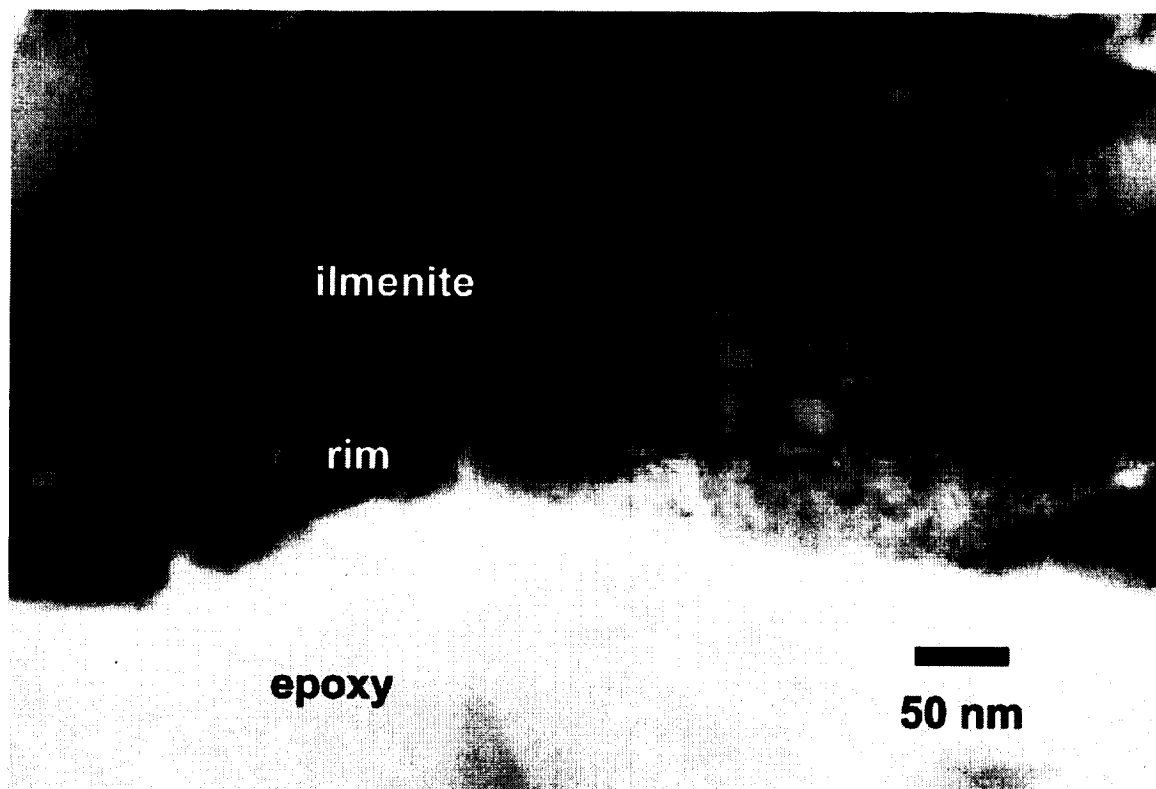


FIGURE 47. Low magnification bright-field TEM image of a disordered rim on an ilmenite grain from soil 10084. Analyses from this rim are given in Table 4 (ilmenite 1).

ORIGINAL PAGE IS
OF POOR QUALITY

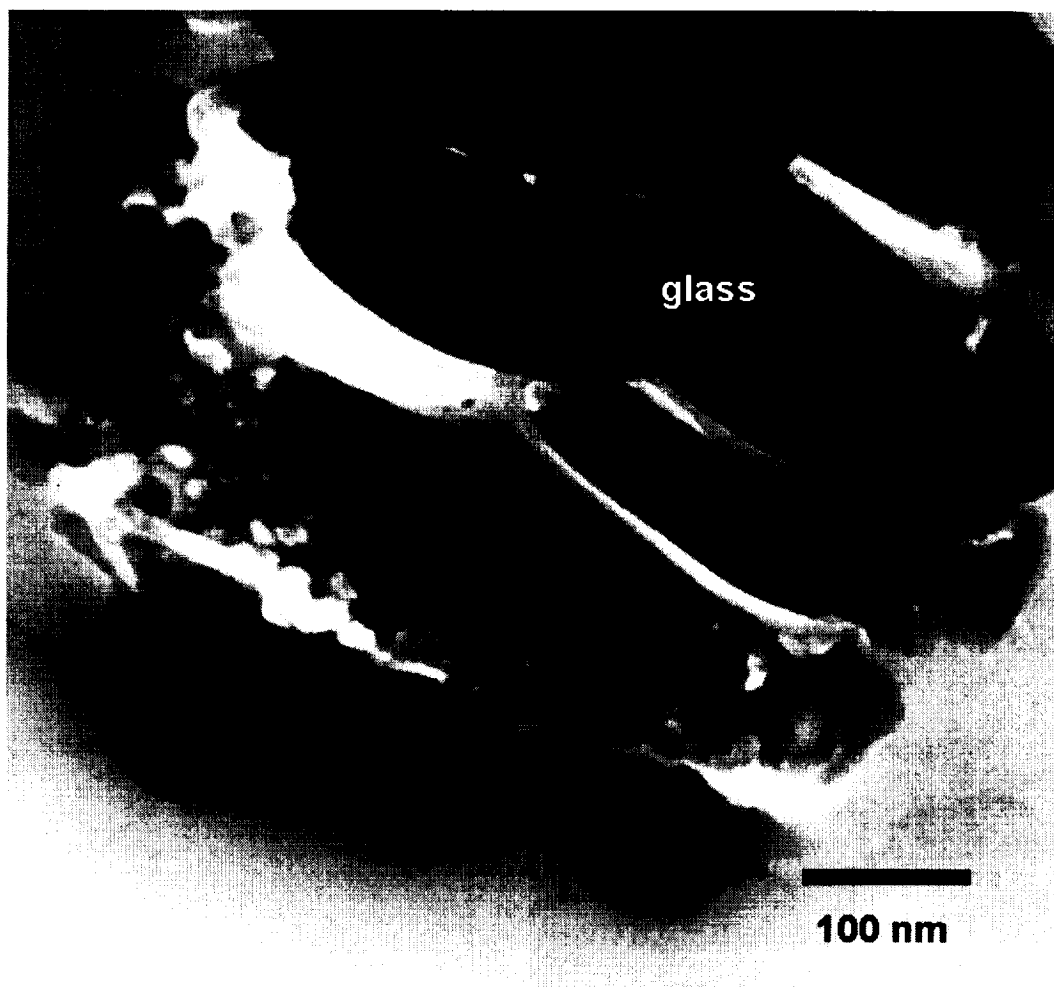


FIGURE 48. Low magnification bright-field TEM image of a vesicular rim on a glass fragment (analyses 42 and 43 in Table 5) in soil 61221.

ORIGINAL PAGE IS
OF POOR QUALITY

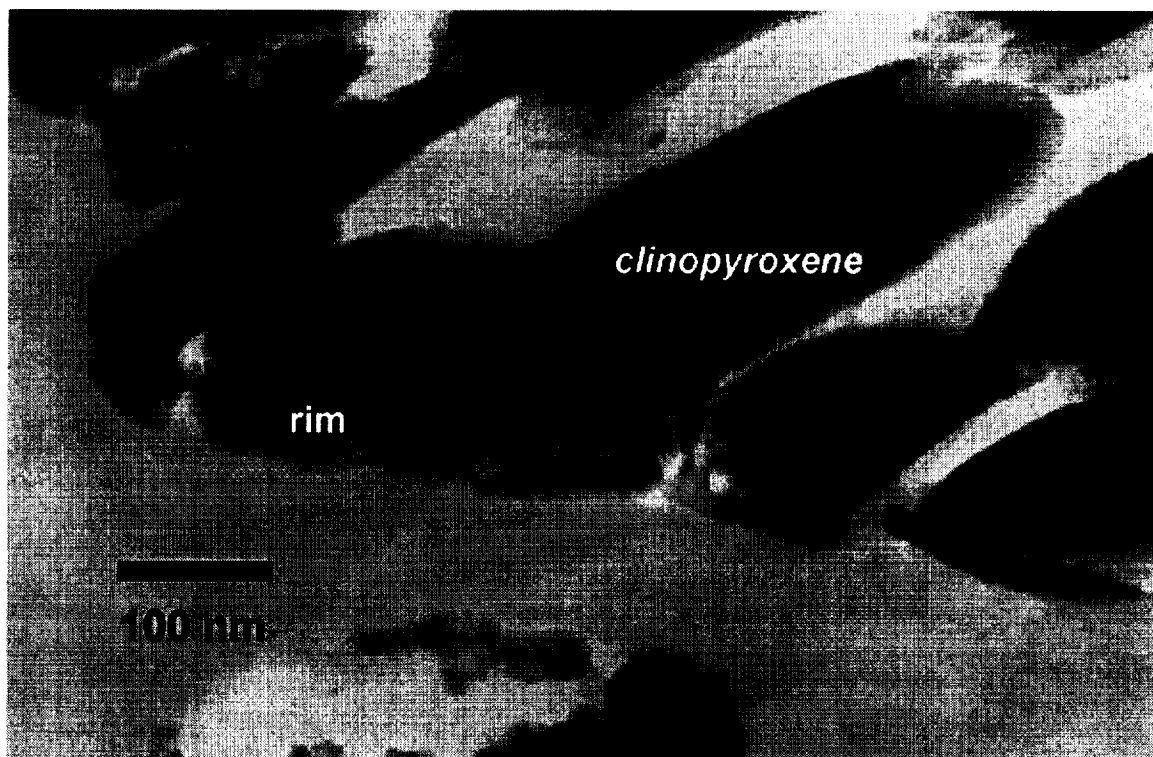


FIGURE 49. Low magnification bright-field TEM image of a vesicular rim on a clinopyroxene grain (analyses 177-179 in Table 5).

TABLE 5. TEM-EDX analyses of vesicular rims on soil grains in 61221.
Analyses are given in atom. %.

Analyses 134-137 are from orthopyroxene.

Analyses 177-179 are from a clinopyroxene, the remaining analyses are from glassy grains.

Analysis (in at. %)	O	Mg	Al	Si	S	Ca	Ti	Fe	Na
177 core	59.14	8.07	0.84	20.89	0.04	7.12	0.19	3.70	0.00
178 inner rim	62.67	5.99	0.73	21.91	0.00	5.34	0.20	3.15	0.00
179 outer rim	66.87	4.20	1.38	21.41	0.02	3.54	0.26	2.31	0.00
134 core 1	55.47	10.46	0.64	22.15	0.01	1.88	0	9.4	0.00
135 rim 1	64.94	9.12	1.05	18.11	0.05	1.71	0.09	4.93	0.00
136 core 2	56.28	12.03	1.13	22.05	0.05	1.13	0.03	7.29	0.00
137 rim 2	65.31	8.42	0.9	19.27	0.05	1.35	0.07	4.63	0.00
42 core	47.69	3.82	17.42	10.13	0	16.23	0.6	4.11	0.00
43 rim	54.71	3.47	15.83	10.28	0	12.2	0.49	3.02	0.00
109 core	60.79	5.05	10.75	16.54	0.03	5.23	0.05	1.16	0.40
108 rim	62.12	2.83	11.43	15.98	0.07	5.54	0	0.82	1.20
113 core	62.31	9.86	4.72	17.56	0.03	3.12	0.09	2.31	0.00
111 rim	62.23	8.88	6.17	16.74	0.09	3.5	0.14	2.26	0.00

4.2.f. Analyzing agglutinates in lunar soils.

We are continuing our studies of the characteristics of agglutinitic glass fragments in fine grained fractions of lunar soils. Our strategy is to analyze 50-100 nm in diameter regions within individual fragments of agglutinitic glass from fine size-fractions of lunar soils in order to evaluate the compositional heterogeneity of the glass at the submicrometer scale. We have analyzed agglutinitic glass in several lunar soils including: 10084, 61181, 61221, and 72501. A total of 97 individual analyses were obtained from multiple regions within 13 individual fragments of agglutinitic glass in Apollo 11 soil 10084 (Table 6). The bulk compositions of the 13 fragments are given in Table 7. Figure 50 shows plots of the individual analyses and the bulk compositions of fragments on plots of $\text{MgO} + \text{FeO}$ versus $\text{Al}_2\text{O}_3 + \text{CaO}$. We found that agglutinitic glass shows compositional and textural heterogeneities at the $0.1\ \mu\text{m}$ scale and that the fragments preserve a component of vapor deposited material. It was shown that the number density of Fe inclusions in agglutinitic glass was highly variable, but in general the size distributions tend to be similar and follow a log-normal distribution. We have also demonstrated that the actual size range of Fe grains in agglutinitic glass is similar to that estimated by Ferromagnetic Resonance. These data were presented at the 25th Lunar and Planetary Science Conference. An abstract summarizing these results is attached in the Appendix (Keller and McKay, 1994, LPSC XXV, 685).

We observed several interesting trends in the nature of agglutinitic glass in 61221 (an immature soil). Agglutinitic glass in 61221 shows a wide range in composition from fragment to fragment (Figure 51), although the average of all fragments is remarkably close to the bulk soil composition (comparison at bottom of Table 8). This wide range in composition is similar to that exhibited by other lunar soils including mature highlands soils (e.g. 72501 and 61181). Most fragments in 61221, however, lack the abundant vesicles and submicroscopic Fe metal grains that are also common in agglutinitic glass from mature soils.

We have completed the chemical analyses of fragments in the $<20\ \mu\text{m}$ fractions of 61181 and 72501. Figures 52 and 53 show the data for the fragment averages and the individual analyses on plots of $\text{MgO} + \text{FeO}$ versus $\text{Al}_2\text{O}_3 + \text{CaO}$, and on plots of MgO versus FeO . The former plots show the well known negative correlation between the felsic and mafic components of agglutinitic glass, while the latter plots show a strong positive correlation between Mg and Fe. The individual analyses and the fragment bulk compositions are given in Tables 9-12.

TABLE 6. Individual TEM-EDX analyses of ~100 nm regions in fragments of agglutinitic glass from soil 10084. Data are presented in oxide wt.% and include data for fragments A to H.

EDX Analyses of Agglutinitic Glass Fragments (A to N) - Soil 10084

(wt. %)	MgO	Al ₂ O ₃	SiO ₂	SO ₃	CaO	TiO ₂	Cr ₂ O ₃	MnO	FeO
A1	8.78	13.84	42.43	2.07	11.94	6.87	0.27	0.27	13.52
A2	6.25	20.85	44.87	0.39	13.34	4.78	0.21	0.01	9.26
A3	0.00	30.29	54.95	0.06	14.37	0.15	0.00	0.00	0.59
A4	2.84	28.11	47.73	0.61	15.41	0.31	0.16	0.02	4.80
A5	5.49	20.27	46.82	0.84	11.97	4.64	0.22	0.10	9.65
A6	7.37	14.83	42.62	2.48	11.23	7.22	0.32	0.29	13.63
B1	9.23	20.02	33.25	0.14	15.50	7.80	0.16	0.31	13.59
B2	10.92	8.55	45.27	0.52	10.79	6.06	0.53	0.35	17.03
B3	9.72	9.83	46.52	0.34	10.51	6.23	0.56	0.27	16.02
B4	9.00	9.17	48.27	0.17	10.00	6.12	0.64	0.24	16.39
B5	10.67	7.90	50.55	0.19	8.29	6.02	0.59	0.38	15.42
C1	4.76	20.50	43.65	0.45	12.51	7.37	0.15	0.08	10.52
C2	6.64	22.29	50.98	0.27	13.78	0.18	0.00	0.05	5.86
C3	6.63	16.85	46.26	0.31	12.49	6.30	0.10	0.29	10.77
C4	4.97	26.08	42.35	0.36	16.17	2.80	0.13	0.07	7.06
C5	4.45	20.67	41.90	0.47	12.81	8.03	0.15	0.16	11.35
C6	6.04	18.17	44.48	0.27	12.83	6.25	0.20	0.26	11.49
D1	10.04	11.44	43.89	0.23	13.64	6.40	0.34	0.22	13.80
D2	7.55	16.79	42.55	0.24	12.40	7.02	0.44	0.12	12.89
D3	8.28	16.66	40.94	0.15	12.76	7.64	0.40	0.15	13.02
D4	8.52	14.40	44.73	0.43	12.14	5.76	0.23	0.19	13.61
D5	8.44	14.98	41.99	0.35	12.71	7.79	0.29	0.26	13.18
D6	9.26	13.69	41.03	0.48	12.03	9.13	0.28	0.17	13.93
E1	6.56	17.43	43.48	0.55	13.77	6.56	0.32	0.16	11.17
E2	10.66	11.33	52.52	0.09	9.02	1.88	0.77	0.10	13.63
E3	13.84	4.18	55.30	0.25	7.23	2.37	0.62	0.42	15.80
E4	7.15	16.59	44.16	0.55	12.71	6.25	0.40	0.23	11.96
E5	12.28	8.25	50.94	0.21	9.51	3.14	0.58	0.34	14.76
E6	7.66	15.62	45.25	0.52	12.23	5.77	0.25	0.18	12.53
E7	11.21	11.00	50.91	0.42	8.96	3.27	0.26	0.22	13.74
F1	7.31	10.21	43.29	0.57	11.98	6.71	0.45	0.33	19.14
F2	8.83	14.52	41.62	0.34	12.74	6.89	0.35	0.13	14.58
F3	8.60	15.34	39.73	0.44	12.90	7.72	0.29	0.19	14.78
F4	10.86	8.58	44.58	0.51	13.92	7.94	0.27	0.27	13.08
F5	15.86	8.71	47.38	0.38	5.73	9.31	0.45	0.50	11.68
F6	21.10	7.79	37.72	0.70	6.26	8.57	0.34	0.60	16.94
F7	15.30	2.20	50.50	0.16	19.34	2.29	0.60	0.11	9.51
F8	7.88	10.05	38.74	0.44	9.34	13.97	0.07	0.35	19.15
F9	5.74	14.54	36.07	0.62	11.03	12.32	0.42	0.14	19.13
F10	5.56	17.72	42.97	0.64	13.92	5.09	0.13	0.28	13.69
G1	9.18	9.58	43.29	0.43	12.03	4.57	0.40	0.19	20.33
G2	7.25	17.07	44.01	0.88	11.92	5.93	0.32	0.14	12.49
G3	8.54	10.27	42.87	1.20	12.30	5.71	0.29	0.17	18.65
H1	8.38	17.35	43.13	0.91	16.01	3.34	0.46	0.15	10.28
H2	9.13	12.82	41.56	0.50	14.23	8.06	0.30	0.35	13.04
H3	7.47	14.49	42.29	0.48	12.23	7.59	0.33	0.27	14.84
H4	8.15	14.09	40.47	0.28	12.17	10.71	0.28	0.04	13.81
H5	8.17	13.04	46.03	0.52	13.07	6.29	0.29	0.19	12.40
H6	7.91	15.87	40.40	0.38	12.50	8.83	0.25	0.15	13.71
H7	7.67	14.36	41.22	0.53	12.70	9.48	0.34	0.21	13.47
H8	10.64	8.71	47.58	0.26	12.59	5.10	0.32	0.30	14.50
H9	8.92	12.31	44.70	0.15	13.77	6.55	0.36	0.32	12.91
H10	11.74	4.01	60.14	0.18	9.34	1.78	0.51	0.24	12.05

TABLE 6 continued. Individual TEM-EDX analyses of ~100 nm regions in fragments of agglutinitic glass from soil 10084. Data are presented in oxide wt.% and include data for fragments I to N.

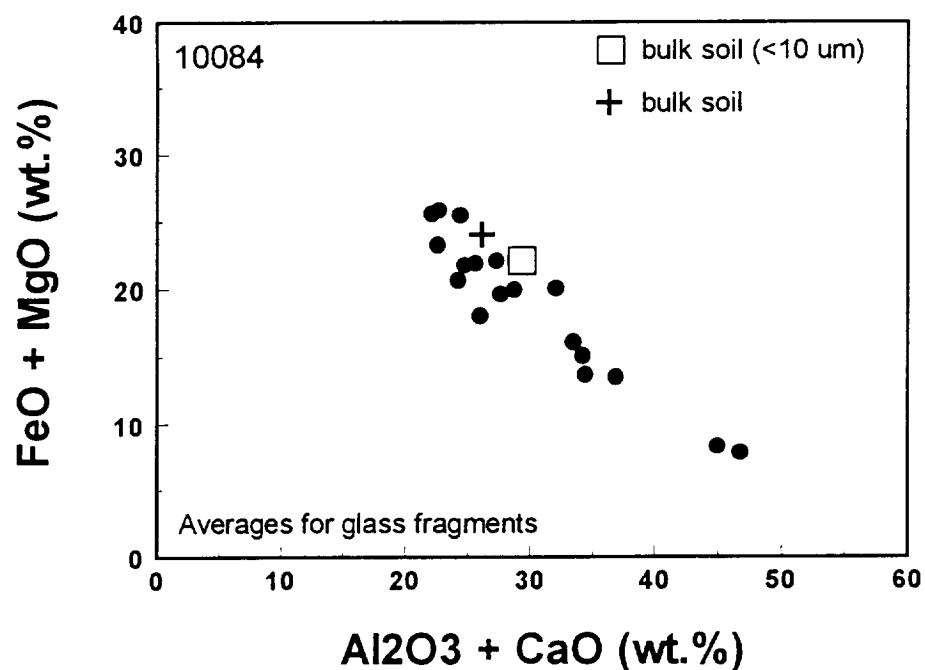
EDX Analyses of Agglutinitic Glass Fragments (A to N) - Soil 10084

(wt.%)	MgO	Al ₂ O ₃	SiO ₂	SO ₃	CaO	TiO ₂	Cr ₂ O ₃	MnO	FeO
I1	1.16	32.48	47.14	0.25	16.52	0.45	0.03	0.20	1.78
I2	8.14	17.14	44.36	0.74	14.11	5.07	0.22	0.13	10.09
I3	12.37	4.24	54.46	0.16	13.14	2.76	0.28	0.24	12.35
I4	4.93	12.49	44.92	0.77	13.72	8.03	0.41	0.31	14.43
I5	4.80	12.43	44.04	0.46	13.24	8.27	0.62	0.26	15.87
I6	7.71	11.34	43.19	0.31	11.76	9.38	0.41	0.34	15.57
I7	5.01	12.65	43.35	0.58	12.96	7.60	0.30	0.32	17.24
I8	6.70	13.93	43.91	0.42	12.75	6.56	0.31	0.24	15.17
I9	7.46	14.05	43.68	0.48	11.82	6.66	0.39	0.31	15.15
I10	4.10	12.89	43.64	0.33	13.67	8.98	0.42	0.19	15.79
I11	4.16	12.66	43.98	0.41	13.75	8.80	0.33	0.22	15.69
J2	4.49	19.04	35.41	0.42	13.02	11.61	0.26	0.18	15.56
K1+K,N	1.70	18.08	69.73	0.16	4.03	0.78	0.02	0.09	2.27
K2	9.12	13.16	42.54	1.13	11.50	6.38	0.27	0.16	15.74
K3	9.52	12.43	40.48	0.97	11.44	6.90	0.27	0.26	17.71
K4	1.18	33.66	44.03	0.04	19.01	0.20	0.00	0.00	1.95
K5	7.07	18.53	42.06	0.46	13.98	5.78	0.35	0.18	11.59
K6	5.98	18.80	38.96	0.94	14.31	8.56	0.22	0.07	12.46
K7	2.85	28.94	43.57	0.28	16.84	2.11	0.39	0.04	4.98
K8	5.87	19.67	43.92	0.41	15.07	2.92	0.27	0.17	11.72
K9	8.13	12.72	41.75	0.59	12.73	7.86	0.29	0.25	15.67
K10	6.93	19.11	42.26	0.42	13.86	5.18	0.21	0.25	11.78
K11	5.21	25.34	42.57	0.31	14.75	3.70	0.44	0.20	7.46
L1	6.36	25.89	47.64	0.28	14.89	0.45	0.21	0.00	4.32
L2	7.31	15.79	43.36	0.43	12.70	6.65	0.57	0.22	12.97
L3	5.11	26.29	50.29	0.30	14.06	0.37	0.17	0.06	3.34
L4	7.64	16.83	41.03	0.16	13.01	6.74	0.65	0.14	13.81
L5	5.96	25.58	48.07	0.88	14.52	0.36	0.06	0.08	4.49
L6	7.89	23.61	47.53	0.93	13.72	0.66	0.14	0.12	5.39
L7	7.31	24.68	48.47	0.20	13.85	0.46	0.26	0.07	4.70
L8	7.84	24.29	48.14	0.31	13.98	0.48	0.21	0.10	4.65
L9	7.21	21.18	48.92	0.74	12.33	0.67	0.17	0.10	8.68
L10	6.39	26.42	47.60	0.25	14.92	0.48	0.16	0.07	3.72
M1	7.27	15.03	40.47	0.34	13.00	8.50	0.29	0.26	14.83
M2	6.96	14.00	43.59	0.53	12.28	7.64	0.37	0.19	14.24
M3	6.79	13.81	44.10	0.66	11.78	7.23	0.32	0.23	15.09
M4	5.43	9.90	39.32	1.32	7.98	15.04	0.38	0.35	20.27
M5	6.59	14.63	49.27	0.47	11.13	6.14	0.18	0.14	11.45
N1	3.50	27.83	45.17	0.29	17.12	1.17	0.05	0.08	4.79
N2	1.08	27.68	42.12	0.63	15.68	1.57	0.10	0.05	11.07
N3	0.94	32.38	45.80	0.25	17.79	0.18	0.06	0.06	2.54
N4	4.66	14.82	48.58	0.58	11.15	6.34	0.27	0.22	13.38
N5	7.40	14.18	42.79	0.50	10.02	11.29	0.36	0.20	13.25
N6	5.87	16.63	42.07	1.28	12.09	7.56	0.30	0.11	14.08
AVG	7.38	16.30	44.84	0.50	12.69	5.67	0.30	0.20	12.11
+/-	0.37	0.82	2.24	0.25	0.63	0.28	0.15	0.10	0.61
Bulk									
Soil:	7.2	16.3	41.3	0.19	12.7	7.3	0.29	0.18	15.1

TABLE 7. Bulk compositions of agglutinitic glass fragments (fragments A to N6) in oxide wt. %.

Bulk Analyses of Agglutinitic Glass Fragments (A to N) - 10084

	MgO	Al ₂ O ₃	SiO ₂	SO ₃	CaO	TiO ₂	Cr ₂ O ₃	MnO	FeO
A	5.12	21.37	46.57	1.08	13.04	4.00	0.20	0.12	8.58
B	9.91	11.09	44.77	0.27	11.02	6.45	0.50	0.31	15.69
C	5.58	20.76	44.94	0.36	13.43	5.16	0.12	0.15	9.51
D	8.68	14.66	42.52	0.31	12.61	7.29	0.33	0.19	13.41
E	9.91	12.06	48.94	0.37	10.49	4.18	0.46	0.24	13.37
F	10.70	10.97	42.26	0.48	11.72	8.08	0.34	0.29	15.17
G	8.32	12.31	43.39	0.84	12.08	5.40	0.34	0.17	17.16
H	8.82	12.71	44.75	0.42	12.86	6.77	0.34	0.22	13.10
I	6.05	14.21	45.15	0.45	13.40	6.60	0.34	0.25	13.56
J	4.49	19.04	35.41	0.42	13.02	11.61	0.26	0.18	15.56
K	5.78	20.04	44.72	0.52	13.41	4.58	0.25	0.15	10.30
L	6.90	23.06	47.11	0.45	13.80	1.73	0.26	0.10	6.61
M	6.61	13.47	43.35	0.66	11.23	8.95	0.31	0.23	15.18
N1	3.50	27.83	45.17	0.29	17.12	1.17	0.05	0.08	4.79
N23	1.01	30.03	43.96	0.44	16.74	0.88	0.08	0.06	6.81
N4	4.66	14.82	48.58	0.58	11.15	6.34	0.27	0.22	13.38
N5	7.40	14.18	42.79	0.50	10.02	11.29	0.36	0.20	13.25
N6	5.87	16.63	42.07	1.28	12.09	7.56	0.30	0.11	14.08
AVG	6.63	17.18	44.25	0.54	12.74	6.00	0.28	0.18	12.19



ORIGINAL PAGE IS
OF POOR QUALITY

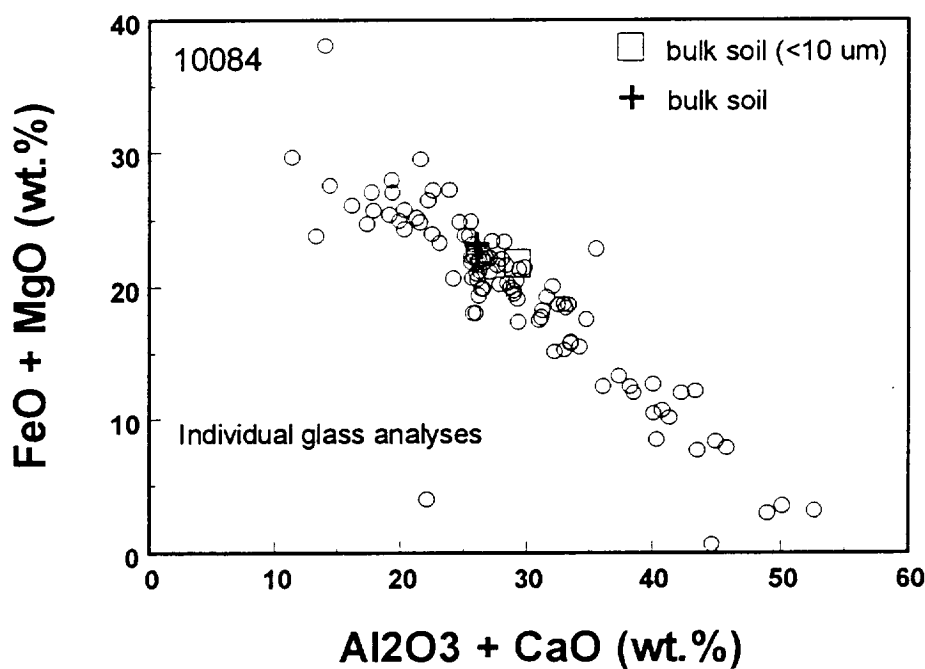


FIGURE 50. Compositions of agglutinitic glass fragments in 10084. Bulk compositions are plotted in the top figure, while the individual analyses are shown in the bottom figure. The bulk soil composition (open box) and the composition of the <10 um fraction (+) are also plotted.

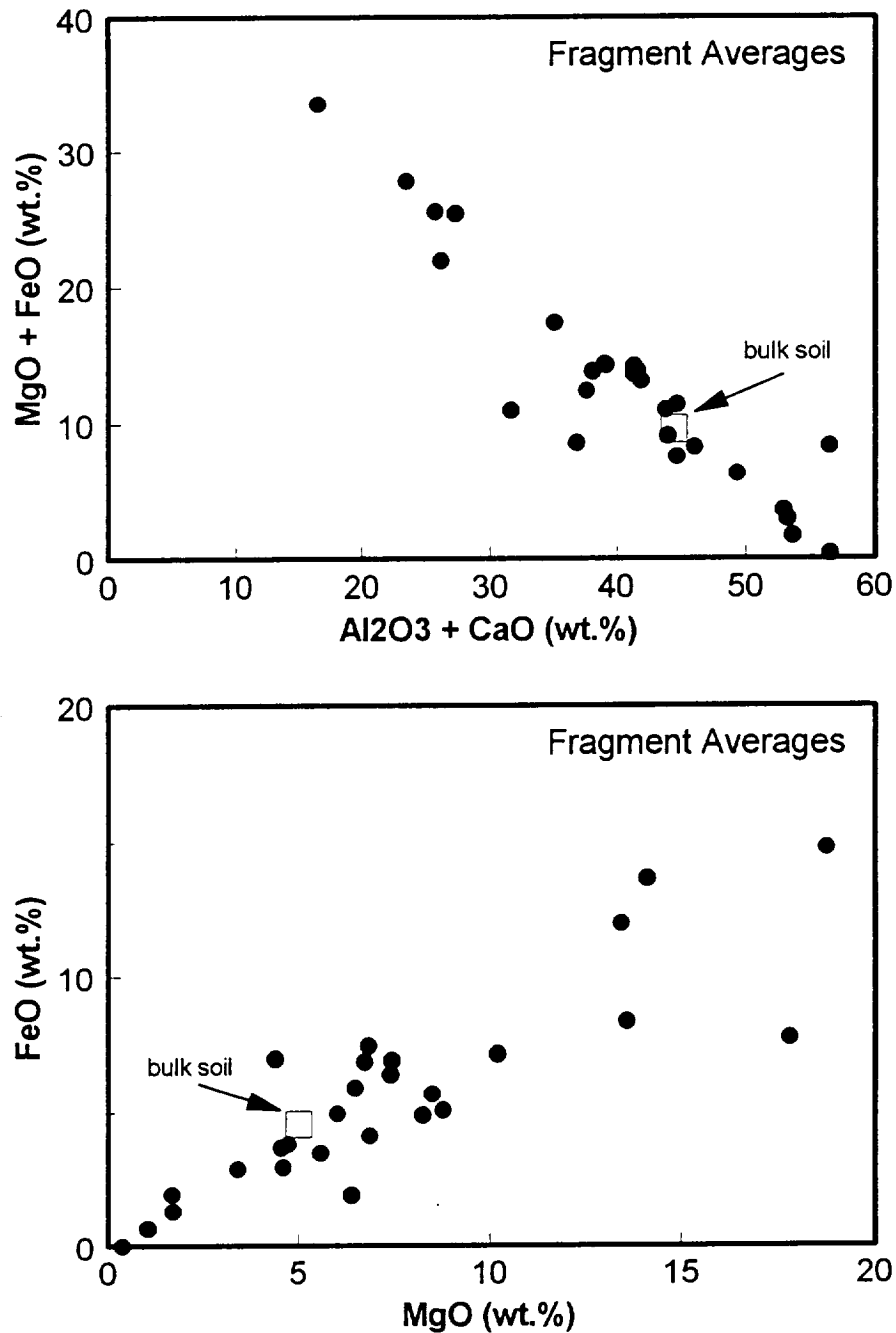


FIGURE 51. TEM-EDX analyses of agglutinitic glass fragments in 61221. The top figure shows the well known mafic-to-felsic trend in bulk composition, while the bottom figure shows the observed positive correlation between Mg and Fe. The wide range in composition is similar to that observed in mature soils.

TABLE 8. TEM-EDX bulk analyses of agglutinitic glass fragments in the immature highlands soil 61221. Data are presented in oxide wt.% except for sulfur which is listed in element wt.%.

TABLE 1. TEM-EDX analyses of agglutinitic glass fragments in 61221.

Analysis	SiO ₂	Al ₂ O ₃	CaO	MgO	TiO ₂	S	Cr ₂ O ₃	FeO	Na ₂ O
22	45.78	28.32	15.66	5.59	0.33	0.10	0.23	3.47	0.51
23	44.99	30.10	15.94	4.55	0.05	0.04	0.10	3.67	0.55
24	44.42	28.25	15.56	6.88	0.11	0.00	0.16	4.10	0.52
26	41.21	28.41	16.27	4.39	0.13	0.85	0.19	6.96	1.59
27	45.24	24.57	13.02	6.50	0.78	0.89	0.19	5.89	2.92
28	45.25	16.96	10.36	13.45	0.64	0.27	0.11	11.96	1.00
29	46.19	24.52	13.55	7.43	0.64	0.14	0.15	6.38	0.98
30	52.68	24.21	12.60	4.73	0.24	0.66	0.00	3.80	1.09
33	42.85	36.07	20.45	0.36	0.00	0.00	0.00	0.00	0.27
35	43.81	31.79	21.83	1.02	0.00	0.06	0.17	0.66	0.66
39	43.64	28.06	13.81	8.26	0.22	0.60	0.13	4.86	0.41
40	43.37	27.12	14.50	8.78	0.12	0.45	0.21	5.06	0.41
41	43.05	27.05	14.29	8.51	0.12	0.65	0.25	5.66	0.41
45	46.88	13.36	10.15	14.12	0.64	0.30	0.64	13.64	0.27
110	48.33	15.65	10.09	17.80	0.32	0.07	0.00	7.73	0.00
124	50.12	16.55	9.66	13.60	1.73	0.00	0.00	8.33	0.00
138	43.60	25.13	14.02	6.85	2.89	0.09	0.00	7.43	0.00
147	43.46	33.68	19.25	1.65	0.00	0.03	0.00	1.94	0.00
154	43.61	35.40	17.84	1.67	0.00	0.18	0.00	1.31	0.00
162	44.23	32.77	16.56	3.39	0.02	0.15	0.00	2.88	0.00
173	47.55	29.38	15.31	4.60	0.00	0.22	0.00	2.94	0.00
174	47.11	16.78	18.29	10.21	0.43	0.04	0.00	7.13	0.00
182	49.49	9.90	6.61	18.75	0.21	0.23	0.00	14.80	0.00
184	35.09	37.20	19.27	6.41	0.00	0.12	0.00	1.91	0.00
193	44.28	25.80	15.52	6.75	0.80	0.00	0.00	6.85	0.00
195	46.41	24.00	14.99	7.46	0.20	0.05	0.00	6.89	0.00
196	56.85	21.85	9.84	6.03	0.02	0.50	0.00	4.93	0.00
AVG	45.54	25.66	14.64	7.40	0.39	0.25	0.09	5.60	0.43
St.Dev.	3.93	7.11	3.64	4.73	0.63	0.27	0.14	3.64	0.65
bulk soil	45.35	28.25	16.21	5.02	0.49	0.06	0.00	4.55	0.42

61181

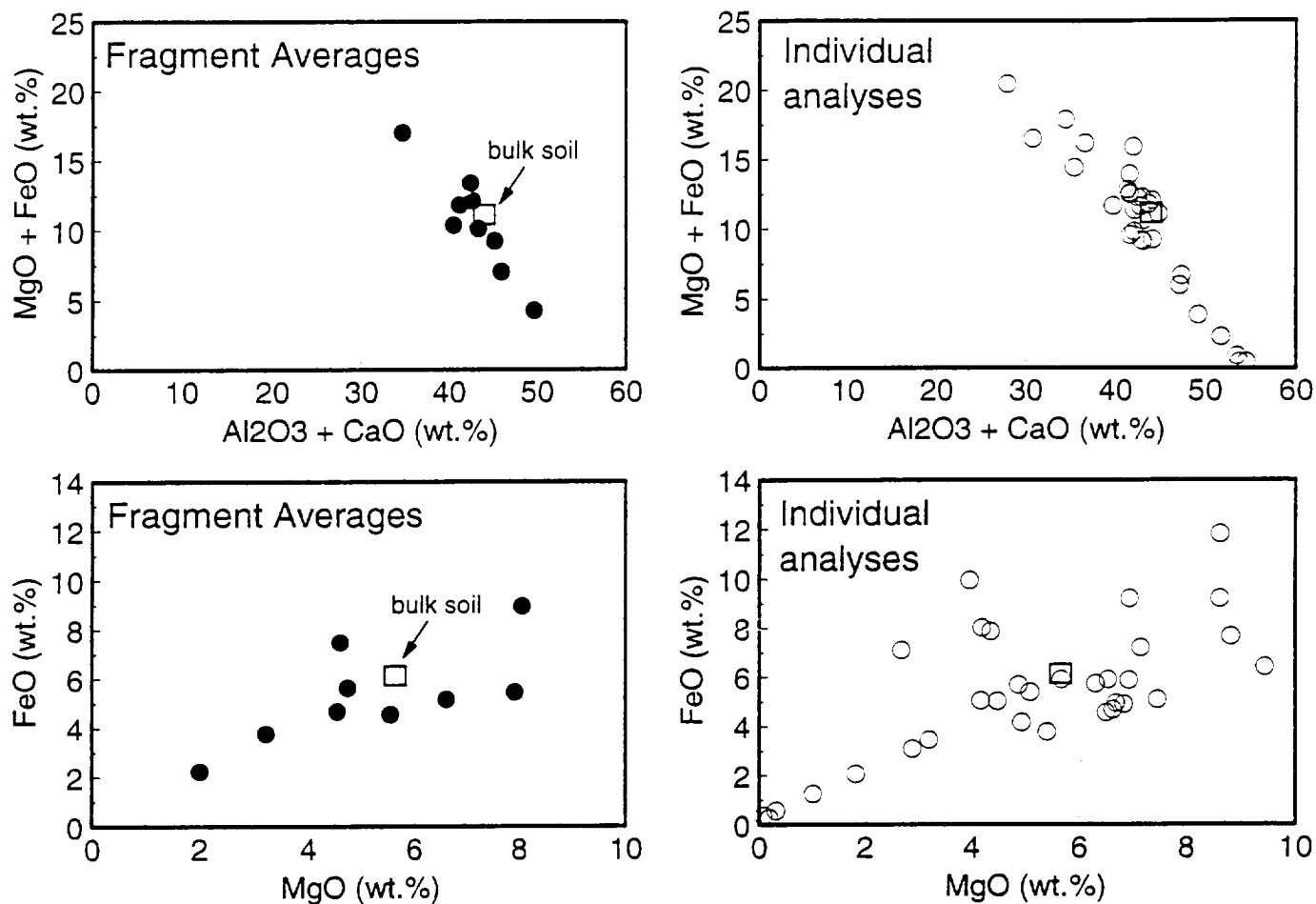


FIGURE 52. Compositional data for fragment averages and the individual analyses of agglutinitic glass in soil 61181 on plots of $\text{MgO} + \text{FeO}$ versus $\text{Al}_2\text{O}_3 + \text{CaO}$, and on plots of MgO versus FeO .

72501

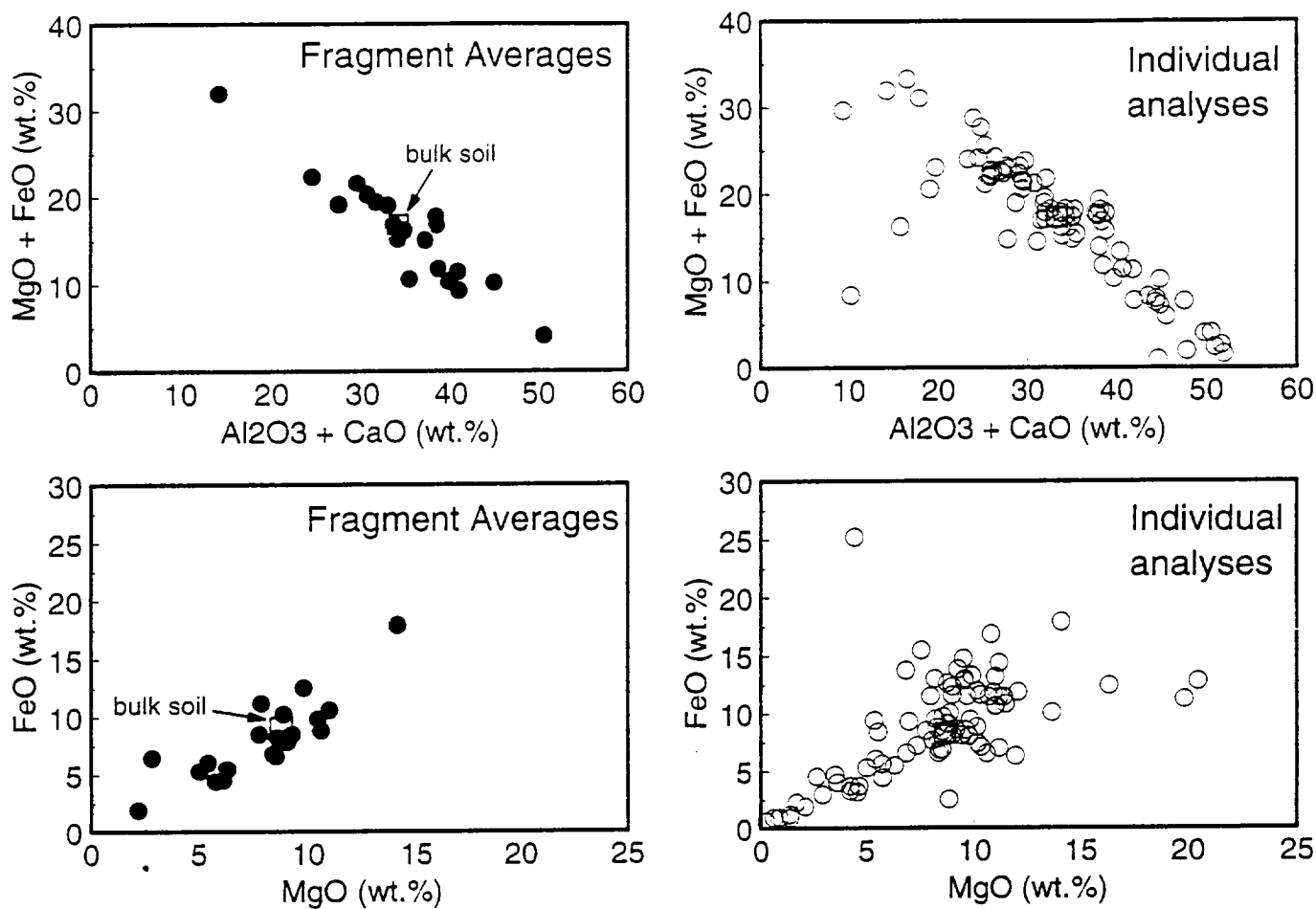


FIGURE 53. Compositional data for fragment averages and the individual analyses of agglutinitic glass in soil 72501 on plots of MgO + FeO versus Al₂O₃ + CaO, and on plots of MgO versus FeO.

TABLE 9. Individual TEM-EDX analyses of agglutinitic glass (fragments A to I) in the mature highlands soil 61181. Data are presented in oxide wt.% except for sulfur which is listed in element wt.%.

Individual EDX Analyses of Agglutinitic Glass Fragments (A to I) from 61181

# (wt.	Na2O	MgO	Al2O3	SiO2	S	K2O	CaO	TiO2	Cr2O3	FeO
A1	1.04	4.94	27.12	44.81	0.39	0.69	15.99	0.57	0.28	4.16
A2	0.67	5.41	26.91	45.30	0.62	0.42	16.00	0.63	0.27	3.76
A3	0.47	6.31	26.59	41.65	0.62	0.29	17.49	0.65	0.20	5.72
B1	0.77	8.62	10.55	48.99	0.83	0.18	17.39	0.62	0.24	11.81
B2	0.52	6.94	25.13	43.24	1.01	0.25	16.29	0.53	0.22	5.88
B3	0.81	8.62	19.77	45.43	0.53	0.21	14.68	0.56	0.19	9.20
C1	0.45	6.63	26.48	44.90	0.25	0.22	15.68	0.62	0.11	4.68
C2	0.49	6.54	26.17	44.40	0.19	0.04	15.45	0.68	0.15	5.90
C3	0.46	6.69	25.34	46.68	0.57	0.21	14.42	0.57	0.12	4.94
D1	0.72	6.95	22.63	43.31	1.65	0.87	14.01	0.37	0.29	9.20
D2	0.98	6.51	28.79	41.80	0.26	0.36	16.11	0.42	0.21	4.56
D3	0.26	0.20	34.83	44.90	0.26	0.15	19.00	0.00	0.13	0.27
E1	1.00	7.16	19.66	47.52	0.55	0.34	15.82	0.49	0.25	7.20
E2	0.93	8.82	18.35	49.92	0.74	0.27	12.44	0.56	0.32	7.66
E3	0.36	0.33	35.21	44.91	0.20	0.02	18.30	0.00	0.13	0.55
F1	0.61	2.69	26.03	46.11	0.66	0.18	16.10	0.27	0.26	7.09
F2	0.51	2.89	30.16	45.64	0.08	0.13	17.07	0.35	0.10	3.08
F3	0.57	0.09	35.70	44.11	0.17	0.09	18.89	0.00	0.03	0.36
F4	0.83	3.21	29.35	44.10	0.18	0.24	18.06	0.38	0.20	3.45
G1	0.73	1.84	31.46	45.14	0.20	0.15	17.87	0.43	0.14	2.05
G2	0.29	5.68	26.40	44.25	0.06	0.13	16.47	0.58	0.24	5.90
G3	0.00	4.88	26.90	44.97	0.29	0.23	16.21	0.70	0.14	5.68
G4	0.07	3.97	26.40	42.51	0.76	0.35	15.25	0.50	0.25	9.94
H1	0.05	4.20	26.81	43.45	0.49	0.45	15.69	0.63	0.22	8.01
H2	0.15	4.36	26.83	42.88	0.32	0.25	16.16	1.00	0.17	7.87
H3	0.67	4.17	27.18	43.83	0.63	0.88	16.99	0.32	0.28	5.05
H4	0.67	1.03	33.70	44.01	0.36	0.77	18.10	0.00	0.10	1.25
I1	0.74	4.49	25.04	45.73	0.70	0.73	16.66	0.62	0.27	5.03
I2	0.75	6.85	27.15	41.92	0.45	0.58	16.59	0.61	0.20	4.90
I3	0.67	9.44	26.35	38.94	1.03	0.75	15.69	0.48	0.24	6.41
I4	0.68	7.47	26.05	43.10	0.45	0.60	15.56	0.63	0.37	5.09
AVG	0.58	5.09	26.61	44.47	0.50	0.36	16.34	0.48	0.20	5.38
bulk soil	0.51	5.78	27.10	44.60	0.17	0.25	15.56	0.66	0.12	5.47

TABLE 10. TEM-EDX bulk analyses of agglutinitic glass fragments (A to I) in the mature highlands soil 61181. Data are presented in oxide wt.% except for sulfur which is listed in element wt.%.

Bulk Analyses of Agglutinitic Glass Fragments (A to I) in 61181

	Na2O	MgO	Al2O3	SiO2	S	K2O	CaO	TiO2	Cr2O3	FeO
A	0.73	5.55	26.87	43.92	0.54	0.47	16.49	0.62	0.25	4.55
B	0.70	8.06	18.48	45.89	0.79	0.21	16.12	0.57	0.22	8.96
C	0.47	6.62	26.00	45.33	0.34	0.16	15.18	0.62	0.13	5.17
D	0.65	4.55	28.75	43.34	0.72	0.46	16.37	0.26	0.21	4.68
E	0.73	4.75	24.81	47.12	0.54	0.20	15.67	0.33	0.24	5.63
F	0.66	2.01	31.67	44.75	0.16	0.15	17.97	0.29	0.12	2.24
G	0.11	4.62	26.67	43.61	0.38	0.28	15.96	0.68	0.20	7.48
H	0.69	3.23	28.64	44.52	0.56	0.79	17.25	0.31	0.22	3.78
I	0.70	7.92	26.52	41.32	0.64	0.64	15.95	0.57	0.27	5.47
AVG	0.60	5.26	26.49	44.42	0.52	0.37	16.33	0.47	0.21	5.33

TABLE 11. Individual TEM-EDX analyses of agglutinitic glass (fragments a to e) in the mature highlands soil 72501. Data are presented in oxide wt. %.

# (wt. %)	Na2O	MgO	Al2O3	SiO2	SO3	K2O	CaO	TiO2	Cr2O3	FeO
1 a	0.46	10.60	20.31	47.71	0.45	0.17	12.82	0.61	0.39	6.48
2 a	0.78	11.97	21.22	45.06	0.47	0.08	13.07	0.63	0.42	6.29
3 a	0.13	1.71	31.04	45.30	0.48	0.00	18.84	0.03	0.21	2.26
4 a	0.18	8.55	19.26	47.53	1.73	0.13	12.33	1.41	0.44	8.44
5 a	0.64	10.34	22.06	44.99	0.40	0.12	13.07	1.14	0.15	7.08
6 a	0.42	11.06	20.29	42.09	1.98	0.11	11.85	1.08	0.44	10.66
7 a	0.53	11.19	21.96	44.59	0.32	0.11	13.45	0.69	0.19	6.97
8 a	0.04	2.70	29.26	46.47	0.61	0.24	15.68	0.40	0.10	4.50
9 b	0.29	12.08	7.95	48.54	0.06	0.05	15.38	3.10	0.68	11.88
10 b	0.00	7.98	17.22	41.30	0.35	0.18	14.77	6.18	0.52	11.51
11 b	0.00	8.57	17.57	42.65	0.04	0.14	15.01	5.73	0.60	9.69
12 b	0.22	8.82	16.78	44.35	0.00	0.04	15.24	4.87	0.60	9.10
13 b	0.00	6.96	6.85	64.24	0.48	0.17	8.94	1.98	1.08	9.30
14 b	0.00	8.89	13.74	46.45	0.31	0.15	15.00	4.82	0.61	10.03
15 c	0.92	8.76	17.06	42.29	0.30	0.11	12.49	5.02	0.40	12.63
16 c	0.56	8.99	17.59	42.44	0.51	0.25	11.90	4.94	0.48	12.34
17 c	0.73	9.91	15.42	42.45	0.55	0.38	12.21	4.55	0.53	13.28
18 c	0.67	9.54	15.75	43.06	0.60	0.00	11.53	5.23	0.78	12.87
19 c	0.54	9.26	16.76	40.13	0.74	0.14	12.39	5.52	0.65	13.87
20 c	0.13	0.65	32.70	45.75	0.35	0.11	19.30	0.00	0.07	0.94
21 c	0.47	5.57	23.66	43.46	0.12	0.25	14.49	3.13	0.45	8.41
22 c	0.78	9.52	14.40	42.21	0.73	0.24	11.96	4.87	0.52	14.75
23 c	0.57	8.22	23.68	39.95	0.25	0.09	14.25	3.12	0.39	9.49
24 c	0.47	8.18	18.25	42.45	0.45	0.26	12.50	3.72	0.71	13.01
25 d	1.08	10.72	14.89	46.01	0.42	0.10	10.98	3.80	0.58	11.43
26 d	0.94	6.84	11.86	53.33	3.12	1.10	7.20	1.57	0.30	13.75
27 d	1.24	10.16	14.85	46.46	0.25	0.30	10.68	3.56	0.51	11.98
28 d	1.00	11.23	16.22	44.65	0.32	0.12	10.78	3.74	0.51	11.44
29 d	1.03	10.92	15.00	44.78	0.38	0.09	10.89	4.64	0.45	11.81
30 d	1.24	9.58	15.08	44.89	0.19	0.27	11.09	4.23	0.41	13.02
31 d	0.95	10.29	15.09	46.27	0.56	0.20	10.75	3.81	0.47	11.60
32 d	0.78	7.54	11.87	51.46	1.77	0.39	7.85	2.42	0.41	15.51
33 d	1.15	11.01	13.98	45.53	0.23	0.17	10.55	3.86	0.38	13.16
34 d	1.06	9.68	14.14	47.08	0.67	0.43	11.13	3.98	0.36	11.47
35 e	0.49	20.49	9.50	47.20	0.87	0.16	7.06	1.04	0.40	12.79
36 e	0.22	9.78	21.21	45.43	0.29	0.15	12.68	1.74	0.47	8.04
37 e	0.26	4.30	28.20	46.26	0.20	0.07	16.30	0.51	0.23	3.67
38 e	0.39	10.83	14.53	44.22	0.84	0.14	10.26	1.66	0.30	16.85
39 e	1.22	0.28	29.48	52.60	0.16	0.06	15.24	0.03	0.30	0.63
40 e	0.37	16.36	14.59	44.32	0.51	0.00	9.37	1.44	0.64	12.43
41 e	0.34	11.19	14.43	45.23	1.42	0.09	10.85	1.45	0.60	14.40

TABLE 11 continued. Individual TEM-EDX analyses of agglutinitic glass (fragments f to p) in the mature highlands soil 72501. Data are presented in oxide wt.%. The bulk soil composition is given at the bottom of the table for comparison.

Individual EDX Analyses of Agglutinitic Glass Fragments (a to p) - 72501										
# (wt.%)	Na2O	MgO	Al2O3	SiO2	SO3	K2O	CaO	TiO2	Cr2O3	FeO
42 m42	0.00	6.31	25.40	48.04	0.44	0.14	13.19	0.64	0.36	5.48
43 m43	0.00	5.75	28.40	44.27	0.12	0.19	16.57	0.27	0.04	4.42
44 m44	0.46	2.16	33.02	43.26	0.64	0.08	17.61	0.63	0.26	1.88
45 f	0.37	4.46	5.80	18.92	0.76	0.01	3.59	37.09	3.81	25.19
47 f	0.00	1.42	33.46	45.86	0.23	0.11	17.57	0.04	0.40	0.91
48 f	0.55	0.92	31.42	48.40	0.28	0.41	16.51	0.24	0.33	0.96
49 f	0.25	3.68	31.79	42.11	0.58	0.26	15.82	1.13	0.40	3.97
50 f	0.66	3.55	29.30	44.72	0.07	0.27	14.35	1.29	1.18	4.67
51 f	0.38	2.98	29.88	45.07	0.45	0.19	15.78	0.54	1.78	2.95
52 g	0.57	8.84	26.93	45.38	0.18	0.23	14.97	0.09	0.29	2.50
53 g	0.52	8.53	21.93	46.13	0.53	0.12	13.65	1.27	0.42	6.89
54 g	0.49	5.74	26.39	45.60	0.23	0.20	14.35	1.04	0.35	5.61
55 g	0.15	1.40	33.95	44.63	0.39	0.14	17.76	0.09	0.30	1.19
56 g	0.34	4.69	6.74	79.39	0.35	0.18	3.56	0.55	0.54	3.66
57 g	0.84	7.36	18.85	51.07	0.49	0.37	12.28	1.17	0.39	7.18
58 m58	1.02	14.10	6.76	41.99	0.57	0.14	7.51	8.74	1.29	17.88
59 h	0.44	10.14	19.19	46.16	0.58	0.11	12.75	1.27	0.55	8.81
60 h	0.16	8.35	22.49	48.26	0.10	0.12	12.60	1.03	0.34	6.55
61 h	0.07	8.35	20.97	47.37	0.40	0.42	12.90	1.35	0.32	7.84
62 h	0.17	9.41	21.38	45.48	0.33	0.15	12.95	1.69	0.38	8.07
63 h	0.29	8.99	20.11	48.68	0.00	0.19	11.95	1.31	0.37	8.11
64 i	1.20	9.00	18.16	46.42	0.58	0.13	11.28	0.96	0.68	11.60
65 i	0.44	11.50	18.32	44.80	0.45	0.26	10.79	1.92	0.71	10.82
66 i	0.55	13.68	18.42	43.46	0.00	0.00	11.35	1.65	0.78	10.08
67 i	0.86	19.85	11.28	48.06	0.37	0.12	6.64	0.88	0.68	11.26
68 i	0.83	11.41	17.07	44.87	0.84	0.06	10.74	1.70	1.05	11.44
69 i	0.33	4.61	26.26	48.58	0.48	0.12	15.76	0.31	0.43	3.13
70 i	0.35	4.28	29.44	45.82	0.55	0.35	15.03	0.61	0.34	3.24
71 j	2.86	8.41	21.38	41.72	1.52	1.51	12.53	1.37	1.84	6.81
72 k	0.56	11.00	18.34	43.60	0.23	0.27	11.05	3.38	0.73	10.58
73 l	0.35	8.70	24.47	39.85	0.33	0.20	14.34	1.77	0.79	9.13
74 l	0.63	10.17	24.23	40.98	0.39	0.12	13.75	1.51	0.79	7.41
75 l	0.34	9.82	23.40	39.39	0.09	0.08	14.72	1.93	0.70	9.45
76 l	0.46	9.63	23.15	39.97	0.40	0.20	15.09	1.82	0.61	8.55
77 l	0.31	8.08	24.01	42.38	0.37	0.22	14.81	1.38	0.65	7.68
78 l	0.49	9.16	23.45	40.59	0.44	0.13	14.28	1.83	0.83	8.62
79 m	0.16	7.77	21.80	44.32	0.15	0.07	12.82	3.32	0.94	8.48
80 n	0.18	5.45	25.54	44.90	0.12	0.16	15.25	1.59	0.71	6.01
81 n	0.37	5.40	14.02	49.85	0.52	0.58	13.79	4.73	0.99	9.42
82 n	0.31	6.85	25.49	42.96	0.02	0.00	15.00	2.02	0.82	6.55
83 o	0.53	8.62	23.61	41.23	0.35	0.21	14.78	1.77	0.53	8.20
84 p	0.30	5.03	24.17	46.33	0.20	0.09	15.54	1.26	1.58	5.28
AVG	0.52	8.18	20.07	44.79	0.48	0.19	12.73	2.56	0.60	8.67
bulk soil	0.43	8.5	20.6	45.1	0.29	0.17	12.2	1.4	0.23	8.6

TABLE 12. TEM-EDX bulk analyses of agglutinitic glass fragments (A to P) in the mature highlands soil 72501. Data are presented in oxide wt.%.

Bulk Analyses of Agglutinitic Glass Fragments (A to P) - 72501

#	Na2O	MgO	Al2O3	SiO2	SO3	K2O	CaO	TiO2	Cr2O3	FeO
A	0.40	8.52	23.18	45.47	0.81	0.12	13.89	0.75	0.29	6.59
B	0.09	8.88	13.35	47.92	0.21	0.12	14.06	4.45	0.68	10.25
C	0.58	7.86	19.53	42.42	0.46	0.18	13.30	4.01	0.50	11.16
D	1.05	9.80	14.30	47.05	0.79	0.32	10.19	3.56	0.44	12.52
E	0.47	10.46	18.85	46.47	0.61	0.10	11.68	1.12	0.42	9.83
F	0.37	2.84	26.94	40.85	0.40	0.21	13.94	6.72	1.32	6.44
G	0.49	6.09	22.47	52.03	0.36	0.21	12.76	0.70	0.38	4.51
H	0.23	9.05	20.83	47.19	0.28	0.20	12.63	1.33	0.39	7.88
I	0.65	10.62	19.85	46.00	0.47	0.15	11.66	1.15	0.67	8.80
J	2.86	8.41	21.38	41.72	1.52	1.51	12.53	1.37	1.84	6.81
K	0.56	11.00	18.34	43.60	0.23	0.27	11.05	3.38	0.73	10.58
L	0.43	9.26	23.79	40.53	0.34	0.16	14.50	1.71	0.73	8.47
M	0.16	7.77	21.80	44.32	0.15	0.07	12.82	3.32	0.94	8.48
N	0.18	5.45	25.54	44.90	0.12	0.16	15.25	1.59	0.71	6.01
O	0.53	8.62	23.61	41.23	0.35	0.21	14.78	1.77	0.53	8.20
P	0.30	5.03	24.17	46.33	0.20	0.09	15.54	1.26	1.58	5.28
M42	0.00	6.31	25.40	48.04	0.44	0.14	13.19	0.64	0.36	5.48
M43	0.00	5.75	28.40	44.27	0.12	0.19	16.57	0.27	0.04	4.42
M44	0.46	2.16	33.02	43.26	0.64	0.08	17.61	0.63	0.26	1.88
M58	1.02	14.10	6.76	41.99	0.57	0.14	7.51	8.74	1.29	17.88
AVG	0.54	7.90	21.57	44.78	0.45	0.23	13.27	2.42	0.70	8.07

4.2.g. Analyzing amorphous rims and vapor deposits.

In response to a technical comment on our research presented in *Science*, we have written a response that was published in the the June 17, 1994 issue of *Science*. A copy of the comment and our response is attached in the Appendix. In addition, we also presented additional data and interpretations on the nature of amorphous rims on lunar silicates at the 57th Meeting of the Meteoritical Society in Prague, Czech Republic. It was demonstrated the magnitude of the chemical differences between rims and their hosts were so great, that a major addition of material was deposited on the surfaces of the soil grains either by condensation of impact-derived vapors or via sputter deposition. A copy of the abstract of this presentation as published in *Meteoritics* is attached in the Appendix.

We have also obtained additional analyses of amorphous rims in lunar soils, including the direct analysis of oxygen in both the rims and their host grains (Table 13). Of the 11 soils grains analyzed, 4 show evidence for cation deficiency, 3 have an oxygen deficit, and the remainder show no anomalies. The cation deficiency may be related to irradiation processes in the lunar regolith (similar oxygen anomalies are reported in interplanetary dust particles, see Bradley, *Science*, 1994, vol. 265, p. 925). The "reduced" rims must have some reduced Si in order to achieve stoichiometry (all of the Fe and S in these rims is assumed to be elemental), and this would be consistent with their formation as vapor deposits.

TABLE 13. TEM-EDX analyses (11) of amorphous rims on various lunar soil grains (An=anorthite, opx=orthopyroxene, cpx=clinopyroxene/augite, and crist=cristobalite) from soils 78221 and 10084. Data are presented in element wt.% and arranged so that each core soil grain/rim pair are listed sequentially.

Quantitative TEM-EDX analyses of amorphous rims and their substrates in Apollo 11 and 17 soils.

Analysis (el. wt.%)	O	Mg	Al	Si	S	Ca	Ti	Fe	Soil
242 rim	36.20	5.53	14.42	22.20	0.05	12.08	1.02	8.51	78221
243 core (An)	45.78	0.58	19.72	21.28	0.00	12.64	0.00	0.00	78221
240 rim	50.30	1.34	9.99	31.35	0.03	2.28	1.35	3.36	78221
241 core (opx)	44.74	14.22	4.30	22.72	0.01	3.70	0.44	9.86	78221
26 rim	47.23	2.42	6.33	33.07	0.47	3.25	1.82	5.41	10084
25 core (cpx)	41.35	6.86	1.72	24.38	0.04	7.61	0.59	17.45	10084
21 rim	45.03	3.98	5.15	33.45	0.40	3.11	1.59	7.30	10084
20 core (opx)	44.70	14.75	0.66	26.59	0.00	2.78	0.36	10.15	10084
46 outer rim	43.28	3.85	9.09	23.32	0.59	5.58	2.53	11.77	10084
45 inner rim	43.53	3.22	13.88	23.11	0.32	8.49	1.33	5.37	10084
44 core (An)	46.35	0.17	18.67	22.05	0.00	12.72	0.00	0.04	10084
34 outer rim	52.26	3.97	3.24	29.60	0.59	1.56	1.22	7.56	10084
35 inner rim	44.61	7.72	3.70	34.67	0.21	2.15	0.27	6.67	10084
36 core (opx)	44.97	16.72	0.40	25.85	0.01	1.57	0.16	10.32	10084
208 rim	48.62	5.50	4.01	26.69	0.10	7.61	0.91	6.56	78221
209 core (opx)	43.23	10.49	0.86	24.85	0.10	4.95	0.54	14.98	78221
211 rim	55.06	0.70	9.69	30.67	0.00	3.05	0.00	0.82	78221
210 core (An)	44.46	0.44	19.67	21.82	0.00	13.57	0.00	0.03	78221
214 rim	41.81	0.98	12.67	28.54	0.20	5.55	0.86	9.38	78221
213 core (An)	47.08	0.51	18.36	21.22	0.00	12.83	0.00	0.00	78221
217 outer rim	51.12	0.92	7.66	31.48	0.07	2.63	0.35	5.78	78221
216 inner rim	54.27	0.58	11.37	27.60	0.04	4.04	0.18	1.92	78221
215 core (An)	47.04	0.51	19.12	20.57	0.00	12.70	0.00	0.05	78221
218 outer rim	51.90	0.00	6.25	33.83	0.00	1.48	2.26	4.28	78221
219 inner rim	54.55	0.45	4.66	39.81	0.02	0.41	0.07	0.03	78221
220 core (crist)	51.43	0.01	0.25	48.31	0.00	0.00	0.00	0.00	78221

4.2.h. Analyzing submicrometer glass spheres in regolith samples.

We have obtained over 50 analyses of individual submicrometer glass spheres in two Apollo 16 soils (61221 and 67701, immature and sub-mature, respectively). The data are presented in Tables 14 and 15 and are plotted in Figure 54. These spheres range in composition from essentially pure silica to glasses containing major Ca and Al and only traces of Si (high-Al, si-poor HASP glasses). This range in composition is similar to what we have observed in other lunar soils (Keller *et al.*, 1995 in review). Unlike the submicrometer glasses observed in other highland soils, fractionated compositions (e.g. HASP and the high-Si glasses) comprise a minority of the analyzed spheres. The majority of spheres have "basaltic" compositions and contain sufficient silica for a traditional norm to be calculated. These results may indicate that the abundance of submicrometer glasses with fractionated compositions correlates positively with soil maturity.

We submitted a manuscript describing our results on submicrometer glass spheres in lunar soils to *Geochimica et Cosmochimica Acta* (the manuscript as submitted is attached in the Appendix of our first quarter progress report for this contract), but the editors declined to publish the paper until major revisions are made. These revisions are in progress.

4.2.i. Analyzing selected regolith grains for carbon.

We do not report any analyses for carbon in lunar soil grains. We learned during the summer of 1994 that existing sieve fractions of lunar soil that were available to us for analysis were contaminated with surficial deposits of carbon-bearing material (David S. McKay and co-workers, pers. comm.). In September 1994 we requested new, pristine soil samples from the Lunar Curator at the Johnson Space Center for our analysis, but as of this writing, we have still not received the requested samples.

TABLE 14. TEM-EDX analyses (37) of submicrometer glass spheres in lunar soil 61221. Data are presented in oxide weight % except sulfur which is reported as element wt. %.

Analysis	SiO ₂	Al ₂ O ₃	CaO	MgO	TiO ₂	S	Cr ₂ O ₃	FeO	Na ₂ O
25	46.36	34.76	15.94	1.68	0.00	0.13	0.12	1.01	0.00
31	35.96	32.15	17.75	7.68	0.31	0.15	0.09	5.35	0.56
32	83.54	3.03	2.72	4.46	0.00	0.83	0.03	4.84	0.56
34	43.36	33.36	17.93	1.88	0.00	0.08	0.04	2.31	1.04
37	97.45	1.21	0.22	0.75	0.00	0.12	0.09	0.15	0.00
44	46.59	33.39	17.66	1.00	0.00	0.00	0.03	0.58	0.77
46	16.58	50.95	27.50	3.74	0.00	0.07	0.00	1.16	0.00
98	1.88	64.59	32.50	0.85	0.08	0.03	0.06	0.01	0.00
99	96.77	1.25	0.23	0.93	0.00	0.00	0.10	0.04	0.69
102	67.25	0.19	0.00	1.19	0.00	1.27	0.05	29.29	0.75
103	44.43	3.15	5.51	3.44	0.00	0.27	0.58	42.62	0.00
104	79.06	0.87	0.46	4.51	0.00	0.00	0.25	10.98	3.88
105	43.17	34.00	17.40	1.59	0.00	0.33	0.06	2.91	0.54
106	30.60	37.49	20.18	8.26	0.19	0.00	0.09	3.19	0.00
107	97.26	0.72	0.00	1.01	0.00	0.16	0.20	0.64	0.00
117	43.31	36.55	18.87	1.01	0.00	0.00	0.00	0.26	0.00
118	44.46	31.04	16.51	3.79	0.00	0.06	0.00	4.13	0.00
119	46.65	28.20	14.50	5.50	0.23	0.00	0.00	4.92	0.00
120	46.52	34.35	17.39	1.08	0.00	0.06	0.00	0.60	0.00
121	50.33	1.78	18.31	14.85	0.33	0.00	0.00	14.39	0.00
122	47.46	13.56	14.94	7.02	1.01	0.07	0.00	15.94	0.00
123	45.07	18.89	14.40	13.21	0.02	0.00	0.00	8.41	0.00
131	42.49	30.12	16.34	5.74	0.22	0.09	0.00	4.99	0.00
132	36.31	34.02	19.64	5.06	0.00	0.08	0.00	4.88	0.00
153	46.06	35.47	16.16	1.49	0.00	0.09	0.00	0.74	0.00
171	45.72	36.93	15.09	1.37	0.00	0.07	0.00	0.82	0.00
172	49.80	34.63	13.95	1.09	0.00	0.00	0.00	0.52	0.00
183	44.84	28.48	16.77	4.95	0.00	0.15	0.00	4.81	0.00
190	97.79	1.26	0.18	0.72	0.00	0.00	0.00	0.05	0.00
191	43.77	35.43	19.21	0.84	0.00	0.00	0.00	0.75	0.00
192	45.00	27.36	16.09	9.66	0.03	0.04	0.00	1.81	0.00
194	50.06	35.11	14.24	0.59	0.00	0.00	0.00	0.00	0.00
203	32.11	43.44	16.82	6.61	0.15	0.00	0.00	0.87	0.00
204	46.27	33.17	16.93	1.74	0.00	0.06	0.00	1.83	0.00
205	44.92	33.72	17.92	1.52	0.00	0.07	0.00	1.86	0.00
206	45.46	32.63	17.50	2.00	0.00	0.14	0.00	2.27	0.00
207	45.76	35.96	17.47	0.81	0.00	0.00	0.00	0.00	0.00

TABLE 15. TEM-EDX analyses (15) of submicrometer glass spheres in lunar soil 67701. Data are presented in oxide weight % except sulfur which is reported as element wt.%.

TEM EDX analyses of sub-micrometer glass spheres in 67701

Analysis	SiO ₂	Al ₂ O ₃	CaO	MgO	TiO ₂	S	Cr ₂ O ₃	FeO	Na ₂ O
78	17.89	45.64	24.87	10.31	0.24	0.05	0.06	0.95	0.00
79	44.64	34.72	18.62	0.94	0.00	0.00	0.34	0.34	0.41
80	38.96	37.86	19.18	2.41	0.00	0.13	0.00	1.46	0.00
81	47.64	27.96	15.08	5.92	0.34	0.08	0.00	2.73	0.26
82	44.46	35.54	18.53	0.66	0.00	0.11	0.09	0.07	0.55
83	27.77	36.20	20.45	11.17	0.39	0.00	0.00	4.02	0.00
84	49.08	32.38	14.90	1.92	0.00	0.16	0.00	1.42	0.13
85	92.92	3.11	1.34	0.73	0.00	0.39	0.00	0.25	1.26
86	32.95	27.33	18.24	14.38	1.32	0.01	0.00	5.66	0.11
87	44.68	33.04	17.46	3.15	0.00	0.00	0.00	1.68	0.00
88	42.69	27.64	17.33	7.43	0.06	0.17	0.30	4.13	0.24
89	44.26	32.47	17.92	2.55	0.00	0.08	0.00	2.03	0.69
92	21.71	46.51	24.22	6.85	0.24	0.03	0.00	0.45	0.00
93	31.81	40.39	20.11	6.51	0.13	0.00	0.00	1.05	0.00
94	98.49	0.99	0.01	0.48	0.00	0.00	0.00	0.03	0.00
bulk soil	44.78	28.47	16.87	4.92	0.43	0.00	0.00	4.17	0.53

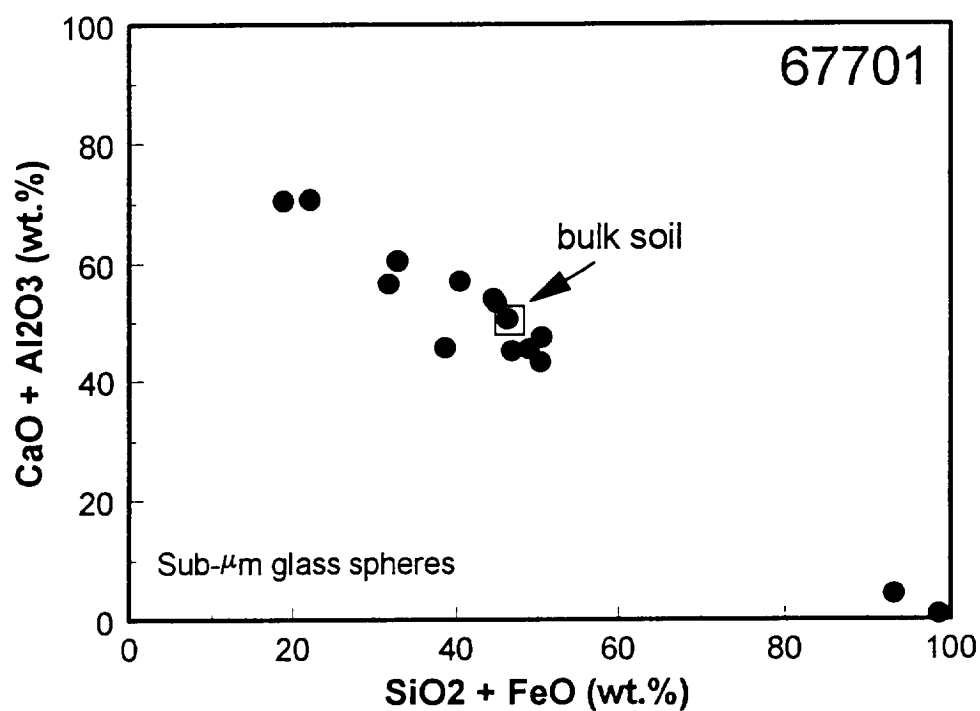
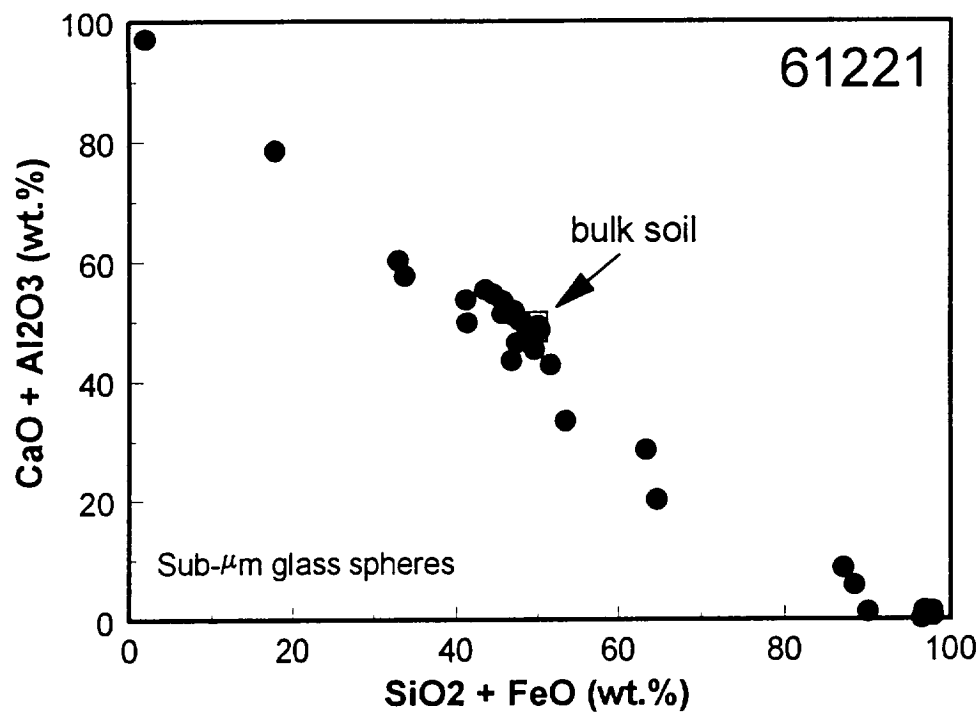


FIGURE 54. Compositions of submicrometer glass spheres in 61221 (top) and 67701 (bottom). The bulk soil composition is indicated by the open box in each plot.

4.2.j. Analyzing selected lunar grains for their reflectance spectra properties.

We have obtained (12) reflectance spectra over the visible wavelength range (380-800 nm) from pyroclastic glass beads from two lunar soils (15401 and 74220). The reflectance data (Figure X) show considerable variation in their absolute reflectivities which is a function of the nature of the particle surface. There is excellent agreement in the spectral shape for glasses from the same soils. For example, all of the analyzed "orange" glass from 74220 shows strong absorption of the shorter wavelengths (yellow to violet) and a major peak at ~700 nm which corresponds to orange-red. All of the "green" glass spectra show a major peak in the yellow-green (~550 nm) with absorption of the shorter and longer wavelengths. These data are summarized by Allen *et al.*, (1994) along with their potential application to remote-sensing of the lunar surface (mapping of pyroclastic deposits).

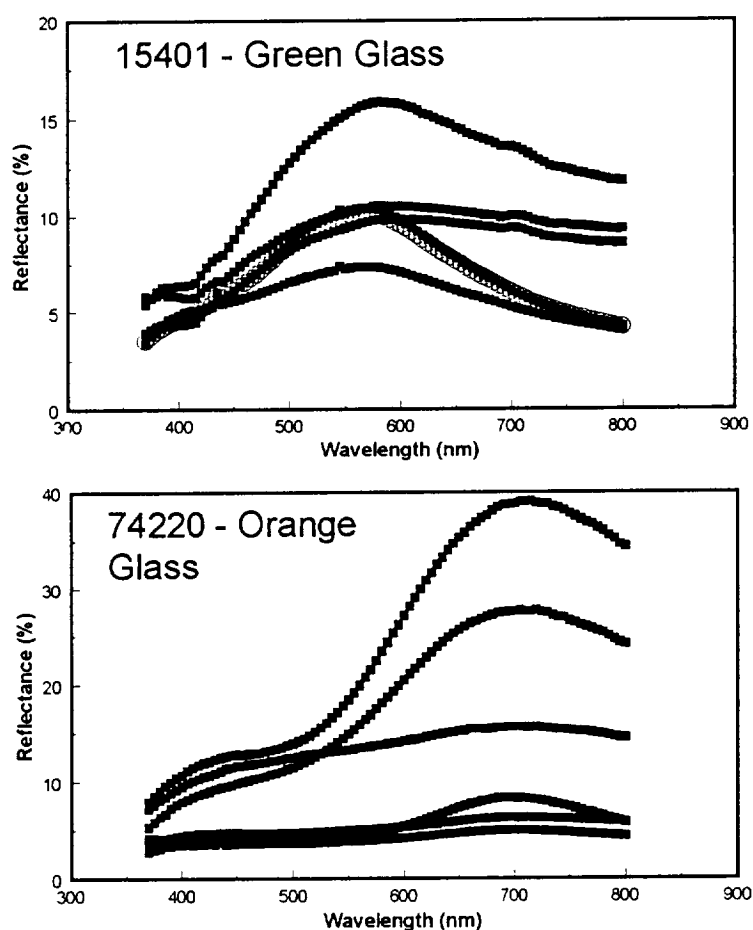


FIGURE 55. Visible reflectance spectra for individual pyroclastic glass beads for lunar soils 15401 and 74220.

APPENDIX - PUBLICATIONS

NEW PROSPECTS FOR ANALYZING LUNAR PYROCLASTIC GLASS

C. C. Allen, Lockheed Engineering & Sciences Co., Houston, TX L. P. Keller and J.P. Bradley, MVA, Inc., Norcross, GA D.E. Brownlee, University of Washington, Seattle, WA
and D. S. McKay, NASA/Johnson Space Center, Houston, TX

Pyroclastic glass particles of diverse compositions are sparsely distributed in the lunar soil. Numerous suspected pyroclastic deposits have been pinpointed on the nearside. However, a dearth of pure samples large enough for spectral study, coupled with the kilometer spatial resolution of Earth-based telescope spectrometry, make it difficult to remotely analyze these deposits or tie most glasses to specific sources. Two developments should soon improve this situation. First, the technique of microscope photometry combined with microprobe analysis for the first time allows correlation of the reflectance spectra and chemical compositions of individual glass particles. Second, the Clementine spacecraft will provide multispectral images of pyroclastic deposits at much higher spatial resolution than is currently achievable. These developments, combined with traditional laboratory and telescope studies, should allow compositions of many pyroclastic deposits and sources of many soil particles to be determined.

Pyroclastic Glass. Lunar pyroclastic glass particles, tens to hundreds of micrometers in diameter, span a large range of chemical compositions. Delano (1) has identified 25 distinct glasses in lunar soil. Among these glasses, thin section colors range from green to yellow to orange to red with increasing TiO_2 content. Some of these compositions are also represented by devitrified black particles, darkened by myriad submicrometer ilmenite and spinel crystals.

Of these diverse glass types the reflectance spectra of only three are known (2,3). Sample 74220 is the high-Ti "orange soil" from Shorty Crater. Sample 74001 is a core dominated by almost pure concentrations of black glass, the devitrified equivalent of 74220. Sample 15401 contains predominantly low-Ti green glass. No other pyroclastic glasses have been found in sufficient quantity (10 mg = 10,000 particles) to permit classical reflectance spectrometry (C.M. Pieters, personal communication).

If reflectance spectra could be correlated to chemical composition it might allow remote analysis of many lunar pyroclastic glass deposits. Such determinations could be ambiguous, however, if the deposits are heterogeneous. The extensive Taurus-Littrow dark mantle, for example, contains mainly black glass like 74001, mixed with orange glass similar to 74220. This determination was made based on telescopic measurements (4, 5) with 5-20 km spatial resolutions. Homogeneous deposits of smaller dimensions, if they exist on the Moon, cannot be identified by Earth-based measurements.

Microscope Photometry. We have for the first time collected reflectance spectra of individual pyroclastic glass spheres as small as $\sim 20 \mu\text{m}$ in diameter. Measurements were made over the wavelength range of 380- to 800-nm relative to a BaSO_4 reference standard. Spectra were obtained by scanning over the wavelength range in 5 nm steps. Measuring apertures were optimized to individual particle diameters. Further details of the microscope photometric technique are reported by Bradley et al. (6).

Figure 1 shows typical spectra of $\sim 100 \mu\text{m}$ diameter glass particles from samples 74220 (orange), 74001 (black), and 15401 (green). The orange glass spectrum is characterized by a gradual rise from the UV to around 600 nm, followed by a steep rise and a broad absorption feature longward of 700 nm. The green glass shows a rapid rise to approximately 560 nm, followed by a deep absorption feature centered in the infrared. These bands have been correlated with the abundances and oxidation states of iron and titanium in the glasses (7). The black glass spectrum is essentially flat throughout the measured range. The locations of absorption features closely match those measured for bulk samples (2,3), though the bulk samples exhibit more pronounced red slopes.

NEW PROSPECTS FOR ANALYZING LUNAR GLASS: Allen C.C. et al.

The peak reflectivities of individual glass particles depend on size and degree of roughness, with broken particles having the most prominent spectral features. Values for green glass range from 7-16%, while orange glass ranges from 8-40%. In both cases slope trends and peak locations are similar among all particles. Black glasses all have nearly identical spectra.

Particles which have been measured by microscope photometry can subsequently be classified by chemical type using the electron microprobe. Thus, chemical compositions can be correlated with reflectance spectra even for extremely rare particles. We intend to use this combination of techniques to quantify the colors of the entire range of pyroclastic glasses, using individual particles picked from lunar soil samples.

Clementine. The Clementine spacecraft, due to map the moon from polar orbit in 1994, will carry four multispectral sensors. The high resolution camera, with an optimum resolution of 23 m, has been targeted to all identified pyroclastic deposits on the nearside. It will provide multispectral images through filters centered at 415, 560, 650, and 750 nm.

We analyzed our spectra of individual particles to determine if the three glass types could be distinguished using only data from the Clementine filter passbands. To emphasize spectral features and minimize albedo differences, reflectivity ratios among several bands were compared. Figure 2 shows a plot of 650/560 nm ratios vs. 750/560 nm ratios. This presentation was chosen to emphasize differences among the spectral types.

Figure 2 demonstrates a strong clustering of reflectivity ratios according to particle composition. We conclude that Clementine data would be adequate to differentiate among deposits of essentially pure orange, black, and green glass. With a resolution of 23 m, the Clementine high-resolution sensor could locate such concentrations in larger deposits which are heterogeneous at telescope resolution.

Determining the chemical compositions of pyroclastic glass deposits will significantly aid our understanding of lunar volcanism. Similarly, locating the sources of individual glass particles in lunar soils will place new constraints on models of regolith development.

References. (1) Delano, 1986, *PLPSC16*, D201 (2) Adams et al., 1974, *PLSC5*, 171 (3) Heiken et al., 1991, *Lunar Sourcebook*, p.211 (4) Gaddis et al., 1985, *Icarus*, 61, 461 (5) Hawke et al., 1991, *PLPSC21*, 377 (6) Bradley et al., 1994, this volume (7) Bell et al., 1976, *PLSC7*, 2543

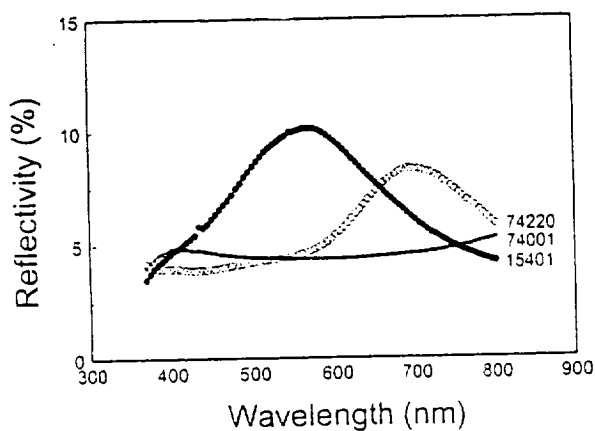


Figure 1. Representative spectra of individual pyroclastic glass particles ~100 μ m in diameter

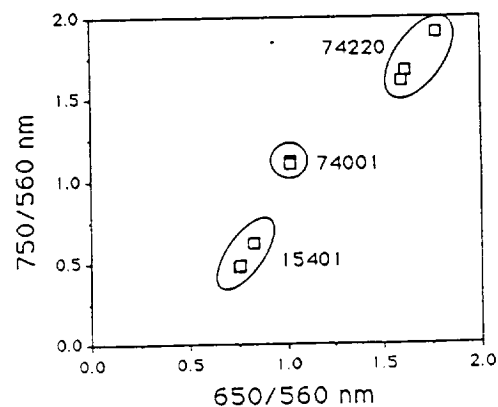


Figure 2. Pyroclastic glass particle color ratios using Clementine filter passbands

THE CONTRIBUTION OF VAPOR DEPOSITION TO AMORPHOUS RIMS ON LUNAR SOIL GRAINS. Lindsay P. Keller¹ and David S. McKay², ¹MVA, Inc., 5500/200 Oakbrook Parkway, Norcross, GA 30093, and ²SN6, NASA Johnson Space Center, Houston, TX 77058.

Our recent analytical electron microscope study of lunar soils showed that the ~60-nm-wide amorphous rims surrounding many lunar soil grains exhibit distinct compositional differences from their hosts [1]. On average, the amorphous rim compositions reflect the local bulk soil composition with the exceptions of silicon and sulfur which are enriched relative to the bulk soil. These chemical trends led us to propose that the amorphous rims were in fact deposits of impact-generated vapors that were produced during regolith gardening [1]; a hypothesis that runs contrary to the generally accepted view that the rims are produced through amorphization of the outer parts of mineral grains by interaction with the solar wind (e.g. [2]). Here we report our analytical data for amorphous rims on individual minerals in lunar soils in order to show that the magnitude of the chemical differences between rim and host are so great that they require a major addition of foreign elements to the grain surfaces.

Table 1 lists the average composition of amorphous rims as a function of host mineralogy as determined in microtome thin sections using energy-dispersive x-ray spectrometry in the transmission electron microscope (see [1] for analytical details). Rims on cristobalite (essentially pure SiO₂) contain major Mg, Al, Ca, Ti, and Fe; these elements are clearly foreign to cristobalite, and so must have been deposited on the surfaces of grains either by sputter deposition or by condensation of impact-derived vapors. Similar arguments can be made for the amorphous rims on olivine [(Mg,Fe)₂SiO₄] grains, which contain major Ca, Al, and Ti that are normally present in olivine at only trace levels, and rims on anorthite (An₉₅₋₉₉) which contain major Mg, Ti, and Fe that are also present at trace concentrations in the host plagioclase. As the host mineral becomes chemically more complex (as in augite) the chemical differences are not as clear as the preceding examples. But overall, the average rim compositions are remarkably similar and are independent of the host grain mineralogy (Table 1). These data indicate that much of the "thickness" of amorphous rims consists of elements that are not indigenous to the host grain.

Whether there are "sputtering" or radiation effects superimposed on the vapor deposited material can be debated. We do not explicitly exclude the effects of radiation damage as a contributing factor to the formation of amorphous rims, we are merely emphasizing the major (and generally overlooked) role played by condensed vapors in the formation of amorphous rims on lunar soil grains.

Acknowledgements. This work was supported by NASA RTOP 152-17-40-21 and NASA Contract NAS 9-18992.

References. [1] Keller, L. P. and McKay, D. S. (1993) *Science*, 261, 1305. [2] Borg, J. et al. (1980) in *The Ancient Sun*, Eds. R. O. Pepin et al., 431.

TABLE 1. Average compositions of amorphous rims on specific minerals in lunar soils 10084 and 78221.

Host Phase	Na ₂ O	MgO	Al ₂ O ₃	SiO ₂	S	CaO	TiO ₂	FeO
Anorthite	0.1	3.5	20.1	53.4	0.7	9.7	4.0	8.5
Augite	0.2	6.6	11.3	56.1	0.6	9.7	4.2	11.3
Cristobalite	0.2	5.4	11.5	59.2	1.7	7.3	3.9	10.8
Olivine	0.6	8.8	15.5	47.6	0.4	8.8	3.6	14.7

Several related fragments from our second cluster, L2005#31, are pictured in the JSC Cosmic Dust Catalog [11]. These fragments have chondritic EDX spectra and show either porous or smooth surface morphologies. Three fragments of this cluster have been analyzed previously by others; two of these are typical pyroxene-rich, porous, anhydrous IDPs, L2005F31 [Keller, pers. comm] and L2005F39 [Zolensky, 12 and pers. comm], while the third fragment (L2005F37) is a saponite-dominated particle [Klöck, pers. comm.]. We obtained 5 additional fragments of L2005#31 in order to determine whether this cluster particle was only partly hydrated. Major element compositions are chondritic (within 2xCI) for all five fragments. From our group of three fragments analyzed in the TEM, two were anhydrous and were dominated by pyroxene. They contained carbonaceous material, Ni-poor sulfides, glass, Fe-Ni metal, chromite, and discontinuous magnetite rims. The third fragment contained no anhydrous silicates; it is composed of saponite, sulfides with Ni ranging from 3-21 wt.%, chromite, and rare Si-rich glass. Although cluster L2005#31 contains both anhydrous and hydrated IDPs, the fragments have several anhydrous phases in common which strongly indicates that the fragments are derived from the same parent cluster.

Reflectance spectra from the fragments show two major trends: three spectra are flat or gently rise into the red and two fall steeply into the red. The TEM data indicate that fragments in the first group are dominantly anhydrous while the latter group are hydrated fragments.

Heating History of Our Second Cluster The presence of minor, discontinuous magnetite rims indicates that fragments from L2005#31 were heated little during atmospheric entry. Another related fragment, L2005F38, was analyzed by [13]; it had a 50% He release temperature of 530 °C which indicates that this fragment also experienced minor atmospheric heating.

How do individual clusters differ from each other? This and previous work show that cluster particles can be composed of anhydrous, hydrated, or a mixture of both anhydrous and hydrated fragments. Prior work on one anhydrous cluster, L2008#5, showed that the chemical compositions and mineralogy widely varied from fragment to fragment (i.e., some were dominated by Fe-Ni sulfides, olivine, or by carbon and pyroxene) [1,2]. In this study, our two cluster particles are chemically and mineralogically different from the anhydrous cluster previously studied. Fragments in cluster L2011#5 are composed mainly of serpentine and are remarkably similar in chemistry, mineralogy, and reflectance spectra; this homogeneity is a likely consequence of extensive aqueous alteration on its parent body. However, cluster L2005#31 contains *both* anhydrous and hydrated fragments which show a much greater degree of chemical and mineralogical heterogeneity. Dramatic differences in mineralogy and reflectance spectra between fragments from cluster L2008#5 and L2005#31 are most likely due to the nature of parent bodies of these clusters; the anhydrous and mixed clusters are essentially heterogeneous breccias made up of different materials having different histories which were physically combined either in the early nebula or in the regolith of a parent body.

How do cluster particles differ from micrometeorites? Cluster IDPs are within the same size range (~50-100 µm in diameter) as smaller-sized Antarctic micrometeorites (MMs). In general, more than 50% of these MMs have been highly heated during atmospheric entry [14]. Approximately 6% of MMs with unmelted-looking surfaces have abundant magnetite and depleted bulk S (relative to CI) which suggests that they have been extensively heated. However, fragments from our cluster particles contain chondritic S and minor amounts of magnetite; they most closely resemble the relatively unheated, small-sized IDPs.

References: [1] Thomas K.L. *et al.* (1994) LPSC 25, 1393. [2] Thomas K.L. *et al.* (1994) LPSC 25, 1391. [3] Clemett S.J. *et al.* (1993) Science 262, 721. [4] McKeegan K.D. *et al.* (1985) GCA 49, 1971. [5] Thomas K.L. *et al.* (1993) GCA 57, 1551. [6] Bradley J.B. *et al.* (1994) LPSC 25, 159. [7] CDPET (1992) Cosmic Dust Catalog 13, 57. [8] Schramm L.S. *et al.* (1989) Meteoritics 24, 99. [9] Keller L.P. *et al.* (1992) LPSC 23, 675. [10] Nier A.O. and Schlutter D.S. (1993) Meteoritics 25, 675. [11] CDPET (1990) Cosmic Dust Catalog 11, 38. [12] Zolensky M.E. & Barrett R.A. (1994) Meteoritics 29, 616. [13] Nier A.O. and Schlutter D.J. (1992) Meteoritics 27, 166. [14] Kurat G. *et al.* (1992) LPSC 23, 747.

PRECEDING PAGE BLANK NOT FILMED

THE NATURE OF AGGLUTINITIC GLASS IN THE FINE-SIZE FRACTION OF LUNAR SOIL 10084.

Lindsay P. Keller¹ and David S. McKay², ¹MVA Inc., 5500 Oakbrook Parkway, Suite 200, Norcross, GA 30093 and ²SN, NASA-JSC, Houston, TX 77058.

Introduction. Agglutinitic glass contains much of the reduced Fe in lunar soils [1], and contributes to the modification of reflectance spectra from lunar soils [2]. Previous work has shown that agglutinitic glass can be compositionally heterogeneous [e.g. 3-5], but the scale of these heterogeneities is not well known. In addition, few data are available on the characteristics of the inclusions in agglutinitic glass. Here we report on our preliminary transmission electron microscope (TEM) examination of agglutinitic glass fragments from the Apollo 11 soil 10084.

Methods. Aliquots of the <20 μm size fraction of 10084 were embedded in low viscosity epoxy and specimens were prepared for electron microscope examination by ultramicrotomy. In the ultramicrotomed thin sections (80- to 100-nm thick), random fragments of agglutinitic glass free of lithic fragments were analyzed using a TEM equipped with an energy-dispersive x-ray (EDX) spectrometer. We analyzed 13 fragments of agglutinitic glass and collected 5 to 10 random analyses from each fragment (97 total analyses) using a probe size of ~ 100 nm. Thin-film EDX analyses were collected so that counting statistics for major elements were $\sim 1\%$; experimental k-factors have relative errors of $< 5\%$. The size distribution of submicroscopic Fe metal was determined for each analyzed area.

Results and Discussion. Agglutinitic glass in our samples shows large variations in composition and texture. To assess the heterogeneity within individual fragments, we plotted all the analyses from different regions within each fragment in plots of MgO/SiO_2 (wt.%) versus $\text{Al}_2\text{O}_3/\text{SiO}_2$ (wt.%). From these plots, three broad patterns are observed. **Group I.** The smallest group (3 of 13 fragments) random analyses within each fragment are tightly clustered about the composition of the $< 10 \mu\text{m}$ fraction of the bulk soil (Fig. 1a). These compositions are highly homogeneous over distances of several micrometers, and the size distribution and number density of Fe inclusions is very similar among fragments of this group. **Group II.** This group contains 5 of the 13 fragments and is characterized by linear mixing trends in x-y scatter plots (Fig. 1b). The mixing trends extend between an anorthite-rich component and a mafic component. These melts are not well-mixed. **Group III.** Agglutinitic glass in this group shows strong compositional and textural gradients on a scale of $< 0.1 \mu\text{m}$. The compositional variations are large and are not systematic. In only a few fragments have we identified domains within the agglutinitic glass that correspond to melts of individual minerals (5 regions of anorthite-composition glass and 1 region of augite glass were observed). Textural differences include the presence or absence of vesicles (and the number density of vesicles), the types of opaque inclusions, the size distribution of opaques, and the spatial distribution of opaques.

In agreement with previous studies, the average composition of our agglutinitic glass approaches that of the finest size fraction (Fig. 1e). We have however, observed that S is enriched by a factor of ~ 3 in agglutinitic glass relative to the bulk soil. Similar enrichments in S are observed in vapor-deposited coatings on mineral grains in the same soil [6], and so we believe that the S enrichment observed in agglutinitic glass is the preserved signature of the precursor materials, i.e. fine-grained soil grains with vapor coatings.

Opaque inclusions are typically spherical although most of the larger grains have begun to assume more euhedral shapes, including grains with octahedral faces and cubic forms. The number density of metal inclusions varies significantly among and within individual fragments of agglutinitic glass, however, the size distributions appear similar. Our results show that averaged over all analyzed agglutinitic glass fragments, the sizes of the metal inclusions follow a log-normal distribution (Fig. 1f) with a geometric mean grain size of 6.4 nm (the geometric standard deviation $\sigma_g = 1.81$). The measured size range of Fe grains closely corresponds to the proposed size range for the reduced metal that is known to be responsible for the ferromagnetic resonance (FMR) absorption used to estimate soil maturity [1]. The FMR data suggest a size range of ~ 4 - to 33-nm for the metal grains produced by the exposure-induced reduction of Fe^{2+} [1].

Conclusions. 1) Agglutinitic glass shows compositional and textural heterogeneities at the $0.1 \mu\text{m}$ scale. 2) The glass fragments preserve a component of vapor deposited material. 3) The number density of Fe inclusions in agglutinitic glass is highly variable, but in general the size distributions tend to be similar and follow a log-normal distribution. 4) The actual size range of Fe grains in agglutinitic glass is similar to that estimated by FMR.

References. [1] Morris, R. V. (1980) *PLPSC* 11, 1697. [2] Pieters, C. M. et al. (1993) *JGR* 98, 20817. [3] Hu, H-N and Taylor, L. A. (1978) *Mare Crisium: The View from Luna 24*, 291-302. [4] Walker, R. J. and Papike, J. J. (1981) *PLPSC* 12B, 421. [5] Basu, A. and McKay, D. S. (1985) *JGR* 90, D87. [6] Keller, L. P. and McKay, D. S. (1993) *Science* 261, 1305.

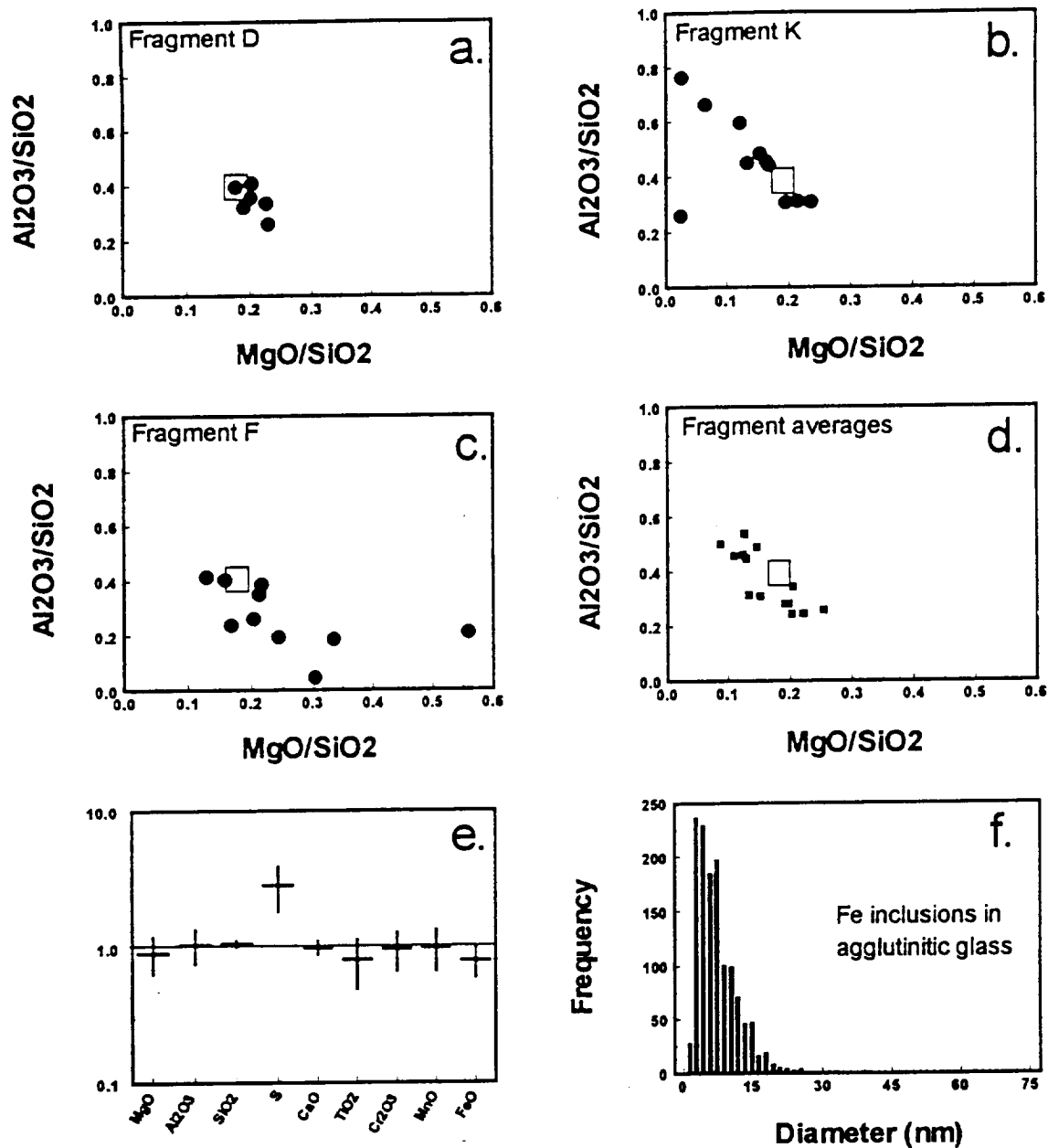


Figure 1a-1c. Plots of MgO/SiO_2 (wt.%) versus $\text{Al}_2\text{O}_3/\text{SiO}_2$ (wt.%) for individual fragments of agglutinitic glass showing a.) Group I, b.) Group II, and c.) Group III patterns (open square is the ratio for the $>10\ \mu\text{m}$ size fraction (from [4]), see text for details. Figure 1d shows the composition of each individual fragment obtained by combining the analyses from different regions within the same fragment to obtain an average. Figure 1e. The average composition of analyzed agglutinitic glass fragments relative to the bulk composition of the $>10\ \mu\text{m}$ size fraction (from [4]) of 10084. Figure 1f. A plot of the average size distribution of Fe grains in the analyzed agglutinitic glass fragments.

ELECTRON ENERGY-LOSS SPECTROSCOPY OF CARBON IN INTERPLANETARY DUST PARTICLES. Lindsay P. Keller¹, John P. Bradley¹, Kathie L. Thomas², and David S. McKay³, ¹MVA, Inc., 5500 Oakbrook Parkway, Norcross, GA 30093, ²C23, Lockheed, NASA/JSC, Houston, TX 77058, and ³SN, NASA/JSC, Houston, TX 77058

Introduction. The nature of the carbon-bearing phases in IDPs provides information regarding the chemical and physical processes involved in the formation and evolution of the early solar system. Several carbon-bearing materials have been observed in IDPs [e.g. 1], but details of their nature, abundance, and distribution are still poorly known. A knowledge of the abundance and nature of carbon in IDPs is useful in constraining the sources of IDPs and for comparisons with other chondritic materials. Estimates of carbon abundance in anhydrous and hydrated IDPs indicate that most of these particles have significantly higher carbon than the carbonaceous chondrites [2,3]. Mineralogical analyses show that carbonates are only a minor component of most hydrated IDPs, and so the high carbon abundances in this group of IDPs indicates that other carbon-bearing phases are present in significant concentrations [3]. Using the technique of electron energy-loss spectroscopy (EELS), we have identified two forms of carbon in a hydrated IDP, oxidized carbon (carbonates) and amorphous elemental carbon.

Methods. EELS spectra were obtained using a JEOL 2010 TEM equipped with a GATAN parallel EELS detector. Carbonate standards were finely ground and dispersed onto SiO thin films for the EELS analysis. Ultramicrotome thin sections (~80 nm thick) of IDPs were placed on holey carbon films and only those regions of the thin sections that were over holes in the film were analyzed. EELS spectra were acquired at 0.2 eV/channel, with an analysis time of 1 second/scan. The scanned spectra were summed until more than 50K photodiode counts in the carbon K-absorption edge were accumulated.

Carbon Near-edge structure. In amorphous carbon, the excitation of a 1s electron to the first empty band (the π^* conduction band) results in the onset of the carbon K-edge at ~284 eV. The broad peak in the EELS spectra at ~292 eV corresponds to transitions from 1s to the σ^* conduction band. In graphite, the π^* peak involves the pz orbitals (the weak bonds between planes of carbon atoms in the graphite structure), while the σ^* peak results from sp² hybrid bonds between coplanar carbon atoms. Structural variations (i.e. the degree of graphitization) can be estimated by comparing the relative proportions of π^* and σ^* bonding in the high-loss region [4,5].

There is a distinct energy shift in the onset of the carbon K-edge in carbonates relative to amorphous carbon. In carbonates, the onset of the carbon K-edge occurs at ~290 eV with a second broader peak centered at ~302 eV [6].

Results and Discussion. EELS spectra were collected from several regions (~0.5 μ m in diameter) in thin sections of L2006G1, a hydrated IDP that contains 20 wt.% C [3]. L2006G1 consists of abundant Mg-rich saponite that coexists with fine-grained Fe-Ni sulfides. Distinct grains of Mg-Fe carbonates are observed in the thin section. This IDP shows no mineralogical evidence of strong heating (e.g. a magnetite rim) even though the diameter of the particle is ~25 μ m.

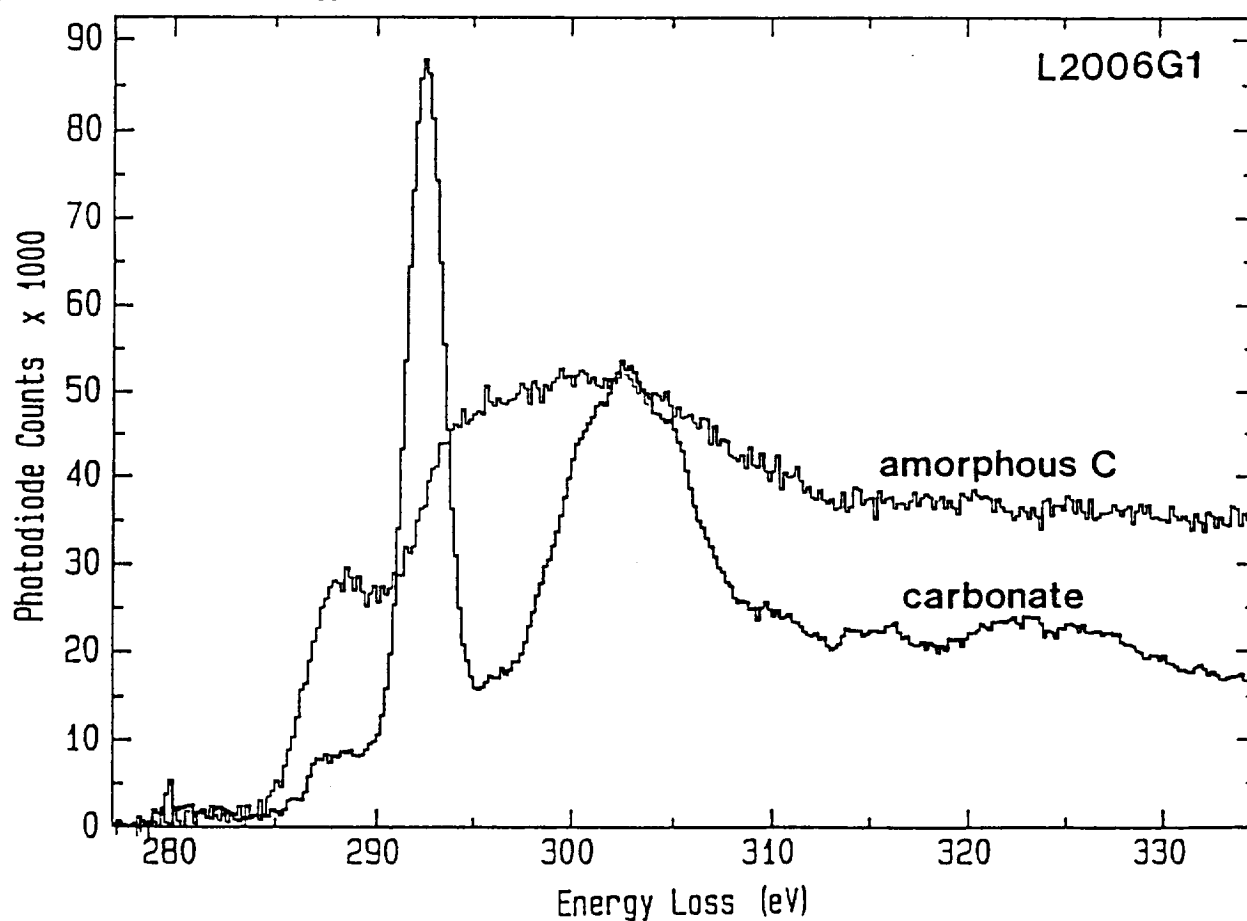
Typical EELS spectra from L2006G1 are shown in Figure 1. Spectra obtained from the carbonate grains show the characteristic doublet structure for oxidized carbon, however, they also exhibit a slight contribution from indigenous amorphous carbon (the small peak with an onset at 284 eV). EELS spectra from other areas in the thin sections (e.g. phyllosilicate-dominated regions) have carbon K-edges that are typical of amorphous carbon. Comparisons with the edge structure of the carbon support film suggest that the amorphous carbon in L2006G1 is more disordered than the holey carbon film.

Conclusions. The analysis of the carbon near-edge structure in the EELS spectra from a hydrated interplanetary dust particle shows that carbonates and amorphous elemental carbon are the major carbon-bearing phases. The carbonates occur as discrete grains in the IDP whereas the amorphous carbon is associated with the fine-grained phyllosilicates. Electron energy-loss spectroscopy in the TEM provides a means of mapping the chemical state of carbon in IDPs with high spatial resolution

Acknowledgements. This work was supported by NASA RTOPs 152-17-40-23 and 199-52-11-02, and MVA, Inc.

References. [1] Bradley, J. P. *et al.* (1988) Interplanetary Dust Particles. In *Meteorites and the Early Solar System*, 861-898. [2] Thomas, K. L., G. E. Blanford, L. P. Keller, W. Klöck and D. S. McKay (1993) *Geochimica et Cosmochimica Acta* **57**, 1551-1566. [3] Keller, L. P., Thomas, K. L., and McKay, D. S. (1993) *LPSC XXIV*, 785-786. [4] Miner, B. (1988) *Poorly Graphitized Kerogens: A High-Resolution TEM Study*. Ph.D Dissertation, Arizona State University. [5] Katrinak, K., Rez, P., and Buseck, P. R. (1992) *Environmental Science and Technology*, **26**, 1967-1976. [6] Smith, D. A., Clarke, D. R., Chisholm, M. F., Batson, P. E., and Olsson, E. (1990) *Proc. XII Intl. Cong. Electron Microscopy*, 32-33.

Figure 1. Electron energy-loss spectra of the main carbon-bearing phases in L2006G1.



PRECEDING PAGE BLANK NOT FILMED

ANATOMY OF A CLUSTER IDP (II): NOBLE GAS ABUNDANCES, TRACE ELEMENT GEOCHEMISTRY, ISOTOPIC ABUNDANCES, AND TRACE ORGANIC CHEMISTRY OF SEVERAL FRAGMENTS FROM L2008#5; K.L. Thomas¹, S. J. Clemett², G. J. Flynn³, L. P. Keller⁴, D. S. McKay⁵, S. Messenger⁶, A. O. Nier⁷, D.J. Schlutter⁷, S.R. Sutton⁸, R. M. Walker⁶, and R. N. Zare²; ¹Lockheed 2400 Nasa Rd. 1Houston, TX, 77058, ²Dept. of Chemistry, Stanford University, Stanford, CA 94305, ³Dept. of Physics, SUNY-Plattsburgh, Plattsburgh, NY 12901, ⁴MVA Inc., 5500/Suite 200 Oakbrook Pkwy., Norcross, GA 30093, ⁵NASA/JSC, SN, Houston, TX 77058, ⁶McDonnell Center for the Space Sciences, Physics Dept., Washington University, St. Louis, MO 63130, ⁷School of Physics and Astronomy, University of Minnesota, Minneapolis, MN 55455, ⁸Dept. of Geophysical Sciences, The University of Chicago, Chicago, IL 60637

In Part I, we described the bulk chemistry and mineralogy of large fragments and fines (<5 μm) from a cluster IDP originally ~ 40-50 μm in diameter [1]. Here we report results from several types of analyses: noble gas measurements (Nier), Synchrotron X-Ray Fluorescence (SXRF) for trace element abundances (Flynn and Sutton), ion probe studies (Messenger and Walker), and trace organic chemistry (Clemett and Zare). The same fragments were analyzed for isotopic abundances and organic compounds. **Noble Gas Content and Release Temperatures** He content and the He release temperatures for four samples were determined by step-heating experiments [2]. The average ⁴He abundance is ~4.1 (cc x 10¹¹) and extraction temperatures for removal of 50% of the He range from 750-1040 °C, with an average at 928 °C (Table 1). The low He content and high release temperatures indicate that all fragments from L2008#5 have experienced heating during atmospheric entry. He measurements have been used to distinguish asteroidal from cometary IDPs in individual, small-sized particles (< 10 μm in diameter) [3]; however these measurements cannot be used to determine sources of cluster particles because higher deceleration heating occurs in large-size particles.

Trace Element Abundances SXRF was used to determine trace element abundances in four fragments from L2008#5 [technique described in 4]. Two fragments show marked depletions in Zn (Zn/Fe < 0.1) indicating they have experienced heating during atmospheric entry (Table 2). Zn/Fe ratios range from 0.2-0.5 for the remaining fragments. All four fragments show deviations by more than a factor of 2 from CI for 3 or more elements (Table 2). The only consistent trends are enrichments in Cu, Se, and Br, and a depletion in Zn relative to CI.

Heating Summary of Cluster Fragments He content and release temperatures of fines suggest they experienced atmospheric entry heating. The large range in 50% He release temperatures suggests that fragments have not been heated equally. Low Zn/Fe ratios show that 2 of 4 fragments were heated during atmospheric entry. Previous TEM studies have shown that the presence of magnetite rims on IDP surfaces is an indication of atmospheric entry heating [e.g., 5]. Magnetite rims were observed in 13 of 20 fragments and fines from this cluster[1]. The He measurements indicate that cluster L2008#5 has not been uniformly heated; trace element abundances and magnetite rims are evidence that heating is seen in selected fragments, probably those located on the exterior surfaces of the cluster.

Isotopic Measurements D/H ratios of eight fragments were measured using an ion microprobe [technique described in 6]. Deuterium enrichments (δD) were observed in all four of the C-rich fragments and range from +322- +822 per mil. Four fragments from Clu37, which had a chondritic C abundance, showed no D enrichment (Table 3). The D enrichments in the C-rich fragments are far in excess of values for terrestrial samples and are another indication that the fragments are extraterrestrial [6]. There is an apparent positive correlation of D enrichment with the abundance of carbonaceous material in our fragments. A larger group of IDPs should be examined to confirm this result.

Trace Organic Chemistry The signatures of polycyclic aromatic hydrocarbons (PAHs) in IDPs have been observed with a microprobe two-step laser mass spectrometer ($\mu\text{L}^2\text{MS}$) [7]. All cluster fragments which had been analyzed previously for isotopic abundances were examined for the presence of PAHs (Table 3).

Anatomy of a Cluster IDP (II): Thomas K.L. *et al.*

All PAH signatures observed show significant variability between different particles. In fact, intensities of PAH signatures varied in pieces from the same fragments (e.g., Clu19 and Clu37, Table 3). For example, a strong PAH signature was observed in Clu19(β), while essentially no signal was found in Clu19(α) (Table 3). The PAH spectra from all fragments are very different from those of two other unrelated IDPs, Aurelian or Florianus [7]: the range of aromatic species observed is reduced (limited from 1 to 6 ring species) although individual peak intensities (e.g., naphthalene and the alkyl-phrenathrenes) are in some cases more intense than the most intense peak observed from Aurelian. The spectra are dominated by even mass PAHs with little evidence for odd mass peaks, suggestive of nitrogen substituted aromatic species. Although the distribution of PAHs may be affected by previous exposure to the ion probe (10keV Cs⁺ ions), strong PAHs signatures have only been observed in D-rich particles [this work & 7]. PAHs and elemental carbon coexist in some fragments of this cluster; however, there is a lack of correlation in the abundance of C and the presence of PAHs. Considering the mass of the entire cluster, PAHs and elemental carbon are not homogeneously distributed.

In summary, analyses of fragments from one cluster IDP show large variations in He content, He release temperatures, trace element and isotopic abundances, and the presence of organic components.

References: [1] Thomas K.L. *et al.* (1994) This volume. [2] Nier A.O. and Schlutter D.J. (1993) *Meteoritics* 25, 675. [3] Brownlee D.E. *et al.* (1993) *LPSC* 24, 205. [4] Flynn G.J. and Sutton S.R. (1991) *Proc. LPSC* 21, 549. [5] Keller L.P. *et al.* (1992) *LPSC* 23, 675. [6] McKeegan K.D. *et al.* (1985) *GCA* 49, 1971. [7] Clemett S.J. *et al.* (1993) *Science* 262, 721.

Table 1. He measurements of fines from cluster L2008#5.

Sample #	⁴ He (cc x 10 ¹¹)	50% He Release Temp (°C)	³ He/ ⁴ He (x10 ⁻⁴)	²⁰ Ne/ ²² Ne	⁴ He/ ²⁰ Ne
1	4.5	750	3.3 +/- 0.7	13.3 +/- 1.6	9.9 +/- 0.4
2	6.1	1040	4.7 +/- 0.5	11.5 +/- 1.3	14.3 +/- 1.0
3	3.4	1010	7.2 +/- 1.2	7.2 +/- 1.0	12.0 +/- 3.0
4	2.2	910	5.9 +/- 1.4	10.5 +/- 1.7	6.8 +/- 1.0

Table 2. SXRF trace element abundances normalized to CI of 4 large fragments from L2008#5.

Sample #	Cr	Mn	Fe*	Ni	Cu	Zn	Ga	Ge	Se	Br	Zn/Fe
Clu16	0.2	0.4	1.4	2.0	3.5	0.06	0.4	0.2	6.1	2.0	0.04
Clu18	1.3	1.8	1.3	0.5	1.7	0.06	7.1	0.3	1.8	7.3	0.05
Clu21	0.4	3.1	2.1	2.0	7.4	0.44	1.4	0.6	3.4	7.3	0.2
Clu319	3.5	0.2	1.1	0.9	2.6	0.52	10.0	2.8	5.4	24.8	0.5

*Values from EDS

Table 3. Carbon abundance (Wt.%), Deuterium enrichments (δ D), and the presence of PAHs signatures in several large fragments from cluster L2008#5.

Sample	Wt.% Carbon (EDS)	δ D (per mil)*	μ L ² MS (%) **
Clu19(α)‡	a+b=14	+664 +/- 84	>5
Clu19(β)‡	"	+424 +/- 71	100
Clu110	10	+822 +/- 91	43
Clu313†	15	+322 +/- 67	Not measured
Clu37(α)§	a+b+c+d=3	-24 +/- 17	20
Clu37(β)§	"	+25 +/- 22	7
Clu37(χ)§	"	-14 +/- 36	32
Clu37(δ)§	"	+12 +/- 29	13

*Terrestrial range is -200 - +50 per mil **Integrated signal intensity from 80-450 amu normalized relative to

Clu19(β) ‡ Clu19 broke into 2 separate pieces (α & β) † 3 μ m fragment, possibly too small for PAHs analysis

§ Clu37 fractured into 4 pieces (α , β , χ , δ)

THE ANATOMY OF A CLUSTER IDP (I): CARBON ABUNDANCE, BULK CHEMISTRY AND MINERALOGY OF FRAGMENTS FROM L2008#5; K.L. Thomas¹, L.P. Keller², W. Klock³, J. Warren¹, G.E. Blanford⁴, and D.S. McKay⁵ ¹Lockheed, 2400 Nasa Rd.1 Houston, TX, 77058, ²MVA Inc., 5500/Suite 200 Oakbrook Pkwy, Norcross, GA 30093 ³Institute fur Planetologie, Wilhelm-Klemm-Str.10, 4400 Munster, Germany, ⁴University of Houston, Clear-Lake, Houston, TX 77058, ⁵NASA/JSC, SN, Houston, TX 77058.

Chondritic anhydrous interplanetary dust particles (IDPs) are among the most pristine solar system materials known, and despite their small size, have been intensely studied. Multidisciplinary studies of IDPs have traditionally been restricted to cluster particles, where individual fragments of the same cluster are allocated to several researchers. In this manner, different analyses can be performed on essentially the same material, assuming that individual fragments are representative of the whole cluster. Our preliminary work, however, indicated that fragments from cluster particles can show mineralogical and chemical heterogeneities at the 10 μm scale [1].

The objective of this study was to determine whether or not cluster particles are sufficiently homogeneous to enable observations from one fragment of the cluster to be extrapolated to the entire cluster. Here we report on the results of a consortium study of the fragments of a large cluster particle. Multiple fragments from one large cluster were distributed to several research groups and were subjected to a variety of mineralogical and chemical analyses including: SEM, TEM, ion probe, SXRF, noble gas measurements, and microprobe laser mass spectrometry of individual fragments. The mineralogy and bulk chemistry of the cluster fragments are discussed below and the trace element geochemistry, isotopic data, and other results are given in a companion abstract [2].

Methods We were allocated ~95% of the fragments from cluster L2008#5 (originally ~40-50 μm in diameter), which contained many large fragments and fines: three fragments are ~15 x 15 μm , six are ~12 x 12 μm , 30-40 range from 5-10 μm in diameter, and many fragments (called fines) were <5 μm in diameter. We have determined bulk compositions for elements with $Z > 5$ of 53 particles from one large cluster. Our procedures and extensive analytical checks for quantitative SEM EDX light element analysis are described in detail elsewhere [3]. Following the chemical analysis, several of the particles were embedded in epoxy, thin sectioned using an ultramicrotome, and examined in the TEM.

Chemistry We analyzed 53 fragments from cluster L2008#5 for major, minor, and light elements (carbon and oxygen). The cluster average and major element ranges for all fragments are shown in Fig. 1. The average element abundances were found to be chondritic (within 2xCI) for L2008#5 with the exception of Na and P which were ~4xCI and 5xCI, respectively. Large ranges for major elements C, Si, Mg, S, Fe, and O suggest that compositional differences exist (Fig. 1). Only 24 (45%) of the analyzed fragments have the "same" composition for major elements (C, O, Mg, Si, S, Fe) within one standard deviation. Of the 29 remaining fragments, 31% have significantly higher Fe or Fe and S with lower O; 17% have significantly higher C.

Mineralogy Table 1 lists mineral assemblages found in large fragments and fines from cluster L2008#5. Fragments have been classified according to the most abundant mineral phase. A variety of mineral phases are present in this cluster particle and minerals with similar compositional ranges are found in large fragments and fines. For example, olivine compositions range from Fo 57-99 in large fragments and from Fo 66-98 in fines. However, several olivine-dominated fragments have very narrow ranges of olivine compositions which differ from one fragment to another. Pyroxenes range in composition from enstatite to those high in Ca. Amorphous material, such as glass and carbonaceous material, is present in some fragments. Glass compositions range from Si-rich to feldspathic with minor amounts of Mg and Fe occasionally present; glass regions can have either a smooth or a vesicular texture. Amorphous, C-rich material is observed in particles with C > 3xCI (~11 wt.% C). Mineral grain sizes vary from fragment to fragment: some fragments are predominantly coarse-grained (μm in diameter), some are predominantly fine-grained (<50 nm in diameter) and

some contain a mixture of coarse and fine grains. Partial magnetite rims are present on some fragments, indicating they were heated during atmospheric entry [4]. The relative range of mineral abundances in the large fragments is also duplicated in the fines.

Discussion Cluster L2008#5 is composed mainly of chondritic (within $\sim 2 \times$ CI) fragments that differ significantly in mineralogy (Table 1). Non-chondritic fragments (e.g., those dominated by sulfides or magnetite) make up 25% of this cluster. A representative sampling of material from the cluster for mineralogical and chemical analyses would require analyses of a minimum of four large fragments. Attempts to extrapolate analyses from one fragment to an entire cluster will be misleading if all cluster particles show similar levels of heterogeneity as L2008#5.

References: [1] Thomas K.L. *et al.* (1993) *Meteoritics* 28, 448. [2] Thomas K.L. *et al.* (1994) This volume. [3] Thomas K.L. *et al.* (1993) *GCA* 57, 1551. [4] Keller L.P. *et al.* (1992) *LPSC* 23, 675.

Figure 1. Mean values and range of element abundances for 53 fragments from cluster L2008#5. Chemical heterogeneity of fragments is shown by the ranges for major elements (bars); mean values are represented by lines located to the right of the bars.

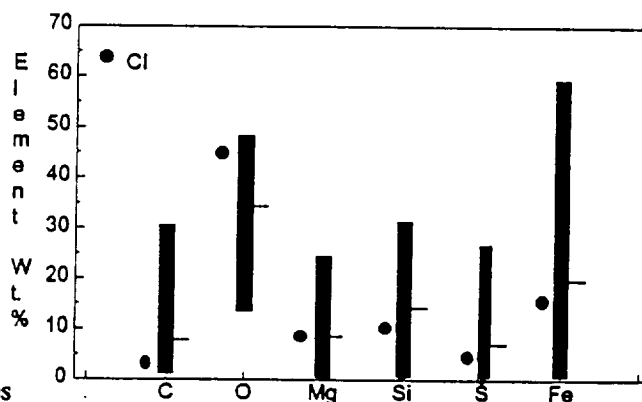


Table 1. Mineralogy of 10 large fragments and fines from cluster L2008#5. Fragments have been classified according to the most abundant mineral phase. Ranges of mineral compositions are given for each group (e.g., olivine-dominated) as a whole, but some individual fragments have narrow ranges of mineral compositions.

Fragments (> 5 μm)	Fines (< 5 μm)
Olivine-Dominated (4 fragments) * Fo 57-84, Glass, Enstatite, high Ca pyroxene, Fe-sulfide with Ni; 3 have magnetite rims. Coarse, fine, and mixed grain sizes.	Olivine-Dominated (3 fragments) * Fo 78-86, Glass, Enstatite, high Ca pyroxene, Fe-sulfide with Ni; all have magnetite rims. Mostly coarse and mixed grain sizes.
Pyroxene-Dominated (3 fragments) * Enstatite, glass, few Fo 88-95, Fe-sulfide with Ni, Carbonaceous material; 2 have magnetite rims. Mostly fine and mixed grain sizes.	Pyroxene-Dominated (2 fragments) * Enstatite, glass, high Ca pyroxene, Fe-sulfide with Ni; all have magnetite rims. Coarse and fine grain sizes.
FGA (Fine-grain aggregate) Dominated (1 fragment) * Fine-grain aggregates, Fo 79-99, enstatite, glass, Abundant Fe-sulfides with Ni; magnetite rim. Fine grain sizes.	Olivine-Pyroxene Mix (1 fragment) * Fo 66, Glass, Enstatite, few fine-grain aggregates; Magnetite rim, mixed grain sizes.
Others (2 fragments) * Large Fe-sulfide, few Fo 65-76, No magnetite rim, coarse grain sizes. * Large magnetite grain, few Fe-sulfides with Ni, Si-rich glass; magnetite rim, coarse grain sizes.	FGA Dominated (1 fragment) * Fine-grain aggregates, Fo 98, Enstatite, Augite, Fe-sulfide; no magnetite rim, fine grain sizes.
	Others (3 fragments) * 2 Large magnetites, Fo-68-91, few Fe-sulfides with Ni, 1 has lg. kamacite; no magnetite rims, coarse grain sizes. * Large Fe-sulfide with Ni, glass, kamacite, ferrihydrite; magnetite rim, coarse grain sizes.

HYDRATED CLUSTER PARTICLES: CHEMICAL AND MINERALOGICAL ANALYSES OF FRAGMENTS FROM TWO INTERPLANETARY DUST PARTICLES; K.L. Thomas¹, L.P. Keller², S.J. Clemett³, D.S. McKay⁴, S. Messenger⁵, and R.N. Zare³; ¹Lockheed, C23, Nasa Rd. 1 Houston, TX 77058, ²Dept. of Chemistry, Stanford University, Stanford, CA 94305, ³MVA Inc., 5500/Suite 200, Oakbrook Pkwy., Norcross, GA 30093, ⁴NASA/JSC SN, Houston, TX 77058, ⁵McDonnell Center for Space Sciences, Physics Dept., Washington University, St.Louis, MO 63130

Chondritic interplanetary dust particles (IDPs) are among the most pristine solar system materials known, yet despite their small size they have been intensely studied. Our previous work on 53 fragments from one *anhydrous* cluster IDP (L2008 #5) showed that the individual fragments display strong chemical and mineralogical heterogeneity [1,2]. We are currently extending our studies of cluster particles to those consisting primarily of *hydrated* fragments in order to compare their chemical and mineralogical heterogeneity to anhydrous cluster particles, micrometeorites, and fine-grained chondrite matrix.

Five fragments for each of two cluster particles were analyzed in consortium mode as in our previous study [1,2]. All fragments from each cluster were distributed to several research groups and subjected to a variety of analyses including: SEM, TEM, ion microprobe, microprobe laser mass spectrometry, and reflectance spectroscopy. Laser mass spectrometry [3] and ion microprobe[4] measurements on some fragments are in progress.

Methods We were allocated 5 fragments from 2 cluster particles, L2011#5 and L2005#31, for a total of 10 IDPs. All fragments were >5 micrometers in diameter. We determined the bulk composition for elements with $Z > 5$ of all 10 fragments. Our procedures and analytical checks for quantitative SEM EDX light element analysis are described in detail elsewhere [5]. Following the chemical analyses, all particles were analyzed using reflectance spectroscopy [technique described in 6]. Six IDPs, three from each cluster, were embedded in epoxy, thin sectioned using an ultramicrotome, and examined in the TEM. The 4 remaining fragments were analyzed for polycyclic aromatic hydrocarbon signatures and for D/H ratios using an ion microprobe.

Results One related fragment from our first cluster, L2011#5, is documented in the JSC Cosmic Dust Catalog [7]. This fragment, L2011B1, has a chondritic spectra with a low bulk Ca content and a smooth surface morphology, two typical characteristics of hydrated IDPs [8]. In general, our five fragments from cluster L2011#5 have chondritic compositions for all major elements. The three fragments analyzed in the TEM are composed predominantly (>50% by volume) of serpentine (0.7 nm basal spacing). Only one fragment contains anhydrous silicates; olivines are Fo ~99-100 and no pyroxenes are observed. Phyllosilicates are both coarse and fine-grained in all fragments. Fe-Ni sulfides are ubiquitous in the fine-grained serpentine; Ni contents range from ~0.5-42 wt.%.

Reflectance spectra were obtained for each of the fragments over the range of 380-800 nm. Three fragments are indistinguishable and show typical flat C-type spectra.

Heating History of Our First Cluster Distinct magnetite rims were located on the exterior surfaces of one fragment. In all three fragments, discrete regions of serpentine located at the outer edge had a vesicular texture. Magnetite rims result from atmospheric entry heating [9] and we believe that the vesicular serpentine on the particle surfaces also forms during atmospheric entry either through volatilization of solar wind implanted gases or through dehydroxylation of serpentine. One related fragment, L2011B5, was analyzed for noble gas content and He release temperature [10]. The ⁴He abundance was low in this IDP (2.3 cm³STP/gx10³). The 50% He release temperature was 550 °C which indicates that this fragment experienced only mild heating during atmospheric entry.

Vapor Deposits in the Lunar Regolith

L. P. Keller and D. S. McKay (1) present direct evidence, obtained by transmission electron microscopy, that widespread coatings were formed by deposition of impact-generated vapor on lunar regolith particles. Since the Apollo missions, we have emphasized the following points, which are based on theoretical calculations and on laboratory studies of the properties of evaporated silicate deposits and of lunar samples (2). (i) The mass of vapor generated by impacts on the lunar surface is comparable in magnitude to the mass of impact melt glasses; (ii) the physics of impact into a porous regolith requires that much of this vapor be retained in the soil rather than lost to space (as is widely believed); (iii) experimental coatings made from vaporized or sputtered lunar basalt contain abundant inclusions of submicroscopic, superparamagnetic metallic Fe; and (iv) this Fe may explain the magnetic signature, low albedo, reddened spectrum, and subdued absorption bands of lunar regolith.

Our conclusions have been generally rejected by the lunar geochemical community for two reasons: (i) there seemed to be no direct evidence for vapor deposits in Apollo samples (3), and (ii) it seemed that the lunar optical properties could be explained by the presence of impact melt glasses alone (4). However, advances in our understanding of the optical properties of glasses (5) and of light scattering by planetary regoliths (6), and now the direct detection of vapor deposits (1), show that these objections are not valid. Vapor phase transport is a major process on the lunar surface, and unless its effects are taken into account, the chemical, magnetic, and optical properties of the regolith cannot be understood.

Bruce Hapke
William Cassidy

Department of Geology and Planetary Science,
University of Pittsburgh,
Pittsburgh, PA 15260, USA

Eddie Wells
Space Telescope Science Institute,
Astronomy Programs,
Computer Science Corporation,
3700 San Martin Drive,
Baltimore, MD 21218, USA

REFERENCES AND NOTES

1. L. P. Keller and D. S. McKay, *Science* **261**, 1305 (1993).
2. B. Hapke, *Moon* **7**, 342 (1973); W. Cassidy and B. Hapke, *Icarus* **25**, 371 (1975); B. Hapke, W. Cassidy, E. Wells, *Moon* **13**, 339 (1975); B. Hapke, *Phys. Earth Planet. Inter.* **15**, 264 (1977); R. Baron et al., *Earth Planet. Sci. Lett.* **37**, 263 (1977); B. Hapke, in *Abstracts, 8th Lunar Science*

Conference (Lunar and Planetary Institute, Houston, TX, 1977), part 1, p. 398.

3. As recently as last year, M. Cintala [*J. Geophys. Res.* **97**, 947 (1992)] argued that vapor deposits in the lunar regolith were either nonexistent or were so thin that their optical effects were negligible.
4. J. Cone and D. Nash, in *Proceedings of the Apollo 11 Lunar Science Conference*, A. Levinson, Ed. (Pergamon, New York, 1970), p. 2013; J. Adams and T. McCord, in *Proceedings of the 2nd Lunar Science Conference*, A. Levinson, Ed. (MIT Press, Cambridge, MA, 1971), p. 2138.
5. E. Wells and B. Hapke, *Science* **195**, 977 (1977).
6. B. Hapke, *Theory of Reflectance and Emittance Spectroscopy* (Cambridge Univ. Press, New York, 1993).

18 October 1993; accepted 24 November 1993

Keller and McKay conclude (1) that the amorphous rims of approximately 500 Å on lunar dust grains are largely a result of impact-produced vapor deposits. This contrasts with previous work by Bibring et al. (2), who concluded that these rims result from solar wind (SW) ion damage. Keller and McKay base their conclusion on the observation of compositional differences between the rims and grain interiors of silicates. Setting aside for the moment the question of whether such compositional variation can also occur within a radiation damage model, a crucial test of the lunar vapor scenario should be provided by lunar soil ilmenite (not studied by Keller and McKay in their report), because it is compositionally distinct from silicates and is only a minor lunar soil component. Because vapor deposition and SW ion implantation affect all lunar soil grains, if the vapor deposit model is correct, it follows that any amorphous rims on ilmenite (FeTiO₃) grains must also be dominantly silicate vapor deposits. Alternatively, because ilmenites are more resistant to radiation damage than are silicates (2), if SW ion damage is important for ilmenites, it is at least equally important for silicates.

We have recently performed rare gas studies (3) of seven ilmenite grains (~100 µm) from the submature lunar soil 71501 that were partially microtomed for transmission electron microscopy (TEM) observation. All of the grains had SW rare gases and disordered rims with chemical compositions similar to those of the host ilmenite. Furthermore, the rare gas extractions from individual lunar ilmenite grains (3) yielded lower limits on SW He fluences to which grains from this soil were subjected. The measured values of up to 5×10^{-3} He ccSTP per square centimeter correspond to an equivalent flat target fluence of about 10^{17} He per square centimeter. Simulation experiments (2) showed that this fluence is

large enough to produce severe radiation damage in ilmenite, as observed. The ilmenite surfaces are also contaminated by vapor deposits, as evidenced by enrichments in Mg, Al, Si, S, and Ca. The dominant vapor deposit species is Si, with an atomic abundance, however, that averages only 20% of that of Ti in the outer few hundred angstroms of the ilmenite grains. The disordered rims cannot, therefore, be pure vapor deposits, as advocated by Keller and McKay. Instead, they must represent SW-damaged layers with a composition that has been affected to only a limited extent by vapor contamination.

The marked rounding of rimmed silicate grains, observed by Keller and McKay (1), cannot be ascribed to vapor deposition because the amorphous rims and the material beneath them are rounded. This rounding reflects an efficient erosion process that can be triggered by SW ion sputtering ($E \approx 1$ keV/amu), but not by the "impact" of lunar vapor with a much lower energy (≈ 0.1 eV/amu). Simulation experiments of SW (2), which indicate that silicates are about ten times more sensitive to damage and sputtering than ilmenite, reproduce this rounding and "coating" effect. The critical fluence of SW ions needed to form amorphous rims on lunar silicates is two to three times smaller than the critical fluence required to round off their edges. Consequently, the well-rounded feldspars depicted in the report by Keller and McKay (1) necessarily contain a SW ion damage layer.

Other observations support the dominance of SW radiation damaged layers. First, the quantity of SW rare gases retained depends on the nature of the lunar mineral, with ilmenite being the most retentive (4). Thus, these gases cannot be implanted in silicate vapor deposits on ilmenite, consistent with our TEM observations. Second, thermal annealing experiments (2) indicate that the approximately 500 Å amorphous rims on lunar silicates anneal at the same temperature ($\approx 800^\circ\text{C}$) as the fossil nuclear tracks registered in the same grains. The same annealing conditions were noted for damage layers of about 500 Å obtained with artificial SW. In contrast, artificial feldspar vapor deposits on silicates start recrystallizing at very low temperatures ($\approx 300^\circ\text{C}$) and flake off at about 500°C (5). Thus, annealing experiments also indicate a radiation damage origin for the lunar amorphous coatings.

Our observations confirm that vapor deposits do alter the composition of lunar grain surfaces, but they also show that disordered rims on lunar grains must be largely ascribed to radiation damage. Moreover, unlike Keller and McKay, we do not expect that the composition of the SW damage layer will strictly match the com-

position of its host minerals because "recoil mixing" (6) can deplete this layer in light elements and especially because the SW damage layer on silicates is extremely reactive. For example, Dran *et al.* (7) showed that hydration rates can be up to 10^3 times higher than that of the undamaged mineral. Concomitant ejection of alkali metal ions in silicates loaded with SW-implanted hydrogen could, for example, provide an explanation for the alkali metal depletion in the lunar silicate rims observed by Keller and McKay (1).

T. J. Bernatowicz
R. H. Nichols Jr.
C. M. Hohenberg

McDonnell Center for the Space Sciences,
Washington University,
St. Louis, MO 63130, USA
M. Maurette
Centre de Spectrometrie Nucleaire
et de Spectrometrie de Masse,
91405 Orsay Campus, Orsay, France

REFERENCES

1. L. P. Keller and D. S. McKay, *Science* 261, 1305 (1993).
2. J. P. Bibring *et al.*, *Earth Planet. Sci. Lett.* 22, 205 (1974).
3. R. H. Nichols Jr. *et al.*, *Geochim. Cosmochim. Acta* 58, 1031 (1994); T. J. Bernatowicz *et al.*, *Lunar Planet. Sci. Conf.* 25, 105 (abstr.) (1994).
4. H. Ducati *et al.*, *Moon* 8, 210 (1973).
5. J. P. Bibring *et al.*, *Geochim. Cosmochim. Acta* 2 (suppl. 5), 1763 (1974).
6. P. Sigmund, *J. Appl. Phys.* 50, 7261 (1979); R. Kelly, I. Bertoni, A. Miotello, *Nucl. Instrum. Methods* 880, 1154 (1993).
7. J. C. Dran, Y. Langevin, J. C. Petit, *Nucl. Instrum. Methods* B1, 557 (1984).

16 December 1993; accepted 6 April 1994

Response: Bernatowicz *et al.* do not present the same analyses on silicates as they do on ilmenites. They apparently assume that ilmenite behaves similarly to the silicates present in lunar soils—for example, that ilmenite acquires and retains vapor deposits with the same efficiency as do silicate grains. Christoffersen *et al.* (1), however, have shown that the surfaces of ilmenite grains are reactive in the lunar soil environment. Several processes operating in the lunar regolith serve to modify the surfaces of ilmenite grains, including the implantation of solar wind ions, in situ reduction, and vapor deposition. Christoffersen *et al.* showed that most ilmenite grains in their samples contained outer rims of up to 120 nm thick, where the host ilmenite had decomposed into a mixture of Fe metal and

Table 1. Average compositions of amorphous rims on specific minerals in lunar soils 10084 and 78221 (in weight %)

Host mineral	Na ₂ O	MgO	Al ₂ O ₃	SiO ₂	S	CaO	TiO ₂	FeO
Anorthite	0.1	3.5	20.1	53.4	0.7	9.7	4.0	9.5
Cristobalite	0.2	5.4	11.5	59.2	1.7	7.3	3.9	10.8
Olivine	0.6	8.8	15.5	47.6	0.4	8.8	3.6	14.7

Ti-oxide grains. These reaction rims correspond to the "disordered" rims observed by Bernatowicz *et al.* (2) and are distinguished from their hosts by their microstructure and composition; all of the reaction rims analyzed are nanocrystalline (not amorphous) and show strong depletions in Fe (up to a 40% depletion of Fe relative to stoichiometric ilmenite). This Fe depletion cannot be the result of direct solar wind sputtering (for example, knock-on and ejection of Fe atoms) of ilmenite because such sputtering is essentially a surface phenomenon that removes surface atoms in proportion to their abundance (notwithstanding the outermost few nanometers where preferential sputtering may occur). Nor can it be ascribed to sputter deposition, because deposits formed by sputtering would be enriched in Fe, not depleted. The reaction rims probably result from the interaction of solar wind hydrogen with ilmenite, either directly during implantation or through subsequent heating of the ilmenite grains (1). This interaction would result in the reduction of Fe²⁺ to Fe⁰, migration of Fe⁰ to the grain surface, and loss of Fe⁰ by vaporization. Thus, the surfaces of ilmenite grains are dynamic; they suffer significant mass loss and volume reduction. These data indicate that ilmenite should be avoided, not sought, as a test of the vapor deposition model, because ilmenite appears to be chemically reactive with solar wind hydrogen and this reaction greatly complicates the outer rims, obscuring other effects.

The only truly amorphous material on the surfaces of the ilmenite grains is a thin rind of silicate material that is superimposed on the reaction rim. We agree that some proportion of the Na and K depletion observed in the rims might be accounted for by sputtering, as demonstrated experimentally by Hapke *et al.* (3). However, "recoil-mixing" cannot account for the gross chemical differences between most rims and their hosts. Rims on cristobalite (essentially pure SiO₂) contain major Mg, Al, Ca, Ti, and

Fe (Table 1); these elements are foreign to cristobalite and so must have been deposited on the surfaces of grains by condensation of impact-derived vapors or by sputter deposition. Similar arguments can be made for the amorphous rims on olivine [(Mg,Fe)₂SiO₄] grains, which contain major amounts of Ca, Al, and Ti (elements that are normally present in olivine at only trace amounts), and for rims on anorthite (An₉₅₋₉₉), which contains major Mg, Ti, and Fe (which are also present in trace concentrations in the host plagioclase). Overall, the average rim compositions are remarkably similar and are independent of the host grain mineralogy (Table 1). These data indicate that much of the "thickness" of amorphous rims consists of elements that are not indigenous to the host soil grains.

Whether there are "sputtering" or radiation effects superimposed on the vapor deposited material can be debated. We do not explicitly exclude the effects of radiation damage as a contributing factor to the formation of amorphous rims; we merely emphasize the major (and generally overlooked) role played by condensed vapors in the formation of amorphous rims on lunar soil grains.

Lindsay P. Keller
MVA, Inc.,

5500 Oakbrook Parkway, Suite 200,
Norcross, GA 30093, USA

David S. McKay
Code SN,

National Aeronautics and Space
Administration,

Johnson Space Center,
Houston, TX 77058, USA

REFERENCES

1. R. Christoffersen *et al.*, *Lunar Planet. Sci. Conf.* 25, 259 (1994).
2. T. J. Bernatowicz *et al.*, *ibid.* (abstr.), p. 105.
3. B. Hapke, W. Cassidy, E. Wells, *Moon* 13, 339 (1975).

23 February 1994; accepted 6 April 1994

THE NATURE OF CARBON-BEARING PHASES IN HYDRATED INTERPLANETARY DUST PARTICLES.

Lindsay P. Keller¹, Kathie L. Thomas², and David S. McKay³, ¹MVA Inc., 5500/200 Oakbrook Parkway, Norcross, GA 30093, ²C23, Lockheed, NASA Johnson Space Center, Houston, TX 77058, and ³SN6, NASA Johnson Space Center, Houston, TX 77058.

We have been quantitatively measuring carbon abundances in hydrated interplanetary dust particles for the past few years, but in general, we have had to infer the distribution and nature of the carbon-bearing materials within these particles because of the complex microtextures of hydrated IDPs. Aside from rare carbonate grains, other carbon-bearing phases are difficult to distinguish from the fine-grained, poorly-crystalline phyllosilicates that comprise the bulk of these particles. We know that carbonates alone cannot account for the high carbon abundances observed in most hydrated IDPs and that additional carbon-bearing phases must be present [1]. We have recently applied the technique of electron energy-loss spectroscopy (EELS) in the transmission electron microscope (TEM) to identify the form and distribution of carbon-bearing phases in hydrated IDPs [2]. These preliminary data show that several carbon-rich hydrated IDPs contain a mixture of two major forms of carbon, Mg-Fe carbonate and amorphous carbon.

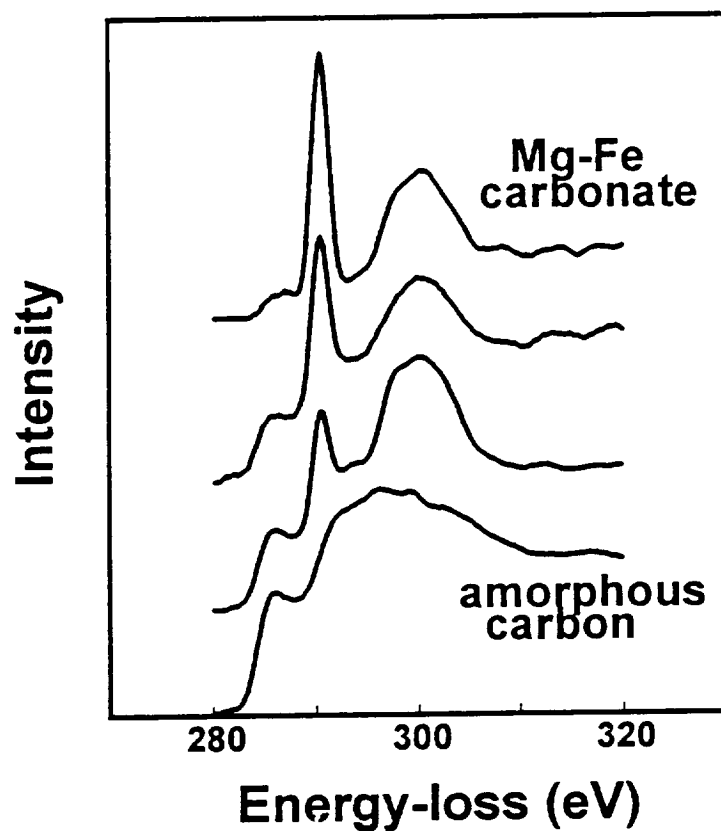
The EELS technique is used to measure the energy lost by electrons through inelastic scattering in the sample. Characteristic edge structure results from the promotion of inner shell electrons to valence and conduction bands and provides information on the local structure and bonding (Figure 1). We analyzed ultramicrotome thin sections of four hydrated IDPs using a parallel energy-loss spectrometer. The IDPs include L2005R7, L2006E10, L2006F10, and L2006G1 which have bulk carbon contents of 9, 11, 15, and 20 wt.%, respectively [1]. The analysis of the carbon k-edges in EELS spectra shows that all four IDPs contain amorphous carbon as the major carbon-bearing phase, G1 and F10 contain abundant Mg-Fe carbonates, R7 contains minor carbonate (detected only by EELS), and E10 is devoid of carbonates.

The near-edge structure in the carbon k-edges from these IDPs shows no evidence for the development of graphite or even poorly-graphitized carbon (Figure 1). We conclude that the "elemental" carbon in these IDPs is either very poorly ordered or is exceedingly fine-grained (we refer to this carbon as "amorphous carbon"). The amorphous carbon is intimately intergrown with the fine-grained phyllosilicates and is evenly distributed within three of the four IDPs analyzed (only G1 contains discrete "hot spots" of amorphous carbon). Not all hydrated IDPs contain carbonates.

Acknowledgements. This work was supported by NASA contract NAS 9-18992 and NASA RTOPs 152-17-40-23 and 199-52-11-02.

References. [1] Keller, L. P. *et al.*, (1993) *LPSC XXIV*, 785. [2] Keller, L. P. *et al.*, (1994) *LPSC XXV*, 687.

Figure 1. Electron energy-loss spectra for the major carbon-bearing phases in L2006F10. The onset of the carbon k-edge for oxidized carbon is shifted by ~4.5 eV to higher energy from amorphous carbon and allows both phases to be easily identified even when intimately mixed.



submitted to LPSC XXVI

THE OXIDATION STATE OF ALTERED RIMS ON ILMENITE FROM LUNAR SOILS. Lindsay P. Keller¹, Roy Christoffersen², and David S. McKay². ¹MVA, Inc., 5500 Oakbrook Parkway, Suite 200, Norcross, GA 30093. ²Code Sn, NASA Johnson Space Center, Houston, TX 77058.

Ilmenite grains in lunar soils are commonly surrounded by complex rim sequences that result from their exposure to the lunar "weathering" environment [1,2]. These rims consist of an outer, thin amorphous rind of vapor-deposited silicate material, and a relatively thick, inner layer that is depleted in Fe relative to stoichiometric ilmenite. TEM studies have shown that the inner rim is not amorphous [1,2], but consists of a microcrystalline assemblage of ilmenite containing platy precipitates of rutile and probable Fe metal grains (the R and M grains of [1]). In this study, electron energy-loss spectroscopy (EELS) was used to demonstrate that the altered rims on soil ilmenites contain significant trivalent titanium. Our data indicate that the disordered rims are chemically "reduced" and that oxygen has been lost from the rims. These results have implications regarding the processes responsible for the formation of disordered rims on ilmenite as well as their potential effects on the optical properties of lunar soils.

Aliquots of a <20 μm sieve fractions of 10084 and individual ilmenite grains from the same soil were embedded in low viscosity epoxy, and TEM specimens were prepared by ultramicrotomy. The thin sections were analyzed using a JEOL 2010 (200kV) transmission electron microscope equipped with a LaB₆ filament, a thin-window energy-dispersive x-ray detector, and a GATAN 666 parallel EEL spectrometer. EEL spectra were collected in TEM image-mode at 15KX magnification with a collection semi-angle of ~ 100 milliradians at a dispersion of 0.1 eV/channel. The FWHM of the raw (unprocessed) zero-loss peak was ~ 0.7 eV. The relative energy of features in the spectra for the Ti L_{2,3} edges were calibrated relative to the C π^* peak maximum, which was set to 286 eV [3]. For the Ti L_{2,3} spectra, the characteristic edge structure results from the promotion of inner shell (2p) electrons to valence and conduction bands (3d states). The EELS data provide information on the local solid state environment, including oxidation states. Differences in oxidation state are manifested by "chemical" shifts in energy of the edge onset and by changes in the near-edge structure.

EEL spectra of the Ti L_{2,3} edge have been obtained from over 10 (<20 μm in dia.) individual ilmenite grains from the Apollo 11 soil 10084, and all spectra show significant differences between the altered rims and the core ilmenite (a typical example is shown in Fig. 1). For comparison, EEL spectra from synthetic Ti-oxides with well-constrained Ti³⁺/Ti⁴⁺ ratios are also included in Figure 1. The spectra from the altered rims exhibit a chemical shift of ~ 0.5 eV towards lower energy relative to the position of the Ti L_{2,3} edge in the core of the ilmenite grains. In addition, the splitting of the L₃ and L₂ peaks is reduced in spectra from the disordered rims as compared to the core ilmenite. Both the chemical shift and the change in the near-edge structure are consistent with a Ti³⁺/Ti⁴⁺ ratio of ~ 0.25 in the disordered rims.

The EELS data given here and the EDX measurements reported earlier [1], show that the development of rims was at least partly a chemical process in which the outer margin of the original ilmenite underwent a decrease in Fe/Ti ratio and moved to a more reduced cation-to-oxygen stoichiometry. The analytical and microstructural evidence is consistent with both chemical changes having penetrated to approximately the same depth as the microstructural widths of the rims, which vary from 40-100 nm. Although our working model holds that the inner layer of the ilmenite rims developed because of solar ion bombardment, the penetration depth of these chemical changes is a challenge to explain. Because the thermal history of the grains limits the depth of chemical transport that can be attained by classical diffusion, possible deep-acting chemical effects of solar ion bombardment need to be considered. Several such deep chemical effects have been postulated for ion-irradiated ceramics and

metals [4], almost all of which accomplish deep-level chemical changes using various radiation-enhanced chemical transport mechanisms to promote mixing between the target interior and a preferentially-sputtered surface layer. Other mechanisms involve ion mixing (so-called recoil mixing or recoil implantation) between a thinly deposited surface layer and the bulk [5,6] are not supported by our EELS data, because they imply that the inner rim should be oxidized rather than reduced. We are presently evaluating the other mixing-based mechanisms with regard to their applicability to the ilmenite rims.

We are also investigating the effects of mixed Ti oxidation states on the optical properties of lunar soils. Intervalence charge transfer between Ti^{3+} and Ti^{4+} results in strong absorption of the visible wavelengths [7] and reflectance spectra from reduced Ti-oxides (e.g. Ti_4O_7) have low albedos (~5% reflectance at 550 nm) [8]. The presence of mixed Ti oxidation states is potentially a significant darkening agent in mare soils.

Acknowledgements. This work supported by NASA Contract NAS 9-18992 and NASA RTOP 152-17-40-21 (D. S. McKay).

References. [1] Christoffersen, R. *et al.*, (1994) LPSC XXV, 259. [2] Bernatowicz, T. J. *et al.*, LPSC XXV, 105. [3] Egerton, R. F. and Whelan, M. J. (1974) *J. Electron. Spectr. Rel. Phenom.*, 3, 232. [4] Betz, B. and Wehner, G. K. (1983) *Sputtering by Particle Bombardment II*, Chapter 2 pp. 11-84, Springer-Verlag. [5] Kelley, R. and Sanders, J. B (1976) *Nucl. Inst. Meth. Phys. Res.*, B132, 335. [6] Sigmund, P. (1979) *J. Appl. Phys.* 50, 7261. [7] Burns, R. G. (1993) *Mineralogical Applications of Crystal Field Theory*, Cambridge Univ. Press, 551pp. [8] Bradley, J. P. *et al.*, 1994, LPSC XXV, 159.

Figure 1. Electron energy-loss spectra for the Ti L_{2,3} edge for a typical ilmenite core/rim pair, along with data for Ti^{3+} bearing oxides. The spectra are shifted vertically for clarity.

